The University of Sydney

Faculty of Engineering

School of Civil Engineering

Characterising the Texture and Temperature Effects on the Deformation Mechanism of Magnesium Alloy AZ31: A Simulation Study of the Interplay between Slip, Twinning, and Dynamic Recrystallisation

A Thesis

By

Kenneth James Tam

A Thesis Submitted in Fulfilment of the

Requirements for the Degree

Of

Doctor of Philosophy

June 2020

ABSTRACT

Two viscoplastic self-consistent (VPSC) models were developed to investigate the temperature and texture effects of a hot-rolled magnesium alloy AZ31. These models are coupled with a composite twin grain model and dislocation density based hardening laws to predict the activation and evolution of the deformation mechanisms found within magnesium. At moderate temperatures, there are a variety of active mechanisms in magnesium: $\langle a \rangle$ basal, $\langle a \rangle$ prismatic, and $\langle c + a \rangle$ pyramidal slip, $\{10\bar{1}2\}$ tensile twins, and $\{10\bar{1}1\}$ compressive twins. The validation of the models is done using an experimental study, realised on a hot-rolled AZ31 Mg alloy over a temperature range of 25 °C to 200 °C and under uniaxial tensile loads parallel, perpendicular, and 45° offset from the c-axis of the material. The first developed VPSC model, VPSC-T, incorporates drag stress and interaction matrix as temperature dependent parameters to predict the deformation behaviour of Mg AZ31 at moderate temperatures. The simulation results obtained with this new mode are in good agreement with the experimental results up to 150 °C, where a softening behaviour, due to dynamic recrystallisation, starts to be observed experimentally. Consequently, the second developed VPSC model, VPSC-DRX, incorporates dynamic recrystallisation into the temperature sensitive model, VPSC-T. The simulation results of the new DRX model are in close agreement with the experimental results for temperatures above 150 °C. Additionally, a parametric study has been conducted to investigate the importance of the various parameters needed to accurately predict DRX.

STATEMENT OF ORIGINALITY

I hereby declare that this submission is my own work and to the best of my knowledge it contains no materials previously published or written by another, or substantial proportions of materials which have been accepted for the award of any other degree or diploma at The University of Sydney or any other educational institution, except where due acknowledgement is made in the thesis. Any contribution made to the research by others, with whom I have worked at The University of Sydney or elsewhere, is explicitly acknowledged in the thesis. I also declare that the intellectual content of this thesis is the product of my own work, except to the extent that assistance from others in the project's design and conception or in style, presentation, and linguistic expression is acknowledged.

Signed _____

Kenneth James Tam Date: 29/06/2020

AUTHORSHIP ATTRIBUTION STATEMENT

Sections of Chapter 3 and 4 of this thesis has been published as “Modelling the Temperature and Texture Effects on the Deformation Mechanisms of Magnesium Alloy AZ31” in the International Journal of Mechanical Sciences. I designed this study, analysed the data, and wrote the drafts of the manuscripts.

Signed _____

Kenneth James Tam Date: 29/06/2020

As supervisor for the candidature upon which this thesis is based, I can confirm that the authorship attribution statements above are correct.

Signed _____

Gwénaëlle Proust Date: 22/06/2020

ACKNOWLEDGEMENTS

Firstly, I would like to express my earnest gratitude to my supervisors, A/Prof. Gwénaëlle Proust and Prof. Luming Shen, who have guided me throughout each stage of my thesis till the end. As well as sharing their knowledge in computer modelling and offering their time to provide me advice.

I would also like to thank the Matthew Vaughan and Prof. Ibrahim Karaman from Texas A&M University for donating samples and providing support and advice for the experimental work, and A/Prof. Marko Knezevic of his advice and guidance in computer modelling.

Finally, I would like to thank my friends and family for putting up with me and my incoherent ramblings regarding the ups and downs of PhD life, as well as providing me emotional and food support over the past couple of years, without which I would not have been able to complete my degree.

TABLE OF CONTENTS

LIST OF FIGURES

LIST OF TABLES

Chapter 1 | INTRODUCTION

1.1 BACKGROUND

Moving into the 21st century, energy conservation and efficiency have been increasing in importance in the material selection process. Materials are required to be “green”, which means that there is a need to reduce the carbon footprint in their manufacturing processes and in their life cycles. In order to offset the increased weight of components in different industries, such as transport, infrastructure, or aeronautical industries, the use of lightweight materials is necessary. Common lightweight metals have been increasingly looked at as a solution to solve weight issues. However, commonly used light metals and alloys present some drawbacks; aluminium requires large amounts of energy to be processed, and titanium is a scarce and expensive metal to produce. Magnesium (Mg), which is the lightest metal, has been extensively studied in the last decade as a possible option to fabricate lightweight metallic components. The two major drawbacks for its extensive use have been its low strength and corrosion resistance in comparison to other metals. However, new Mg alloys and fabrication routes are still presently investigated , and recent results are promising. It is, therefore, possible to envision a future for Mg alloys in large scale industrial applications.

1.2 MOTIVATION

Mg is a lightweight material, lighter than the two most commonly used lightweight metals, titanium and aluminium [1-3], and is one of the most abundant elements in the earth’s upper crust [4, 5]. Due to its properties, in recent years, Mg has become increasingly attractive as a materials substitute for current metallic components, as it can be used in a wide range of different applications and industries [1-3, 6]. One of the main restrictions

for the use of Mg and its alloys is the need to manufacture the material at elevated temperatures, adding to the cost of the material. In recent years, it has been shown that it is possible to process Mg alloys at warm temperatures instead of high temperatures. This has been achieved through texture manipulation, causing the activation of different deformation mechanisms that are more attuned for materials processing [7-12]. This is possible, in part, due to Mg being an anisotropic material; changing the loading condition changes the deformation behaviour of the material [8, 9].

Gaining a deep understanding of the deformation mechanism activations will be critical in the development of Mg alloy processing techniques, as each deformation mechanism has a different effect on the plastic deformation behaviour. In order to facilitate the development of new processing routes or to predict the behaviour of the alloys during their life cycle, a model predicting the macroscopic response of Mg alloys by accounting for all deformation mechanisms is necessary. This can be readily achieved through the use of a viscoplastic self-consistent (VPSC) crystal plasticity model [13-15], as it can bridge the deformation mechanisms occurring in the grain to the overall macroscopic response.

1.3 CURRENT RESEARCH

Many groups have worked on modelling the deformation mechanisms of Mg alloys using different crystal plasticity models and approaches [16-22]. Proust *et al.* [16] proposed a new model for simulating the hardening behaviour of twinning, discriminating the dislocation interactions with the twins. Li *et al.* [18] studied the strain rate influences on slip and twinning activation and the resulting hardening behaviour. Chandola *et al.* [17] determined the deformation evolution under various strain paths to discern the anisotropic

effect in Mg. Agnew *et al.* [19] investigated the impact and the roles of prismatic and pyramidal slip under ambient and elevated temperatures. Barnett *et al.* [20] developed a model to predict the plastic deformation of Mg alloys under both tensile and compressive loading. Oppedal *et al.* [21] investigated the anisotropic effect with the hardening mechanism by dislocations coupled to the twinning mechanisms within Mg alloys. These studies investigate the different aspects of the deformation mechanisms of Mg alloys taking into consideration the anisotropic effect and the active deformation mechanisms at different temperatures.

Another deformation mechanism of Mg and its alloys is dynamic recrystallisation (DRX), which is a complex process to predict; there has been an increasing interest in recent years to design and improve on DRX models. Ding and Guo's cellular automaton (CA) model [23] utilises fundamental metallurgical principles to allow accurate predictions of the nucleation and growth of DRX grains. Zhou *et al*. [15] developed a crystal plasticity based DRX model to predict the texture evolution of AZ31 CDRX at 200 °C without any twinning activity. A thermo-mechanical viscoplastic self-consistent (VPSC) DRX model was created by Tang *et al*. [24] using a dislocation density based hardening laws for hot deformation of magnesium, incorporating multiple slip systems, to investigate strain rate and temperature effects at 300 °C to 400 °C. Zecevic *et al*. [25] developed a model using strain fields to show the intragranular misorientation and its effects on the DRX behaviour.

There has not been any model, to this date, able to accurately predict the hardening behaviour and texture evolution during deformation of Mg alloys over temperatures ranging from 25 °C to 200 °C using a single set of hardening parameters. In addition, no model to date, incorporates three different types of deformations mechanisms into one

model; the interactions between slip, twinning, and DRX deformation mechanisms has not been investigated.

1.4 THESIS OBJECTIVES AND AIMS

The aim of this thesis is to develop a temperature sensitive VPSC model in order to predict the deformation behaviour of Mg alloys at low to moderate temperature. This will be achieved by analysing the different deformation mechanisms that can be found in Mg alloys at these temperatures and their sensitivity with respect to the temperature. Additionally, Mg and its alloys are known for their anisotropic behaviour leading to different deformation responses under different loading conditions. Through this analysis, the variety of the different active deformation mechanisms at different temperatures will be revealed, along with their interactions with one another across a variety of different loading conditions.

There are a number of different aspects of the plastic behaviour that needs to be taken into consideration in order to develop such a model: the hardening behaviour, and the microstructural evolution. It is known that different deformation mechanisms elicit a different effect on the hardening behaviour and textural evolution. As such, analysing the hardening behaviour and textural evolution for each deformation mechanism is a critical step in the development of the VPSC model.

An experimental study was previously conducted at Texas A&M University to ascertain the microstructural and mechanical behaviour changes during tension along the normal direction (ND), transverse direction (TD), and 45° offset from the normal direction (ND45) at different temperatures ranging from 25 °C to 200 °C [8]. This study is used

here to calibrate and test the validity of the new VPSC model that has been developed during this work.

In Chapter 2, a literature review on Mg alloys deformation and modelling efforts is presented. Chapter 3 presents the temperature dependent VPSC model that was adapted to Mg deformation and Chapter 4 shows the results obtained for the Mg deformation prediction at different temperatures. Chapter 5 presents the VPSC model incorporating the DRX scheme developed for Mg alloys in this work and the results of this new model are shown in Chapter 6. Conclusive remarks and potential extensions to this work are presented in Chapters 7 and 8, respectively.

Chapter 2 | LITERATURE REVIEW

2.1 MAGNESIUM AND ITS ALLOYS

Magnesium (Mg) and its alloys have become increasingly popular research materials due to their potential uses in numerous structural applications thanks to their low density [1, 26]. Mg has a density of 1.7 g/cm^3, which is four times smaller than that of steel, 7.9 g/cm^3, more than two times smaller than titanium, 4.5 g/cm^3, and 1.6 times smaller than aluminium, 2.7 g/cm^3 [2, 3]. Its density alone enables Mg to be more efficient and allows for a competitive edge over the other traditional lightweight materials, especially when weight is a crucial factor. This low density also gives Mg and its alloys a large specific strength, or strength-to-weight ratio, comparable to other lightweight materials, such as aluminium and titanium (see Figure 2.1) [1-3, 26-29]. As a result, Mg alloys are commonly used in many lightweight applications in the aerospace industry (structural frames), automotive industry (engine blocks) and electronics industry (electronic component bodies and frames) [1, 3, 18, 30-32].

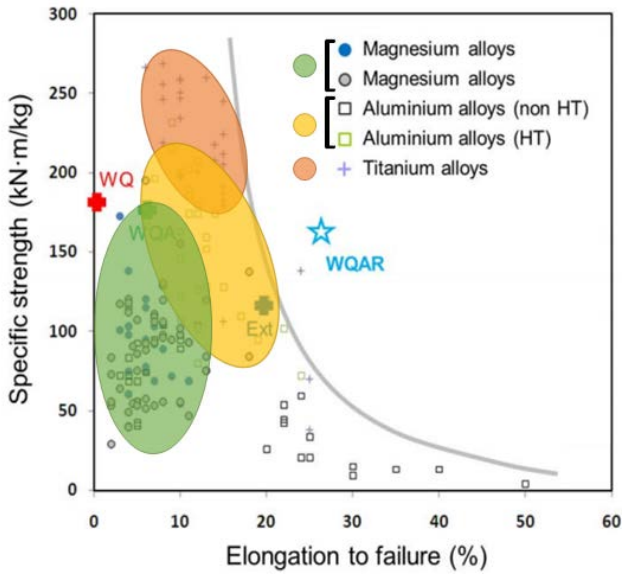

Figure 2.1 Specific strength with regards to ductility for aluminium, titanium, and magnesium alloys. Modified from [27].

Recent studies of Mg alloys have led to the introduction of a new application, as a biomedical implants [6, 33-38]. Commonly in the medical field, implants or medical equipment are inserted to the human body to provide reinforcement, such as screws and pins for bones [6, 34, 36, 38], and stents for blood vessels [37, 38]. There are many different metals and polymers that are used for this purpose, though most require a second surgery in order to extract the medical implant at the end of the treatment, which often leads to additional risks and cost [34, 35]. Notably, Mg alloys are bioabsorbable materials (they are expected to be totally absorbed into the body) as well as being biocompatible, which make them an attractive material in biomedical applications [6, 33, 35-38].

Mg and its alloys are infamous for their pronounced anisotropy (depending on the loading direction, different deformation modes will be activated) as are most hexagonal close-packed materials [16, 18, 19, 21, 39-47] and poor formability at temperatures below 100 °C (only a small amount of plastic deformation can be accommodated at low temperatures) [1, 7, 28, 30, 42], inhibiting their widespread usage. Improving the low temperature formability of Mg requires a deep understanding of its deformation mechanisms and their interactions with each other. In order to overcome the low temperature formability of Mg, the manufacturing of Mg alloys are conducted at temperatures greater than 300 °C [1, 7, 19, 43]. However, it has been shown that manufacturing is possible at temperatures below 200 °C [7, 48]. Processing Mg and its alloys at low temperatures would be a great achievement that would reduce the cost of Mg manufacturing, opening up the material to be used in a wider range of applications.

Furthermore, Mg alloys have a low melting temperature of 650 °C [1], which limits their use for applications with service temperatures below 200 °C [1, 7]. At higher

temperatures, a process known as “creep” occurs, where the material plastically deforms over time at stresses below the yield strength of the material. Therefore, it is important to be able to analyse the different deformation behaviours of Mg and its alloys up to moderate temperatures.

2.2 DEFORMATION MECHANISMS

The active deformation mechanisms of any given material are dependent on the crystal structure type [3, 49]. Common metals, such as steel and aluminium have body centred cubic (BCC) and face centred cubic (FCC) crystal structures, respectively (see Figures 2.2a and b) [3, 49]. These crystal structure types readily deform through slip [3, 49, 50]. On the other hand, Mg has a hexagonal close packed (HCP) (see Figure 2.2c) crystal structure, which greatly changes the active deformation modes [1, 16, 18, 19, 28, 31, 39, 41-43, 45-47, 51, 52].

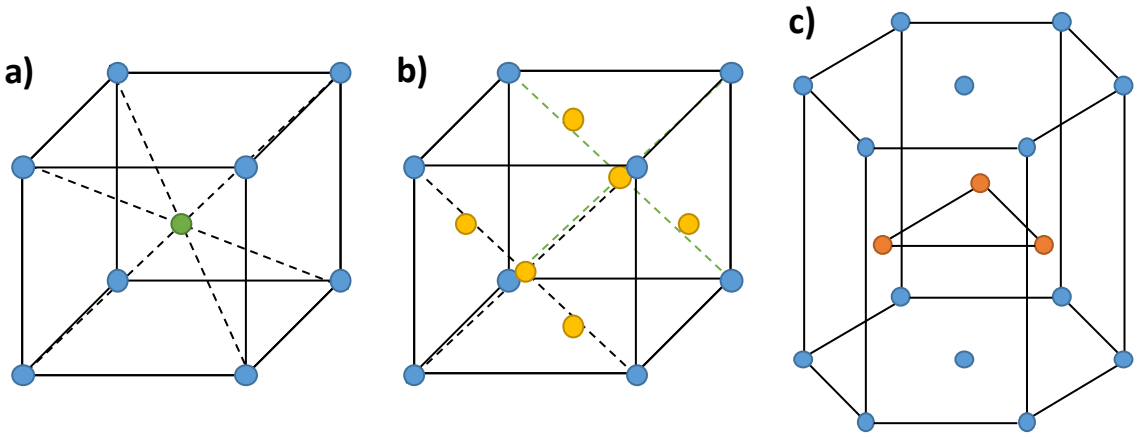

Figure 2.2 Schematic structure and atom arrangement of the different crystal structures: a) BCC, b) FCC, and c) HCP

Due to the crystal structural differences, HCP materials, such as Mg and titanium, have a lower number of active slip systems for slip activity compared to the other crystal structures [3, 19, 31, 41, 43, 49]. According to the Taylor criteria, the lower number of

slip systems are insufficient for accommodating homogeneous deformation [13, 28, 41, 44, 53], and as a result, the additional deformation modes that are activated to accommodate plastic strain, come in the form of deformation twinning in HCP materials [1, 16, 18, 19, 28, 31, 39, 41-43, 46, 51, 52, 54].

2.2.1 Slip Deformation

The slip deformation occurs through the motion of dislocations on specific planes and along specific directions, leading to the material to "slip" causing plastic deformation, see Figure 2.3 [49]. Dislocations are created within the material from imperfections of the crystal lattice and can be categorised into two different types, known as edge- and shear-type, though most dislocations are a combination of both types. Edge-type dislocations are an extra half plane of atoms, highlighted by the green atoms in Figure 2.4, and move parallel to the direction of the local applied force, shown through the yellow arrow. Shear-type dislocations are a shear distortion, which causes a portion of the crystal to slide across one another, highlighted by the different coloured atoms in Figure 2.5, and move perpendicularly to the direction of the local applied force, shown through the yellow arrow. Despite causing large amounts of deformation to the material leading to the eventual failure of the material, overall slip deformation has minimal influences on the textural evolution [7, 17, 19, 29, 31, 39, 51, 55, 56].

Figure 2.3 Illustration of slip in a single zinc crystal. Modified from [49].

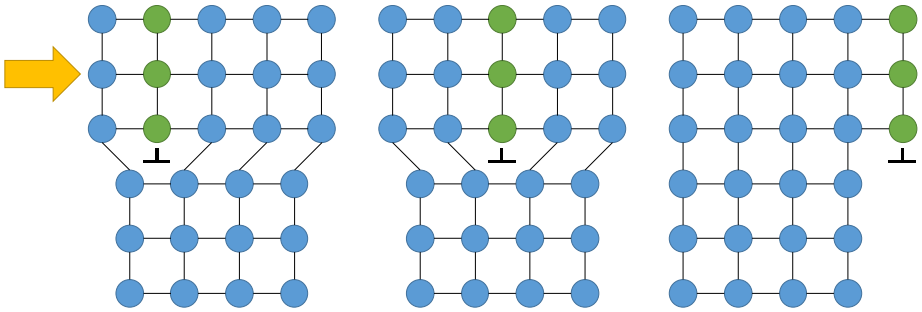

Figure 2.4 Illustration of the evolution of the edge-type dislocation. The blue atoms represent the lattice, and the green atoms represent the extra half plane of atoms.

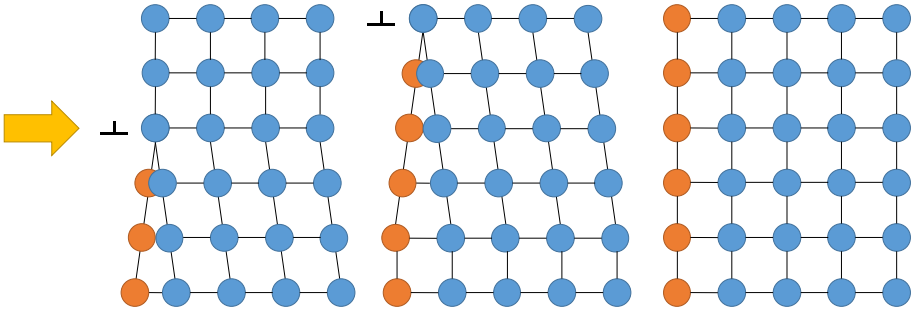

Figure 2.5 Illustration of the evolution of the shear-type dislocation. The blue atoms represent the upper portion of the lattice, and the orange atoms represent the lower portion.

In Figure 2.6, a generic stress-strain curve of a slip dominant deformation behaviour is shown, along with its corresponding work hardening curve. The stress-strain curve (Figure 2.6a) has a linear initial region until the yield strength is reached. After this yield point, plastic deformation is observed, with more or less hardening depending on the material, until fracture occurs in the material. The work hardening curve (Figure 2.6b) shows the evolution of the hardening rate, $d\sigma/d\varepsilon$, as a function of the macroscopic plastic stress, and it can be used to qualitatively ascertain the predominant deformation mechanism that has been activated during deformation. Here the slip dominant deformation behaviour is determined through the continuous decreasing hardening rate with increasing plastic stress.

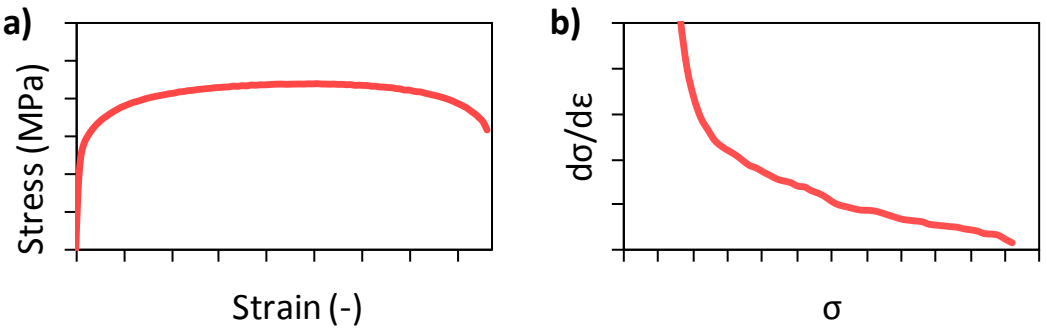

Figure 2.6 Typical slip behaviour in the: (a) stress-strain curve and (b) work hardening curve.

It is widely known that Mg deforms through a number of different slip modes on different slip systems: basal slip $\{0001\}\langle 11\bar{2}0\rangle$, prismatic slip $\{10\bar{1}0\}\langle \bar{1}2\bar{1}0\rangle$, pyramidal-I slip $\{10\bar{1}0\}\langle 11\bar{2}0\rangle$, and pyramidal-II slip $\{10\bar{1}2\}\langle 11\bar{2}3\rangle$ [17-19, 21, 28, 29, 31, 39-41, 43, 44, 46, 50-52, 57-59]. These slip modes of Mg are highlighted in Figure 2.7 by the red planes, with reference to HCP crystal structure. For Mg the easiest slip systems to activate are the basal slip systems, due to their low critical resolved shear stress (CRSS) and as a consequence basal slip is usually one of the dominant deformation mode [1, 16, 31, 40, 41, 44, 52, 56, 59].

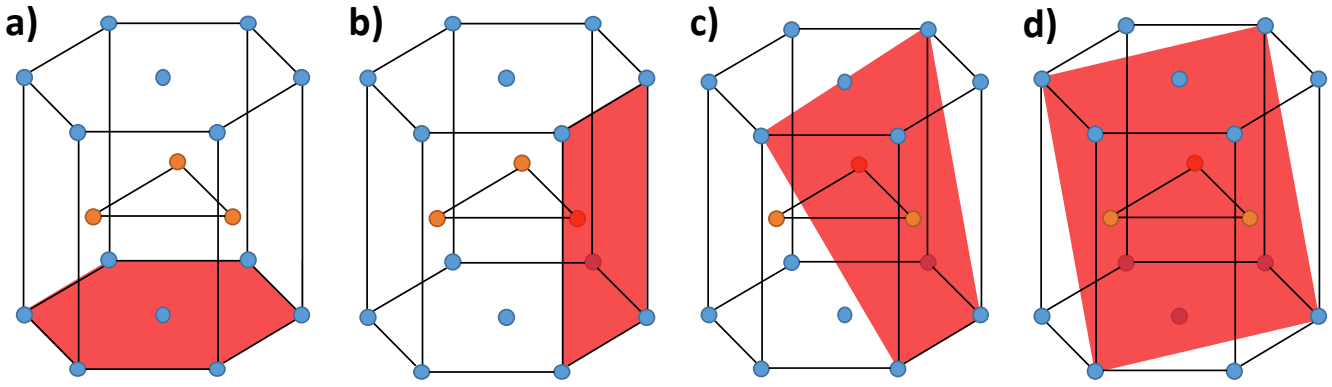

Figure 2.7 Schematic of HCP slip systems: (a) basal, (b) prismatic, (c) pyramidal-I, and (d) pyramidal-II

Owing to the anisotropic effect, depending on the loading conditions different slip modes are activated preferentially and each of them is able to become one of the dominant

deformation mode [1, 16, 18, 19, 28, 31, 39, 41-43, 45-47, 51, 52]. The c-axis is parallel to the height of the HCP crystal structure shown in Figure 2.2, and when the loading direction is perpendicular to this c-axis, prismatic slip is preferentially activated [17, 19, 39, 41]. As temperature increases, the pyramidal slips become active; at room temperature, the CRSS for pyramidal slip has a high value that decreases with increasing temperature such that at higher temperatures it becomes one of the predominant deformation modes [39, 43, 60, 61]. In general, non-basal deformation slip modes are difficult to activate at low temperatures, this accounts for the pronounced anisotropy and poor formability of Mg alloys [1, 16, 18, 19, 28, 31, 39, 41-43, 45-47, 51, 52] as other deformation modes need to be activated to supplement basal slip.

2.2.2 Twinning Deformation

In the previous section, it was noted that at low temperatures basal slip is not able to encompass the total deformation. Subsequently, a different deformation mode is needed in order to accommodate plastic strain, this new deformation mode is known as twinning [17-19, 21, 28, 29, 31, 39-41, 43, 44, 46, 50-52, 57-59]. The twinning deformation process causes a reorientation of the crystal structure in small regions in a grain, such that it creates a reflection of the plane orientations, see Figure 2.8 [49]. Unlike slip deformation, where the material is able to undergo large amounts of plastic deformation, the twinning reorientation results in minimal physical changes.

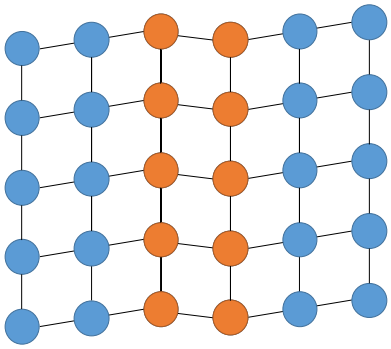

Figure 2.8 Atomic structure of a crystal lattice (in blue) containing a twinned region (in orange).

In Figure 2.9, a generic stress-strain curve of a twinning dominant deformation behaviour is shown, along with its corresponding work hardening curve. The stress-strain curve (see Figure 2.9a) exhibits a downward curvature, creating an "S" shape, which is indicative of twinning deformation. The work hardening curve (see Figure 2.9b) has a decreasing curve followed by an increase in the hardening rate before decreasing at a higher stress, creating a cubic parabola. This work hardening curve is typical of plastic deformation occurring predominantly through twinning.

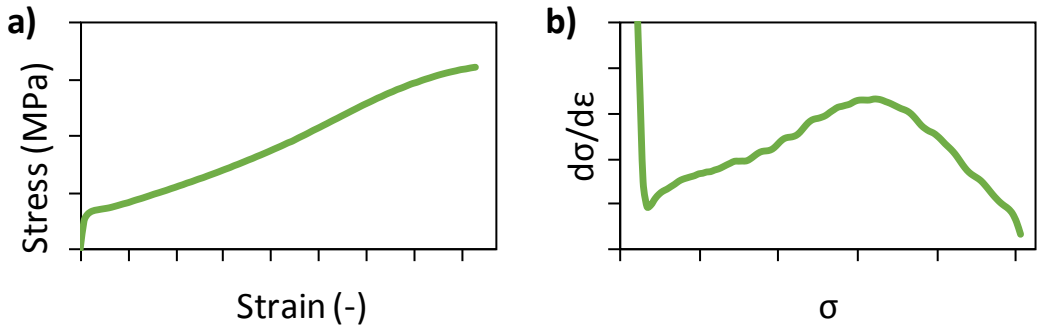

Figure 2.9 Typical twinning behaviour in the: (a) stress-strain curve and (b) work hardening curve.

There are two different types of twinning found in Mg and they are known as $\{10\bar{1}2\}\langle\bar{1}011\rangle$ tensile twinning and $\{10\bar{1}1\}\langle10\bar{1}\bar{2}\rangle$ compressive twinning [17, 19, 21, 28, 29, 31, 43, 44, 46, 51, 52, 58, 59]. These twinning modes are highlighted by the green planes shown in Figure 2.10 with reference to HCP crystal structure. Here the grains that have undergone tensile and compressive twinning, show a great change in their

crystallographic orientation, as a result of the reorientation. This reorientation is dependent on the deformation system and the c/a axis ratio. $\{10\bar{1}2\}\langle\bar{1}011\rangle$ Tensile twinning reorientates the grains by 86° [7, 16-18, 20, 22, 28, 31, 39, 43, 51, 55, 56], and $\{10\bar{1}1\}\langle10\bar{1}\bar{2}\rangle$ compressive twinning reorientates the grains by 57° [17, 29, 46, 51, 55, 56]. Tensile twinning is readily found at low temperatures, being the other dominant deformation mechanisms alongside basal slip [8, 9, 46, 51]. This high level of twinning activity is unsuitable for the processing of Mg alloys, as it results in the formation of shear bands and leads to the eventual fracture of the material [7, 31]. This is the reason behind the poor low temperature formability of Mg alloys, as such in the manufacturing process of magnesium temperature needs to be elevated to activate more slip deformation modes, namely pyramidal slip [9, 19].

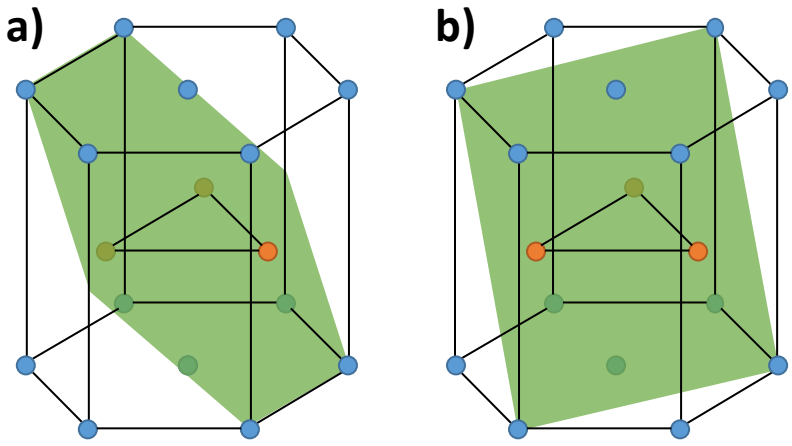

Figure 2.10 Schematic of the twinning planes in HCP: (a) $\{10\bar{1}2\}$ tensile twinning, and (b) $\{10\bar{1}1\}$ compressive twinning.

2.3 Temperature Sensitive Deformation Mechanisms in Magnesium

In Section 2.2, it was stated that, in general, basal slip is the easiest deformation mechanism to activate in Mg alloys, as it has a low CRSS value, and it is expected to be

one of the dominant deformation mode at room temperature [1, 16, 31, 40, 41, 44, 52, 56, 59]. However, due to the limited active slip systems a secondary deformation mode is necessary to accommodate plastic strain [3, 13, 28, 41, 44, 53]. This secondary deformation mode is dependent on the loading direction, as a result of the anisotropic effect found in Mg alloys [16, 18, 19, 21, 39-47]. Determining the competing active deformation mechanisms and their interactions with one another at low to moderate temperatures will aid in improving poor low temperature formability.

At room temperature, non-basal slip systems are difficult to activate as the CRSS values for prismatic and pyramidal slip are much higher than those for basal slip and tensile twinning [18, 28, 31, 56]. Due to the anisotropic effect, prismatic slip is activated at the expense of tensile twinning when the loading direction is normal to the c-axis [17, 19, 39, 41]. When the loading direction is parallel to the c-axis, the propensity for prismatic slip disappears and the predominant deformation mechanisms are basal slip and tensile twinning [8, 9, 46, 51].

At elevated temperatures, the formability of Mg increases [19, 28, 30, 31, 39, 43, 46, 62] due to the decrease of the CRSS values of the different slip modes [29, 39, 43, 61]. Although twinning is not temperature sensitive, pyramidal-II slip is and at elevated temperatures the CRSS for that slip mode decreases drastically and pyramidal-II slip becomes one of the predominant deformation modes [39, 43, 60, 61]. The activation of the pyramidal slip deformation, results in a mixture of slip and twinning at this temperature range, as twinning still plays a significant role in the deformation behaviour. The anisotropic nature of Mg is still observed at this temperature, as Mg alloys are able to activate prismatic slip when loading occurs perpendicularly to the c-axis [9, 28, 31, 39].

When the loading conditions reaches temperatures above 200 °C, there is minimal amounts of twinning, despite the loading direction be favourable to the activation of tensile twinning [8, 9]. Here the dominant deformation mode shifts from a twinning dominated deformation behaviour seen at low temperatures to a slip dominated deformation behaviour, with large amounts of basal and pyramidal slip [9, 28, 29, 43, 52]. Table 2.1 contains all the various deformation mechanism active in Mg at low to moderate temperatures, with respect to the relationship between loading direction and the c-axis. Furthermore, at higher temperatures a new deformation mechanism emerges known as dynamic recrystallisation (DRX), which begins to accommodate some of the plastic strain [9, 19, 43, 48, 63].

Table 2.1 Active anisotropic deformation mechanisms for Mg alloys at different temperatures.

Loading Direction (in relation to the c-axis)	Temperature		
	25 °C	100 °C	200 °C
Parallel	Tensile Twinning Basal Slip	Tensile Twinning Basal Slip	Basal Slip Pyramidal Slip
45° offset	Tensile Twinning Basal Slip Prismatic Slip	Basal Slip Pyramidal Slip	Basal Slip Pyramidal Slip
Perpendicular	Basal Slip Prismatic Slip	Basal Slip Prismatic Slip Pyramidal Slip	Basal Slip Pyramidal Slip

2.3.1 Dislocation Motion Mechanisms at Elevated Temperatures

In Section 2.3 the slip systems in Mg that are active at elevated temperatures are discussed. The thermal activation of slip planes is possible as dislocation motion is a thermally sensitive deformation mechanism, where there are additional mechanisms to facilitate the activation of dislocation motion. These mechanisms include dislocation climb and cross-slip, which enables the activation of immobile dislocations.

Dislocation climb is the activation of a sessile (immobile) dislocations, turning them into glissile (mobile) dislocations [64-66]. This is achieved through a diffusion process at elevated temperatures by adding or removing an atom at the dislocation core [64-66]. A dislocation core is the area surrounding the end of a dislocation, which is represented by the uptick in Figure 2.4. Dislocation climb has been readily observed in various HCP alloys [67-70].

The other mechanism for dislocation motion at elevated temperatures is cross slip, wherein a screw dislocation transfers to a different slip plane before returning to its original slip plane [66, 71]. This is possible due to the disassociation of a part of the dislocation into its Shockley partials allowing motion of the entire dislocation [66, 71]. This cross-slip mechanism has been found to be active in Mg alloys at elevated temperatures, in particular for $\langle c + a \rangle$ pyramidal slip [69, 72, 73].

2.4 DYNAMIC RECRYSTALLISATION

DRX is a deformation mechanism that occurs at elevated temperatures, wherein the grains in a material splinter into many smaller grains to accommodate strain [7, 11, 12, 74-80]. Commonly, the DRX behaviour is observed through a reduction in the flow stress after a

peak stress, or a softening behaviour, as shown in Figure 2.11 [8, 9, 15, 24, 30, 80-91]. This drop in stress seen in the stress-strain curve (see Figure 2.11a), creates a reverse hardening effect creating a "hook" shape seen in the work hardening curve (see Figure 2.11b) [84, 85, 90, 92]. This softening behaviour is observed for the different DRX mechanisms; discontinuous DRX (DDRX), and continuous DRX (CDRX) [74, 78, 79, 81, 82, 86, 88, 91, 93, 94]. Generally, the stacking fault energy (SFE) can determine which DRX mechanism is active, DDRX occurs in materials with a low SFE materials, while CDRX is commonly found in high SFE materials [30, 74, 90, 95-97]. However, the thermo-mechanical processing conditions are the main factor for the activation of the different DRX mechanisms [30, 74, 78, 81, 86-88, 91, 94, 95, 97-99].

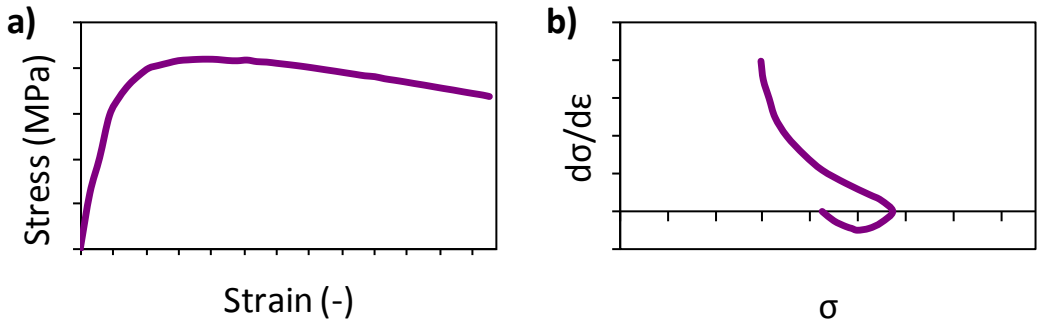

Figure 2.11 Typical DRX behaviour in the: (a) stress-strain curve and (b) work hardening curve. The work hardening curve is adapted from [84].

2.4.1 Discontinuous Dynamic Recrystallisation

When unspecified DRX generally refers to the DDRX as it is the most observed type of recrystallisation processes, and is the conventional DRX process wherein grains are nucleated in the grain boundaries of the parent grains [10, 74, 98]. This process is detailed in Figure 2.12. Due to the tendency of the nucleation sites to be in the grain boundaries, the resulting DRX grains produce a "necklace-like structure", defined by high angle grain

boundaries (HAGB) between the newly nucleated grains and the parent grain [10, 78, 82, 87, 88, 98]. Nucleation sites are not limited to grain boundaries, as DRX grains have been observed along twin boundaries and shear bands as well [7, 11, 12, 30, 77, 81, 86, 91, 94, 96].

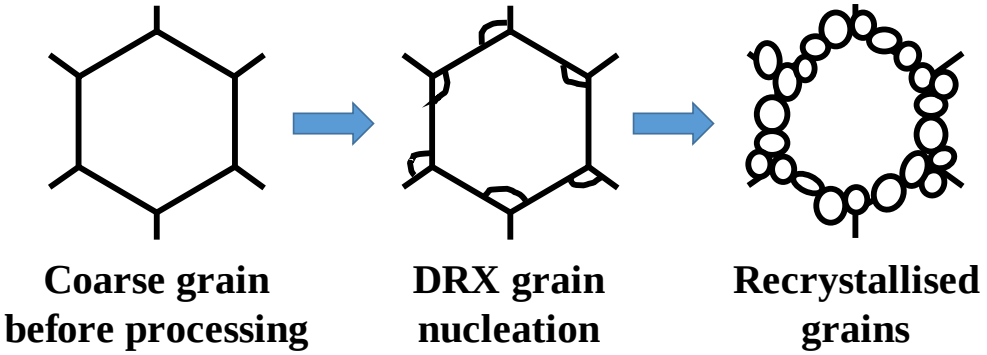

Figure 2.12 Flowchart of the DDRX mechanism. Adapted from [98].

When compared to slip deformation, the DDRX mechanism causes a greater change in the microstructure, owing to the HAGBs created, with misorientation angles greater than 15° [74, 86, 93, 99]. Despite this microstructural evolution, overall the DDRX mechanism has a minimal effect on the overall textural evolution of the material, maintaining a similar deformed texture with the initial texture [7, 10-12, 77, 78, 81, 94]. As a result, the main source of textural change comes from the reorientation of the grains by twinning.

2.4.2 Continuous Dynamic Recrystallisation

The other main type of DRX is known as CDRX, where the nucleation sites for the recrystallised grains occurs within the parent grain as opposed to the grain boundaries as seen in DDRX [74, 95]. In this case, defined sub-grain boundaries are developed with the aid of dislocations, where these sub-grains contain limited dislocations within them [74]. With increasing strains and dislocation accumulation, these sub-grains rotate into low angle grain boundaries (LAGB) creating recrystallised grains, and eventually after further

deformation, HAGBs can also appear [74, 78, 81, 91, 95, 100, 101]. Therefore, the CDRX mechanism can produce a similar deformed texture as the initial texture [78, 81, 91, 95, 100, 101], akin to the DDRX mechanism. A graphical evolution of the CDRX process is detailed in Figure 2.13.

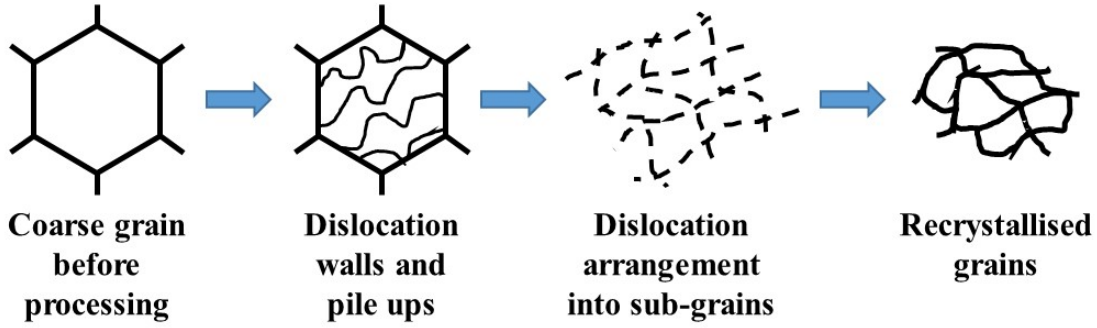

Figure 2.13 Flowchart of the CDRX mechanism. Adapted from [98].

2.4.3 Twin-Related Dynamic Recrystallisation

In addition to the two main DRX mechanisms, there is another sub-mechanism for the DRX process known as twin-assisted or twin-induced DRX [12, 30, 81, 86, 91, 94, 96]. The deformation twins provide additional grain boundaries for either DDRX or CDRX to occur [11, 30, 74, 78, 79, 81, 86, 91, 94, 96, 100, 102-104]. During DDRX, the formation of twins ultimately increases the number of potential nucleation sites for recrystallised grains [78, 86]. Meanwhile, in CDRX the twin boundaries encourages dislocation accumulation in the sub grains eventually leading to the lattice rotation [78, 81, 91, 100, 101]. As with DDRX and CDRX, the twin-assisted DRX mechanism causes minimal textural evolutions [11, 74, 78, 79, 81, 86, 91, 94, 96, 100, 102-104], although the creation of the twins in the first instance would drastically change the texture.

2.4.4 Dynamic Recrystallisation in Magnesium Alloys

The DRX mechanism in Mg only occurs at elevated temperatures where there are significant levels of dislocation activity [9, 10, 15, 23-25, 70, 105] and the threshold for the DRX grain nucleation has decreased. As previously discussed, the slip and twinning deformation mechanisms in Mg alloys are highly dependent on the temperature, which can be said for the DRX mechanism. For Mg the active DRX mechanism is dependent on the deformation temperature; CDRX is active below 150 °C [78, 81, 86, 91, 94, 98, 99], DDRX is active at 250 °C and above [86-88, 91, 94], and a combination of both DDRX and CDRX occurs between these two temperatures [87, 88, 93, 99, 101, 104].

For Mg alloys at moderate temperatures (between 100 °C and 150 °C) deformation twinning is still prevalent, resulting in significant volume fractions of twinned grains [8, 9, 46, 51], creating an abundance of nucleation sites for DRX. Though, experimentally, DRX only exists at higher temperatures where deformation occurs through dislocation slip producing the necessary dislocations to activate the DRX mechanism. At high temperatures, there are a limited number of twinned grains that do form and can aid in the DRX process [30, 81, 86, 91, 94]. It should be noted that at lower temperatures, the DRX mechanisms are difficult to be distinguished apart. Twin-assisted CDRX can be mistaken for DDRX; when CDRX occurs it will consume the entire twinned region, creating the necklace-like structure appearing in between grain boundaries akin to DDRX [78, 86, 87, 100].

2.5 CRYSTAL PLASTICITY MODELLING

Crystal plasticity (CP) models create a framework around a deformation mechanism, which is used to analysis the deformation behaviour and correlates its influences at the

macroscopic scale [13, 14, 42, 75, 106]. These CP-based models can be combined with other types of models, as a means to obtain a deeper understanding of the deformation behaviours being investigated [58, 107]. A commonly used CP-based model, viscoplastic self-consistent (VPSC) is explained in further detail in Chapters 3 and 5. In these chapters a detailed review on temperature effect modelling and DRX modelling is given to help understand how the new versions of the model obtained during this work. In the following paragraphs a short description of where these models have been used are given.

CP-based models are used, due to their versatility, in modelling the deformation mechanisms of different materials under varying loading conditions [13, 14, 20, 50, 108, 109]. Barnett *et al.* [20] modelled the twinning behaviour in Mg single crystal, investigating the mechanical flow behaviour under tensile and compressive loads and their effects on the microstructure. Bertin *et al.* [50] investigated the interactions between the different dislocation-dislocation interactions of the different slip systems found in pure Mg. Proust *et al.* [13] developed a composite grain model to define the twinning behaviour for a polycrystalline zirconium (Zr) alloy. This particular was then adapted to predict the strain-path changes behaviour of Mg AZ31 [16]. A dislocation density based constitute hardening law was developed by Beyerlein and Tome [14], incorporating the temperature effects on the deformation mechanisms of twinning and slip. This model was then used to describe the behaviour of Mg AZ31 at different strain rates [18]. Knezevic [108] developed a physically based constitute law dependent on the strain and temperature for single crystal BCC alloys.

Modern models of the DRX mechanism are based on Ding and Guo's cellular automaton model [23], which is utilises the fundamental metallurgical principles of the DRX process.

Li *et al.* [106] developed a model for the prediction of the DRX behaviour of two-phase titanium alloys. Zhou *et al.* simulated the deformation behaviour of the different DRX mechanisms, DDRX [83] and CDRX [15]. Popova *et al.* [58] developed a new nucleation and growth model for the DRX mechanism in Mg alloy AZ31. The twin-assisted DRX mechanism was investigated by Popova *et al.* [75] determining its influence on the deformation behaviour. Li *et al.* [42] analysed the DRX deformation behaviour with respect to the anisotropic behaviour within an AZ31 alloy.

Additionally, there have been other studies utilising a different DRX model by Wenk *et al.* [110]. Solas *et al.* [111] developed a recrystallisation model for hexagonal polycrystals through the use of parallelepipedal cells to describe the nucleation and growth of grains. Walde and Reidel [112] investigated the texture evolution of DRX in Mg alloy AZ31 noting that the activation of prismatic slip is required to accurately describe the texture evolution. Whilst, Zecevic *et al.* [113] utilised the strain energy and misorientation angles to determine the thermo-mechanical response and texture evolution of DRX in a WE43 Mg alloy.

In conjunction with the CP-based models described above and those discussed in the previous chapter, there are many studies with different models investigating the deformation mechanisms, twinning, slip, and DRX, and their influence on the deformation behaviour at different temperatures. These studies focuses their investigations on one or two of these mechanisms being tested at room temperature [14, 16-22, 108] and at temperatures above 200 °C [14, 15, 17, 58, 75, 83, 106, 108]. However, only a few studies was done to predict Mg behaviour over a range of temperatures from room temperatures to 200 °C [19, 42]. While there have been a lot of work on

characterising the behaviour of Mg alloys over a large range of temperatures or on modelling the behaviour of Mg alloys at a given temperatures. There has not been a single model, to this date, incorporating the three different deformations mechanisms for Mg (slip, twinning, and DRX) and able to predict the mechanical response and textural evolution of Mg alloys from 25 °C and 200 °C.

2.6 SUMMARY

Magnesium is an increasingly popular material, being used in a wide variety of different applications and industries, due to its high specific strength and extremely low density. Despite the increase in popularity, Mg and its alloys are limited in use as a result of its low temperature formability and anisotropic behaviour. This causes the need to manufacture Mg alloys at higher temperatures to preferentially activate the slip deformation mechanism and to avoid activating the twinning deformation mechanism. At these elevated temperatures, there is the activation of another deformation mechanism, DRX, which makes predicting the deformation behaviour of Mg alloy at warm temperatures difficult. Improving the low temperature formability requires an in-depth understanding of the interactions between these three deformation mechanisms of Mg alloys. This can be achieved through the use of CP-based models, which can correlate the microscopic behaviour of the deformation mechanisms to the macroscopic response of the material.

Chapter 3 | THE TEMPERATURE DEPENDENT VISCOPLASTIC SELF-CONSISTENT MODEL

3.1 HISTORY AND INTRODUCTION

Historically, the VPSC model was developed for the application of low symmetry materials such as hexagonal, trigonal, and orthorhombic crystal structures. While the initial intention of the VPSC model was to model low symmetry materials, it has been shown to perform well with cubic crystal structures as well. The name refers to the mechanical regime (VP; viscoplastic) and approach (SC; self-consistent) used in the creation of the model. The VPSC model was first used to predict the mechanical response of a Zr alloy and ascertain the deformation mechanisms responsible for the textural evolution. This was achieved through the incorporation of the grains' interactions with one and another, a crucial aspect in the modelling of anisotropic materials, such as Zr and Mg.

The anisotropic viscoplastic response is achieved through the use of a homogenous effective medium (HEM) to represent the neighbouring grains surrounding a single grain, which is defined as an ellipsoidal inclusion. Using external stresses and strains, the VPSC model is able to simulate the plastic deformation, such as the hardening behaviour, reorientation, and shape change, of a grain. A self-consistent approach is used to calculate a mean-field approximation to the environment of each individual grain, and the aggregate of each grain provides the macroscopic response. Once the macroscopic stress-strain response is found, it enables the prediction of the microstructural evolution, deformation mechanisms activities, and hardening behaviour that is associated with plastic deformation.

3.2 KINEMATIC EQUATIONS

In this section, a brief overview of the kinematic equations for any continuum plastic body is shown. The deformation of the grain is dictated by a displacement gradient tensor, $\boldsymbol{L}$, and a deformation gradient tensor, $\boldsymbol{F}$. The deformation rate is defined by the following equation [114, 115]:

$$\dot{\boldsymbol{F}} = \boldsymbol{L} \cdot \boldsymbol{F} \tag{3-1}$$

The deformation gradient tensor can be expressed in terms of plastic stretch, $\boldsymbol{F}_0$, and plastic rotation, $\boldsymbol{R}$, in the following equation [114, 115]:

$$\boldsymbol{F} = \boldsymbol{R} \cdot \boldsymbol{F}_0 \tag{3-2}$$

Here, the plastic stretch is used to determine the plastic stretch rate, $\dot{\mathbf{F}}_0$, in following equation [114, 115]:

$$\dot{\boldsymbol{F}}_0 = \boldsymbol{L}_0 \cdot \boldsymbol{F}_0 \tag{3-3}$$

where $\boldsymbol{L}_0$ is the velocity gradient, which is defined by the linear superposition of the shear rate of the active deformation systems [115]:

$$\boldsymbol{L}_0 = \sum_s \dot{\gamma}_s \boldsymbol{b}_s \boldsymbol{n}_s \tag{3-4}$$

where "s" is the deformation system, $\dot{\gamma}_s$ is the shear rate, $\boldsymbol{b}_s$ and $\boldsymbol{n}_s$ are the Burger's vector and the normal to the Burger's vector associated with the deformation system, s.

The Burger's vectors can be used to describe the displacement gradient tensor in terms of the symmetry [115]:

$$\boldsymbol{m}_s = \frac{1}{2}(\boldsymbol{b}_s \boldsymbol{n}_s + \boldsymbol{b}_s \boldsymbol{n}_s) \tag{3-5}$$

and skew symmetric components [115]:

$$\boldsymbol{q}_s = \frac{1}{2}(\boldsymbol{b}_s\boldsymbol{n}_s - \boldsymbol{b}_s\boldsymbol{n}_s) \tag{3-6}$$

This allows the displacement gradient tensor, $\boldsymbol{L}_0$, from Equation (3-4), to be decomposed into the strain rate, $\boldsymbol{D}_0$, and rotation rate, $\boldsymbol{W}_0$, as follows [114, 115]:

$$\boldsymbol{L}_0 = \boldsymbol{D}_0 + \boldsymbol{W}_0 \tag{3-7}$$

$$\text{where } \boldsymbol{D}_0 = \sum_s \dot{\gamma}_s \boldsymbol{m}_s \tag{3-8}$$

$$\boldsymbol{W}_0 = \sum_s \dot{\gamma}_s \boldsymbol{q}_s \tag{3-9}$$

The strain rate, $\boldsymbol{D}$, and rotation rate, $\boldsymbol{W}$, can be written as a function of the plastic rotation term, $\boldsymbol{R}$ [114, 115]:

$$\boldsymbol{D} = \boldsymbol{R} \cdot \boldsymbol{D}_0 \cdot \boldsymbol{R}^T \tag{3-10}$$

$$\boldsymbol{W} = \boldsymbol{R} \cdot \boldsymbol{W}_0 \cdot \boldsymbol{R}^T + \dot{\boldsymbol{R}} \cdot \boldsymbol{R}^T \tag{3-11}$$

The velocity gradient is utilised to define and determine the magnitude of the plastic deformation, split in terms of stretch and rotation. This strain rate and rotation rate will be used to determine the stress-strain state of a grain and the polycrystalline material.

3.3 Self-Consistent Formalisation

Considering a polycrystalline structure, a viscoplastic constitutive behaviour within the grain can be described using a non-linear sensitivity equation [13-15, 56, 109]:

$$\dot{\varepsilon} = \sum_s \boldsymbol{m}_s \dot{\gamma}_s = \dot{\gamma}_0 \sum_s \boldsymbol{m}_s \left(\frac{\boldsymbol{m}_s \cdot \boldsymbol{\sigma}_r}{\tau_0^s} \right)^n \tag{3-12}$$

where $\dot{\varepsilon}$ is the deviatoric strain rate, $\boldsymbol{m}_s$ is the symmetric Schmid tensor associated with a deformation system, $\boldsymbol{\sigma}_r$ is the deviatoric stress within the grain, $\boldsymbol{\tau}_0^s$ is the threshold stress or the CRSS for deformation activation, $\dot{\gamma}_0$ is a normalisation factor, and n is the

strain-rate sensitivity. Through linearisation of Equation (3-12), the local constitutive behaviour within a grain can be obtained [109]:

$$\dot{\varepsilon}_r = \boldsymbol{M}_r \cdot \boldsymbol{\sigma}_r + \dot{\varepsilon}_{0,r} \tag{3-13}$$

where $\boldsymbol{M_r}$ is the viscoplastic compliance, and $\dot{\varepsilon}_{0,r}$ is the back-extrapolated term. Equation (3-13) then can be homogenised to obtain the effective strain rate at the macroscopic level [109]:

$$\bar{\dot{\varepsilon}} = \bar{\boldsymbol{M}} \cdot \bar{\boldsymbol{\sigma}} + \bar{\dot{\varepsilon}}_o \tag{3-14}$$

where "$-$" above each term denotes the macroscopic magnitude. The macroscopic compliance and back-extrapolated terms are the unknowns within the formalisation and are adjusted self-consistently. The local constitutive behaviour of a grain in Equation (3-13) can instead be written in terms of the macroscopic moduli and back-extrapolated term, and any resulting inhomogeneity created is given by an eigen strain rate, ε_r^* [115]:

$$\dot{\varepsilon}_r = \bar{\boldsymbol{M}} \cdot \boldsymbol{\sigma}_r + \bar{\dot{\varepsilon}}_o + \varepsilon_r^* \tag{3-15}$$

Combining the effective macroscopic strain rate, Equation (3-14), and the new local constitutive behaviour, Equation (3-15), gives the deviation equation for the grain [115]:

$$\tilde{\boldsymbol{\sigma}}_{\boldsymbol{r}} = \bar{\boldsymbol{L}}(\tilde{\dot{\varepsilon}}_{\boldsymbol{r}} - \varepsilon_{\boldsymbol{r}}^*) \tag{3-16}$$

where "$\sim$" above the terms denotes the local deviations from macroscopic values, i.e. $\tilde{\boldsymbol{\sigma}} = \bar{\boldsymbol{\sigma}} - \boldsymbol{\sigma}_r$, and $\bar{\boldsymbol{L}} = \bar{\boldsymbol{M}}^{-1}$. The deviation equation, Equation (3-16), can be expressed in terms of a symmetric Eshelby tensor, $\boldsymbol{S}$, and eigen strain rate, $\boldsymbol{\varepsilon}_{\boldsymbol{r}}^*$, giving the interaction equation [13, 109]:

$$\tilde{\dot{\varepsilon}}_r = -\tilde{\boldsymbol{M}} \cdot \tilde{\boldsymbol{\sigma}}_{\boldsymbol{r}} \tag{3-17}$$

where the interaction tensor is given by [13, 109]:

$$\widetilde{\boldsymbol{M}} = (\boldsymbol{I} - \boldsymbol{S})^{-1}\boldsymbol{S} \cdot \bar{\boldsymbol{M}} \tag{3-18}$$

Replacing the local and overall deviatoric constitutive relations in Equations (3-13) and (3-14) in the interaction Equation (3-17) gives the following localisation equation [115]:

$$\boldsymbol{\sigma_r} = \boldsymbol{B}_r \cdot \bar{\boldsymbol{\sigma}} + \boldsymbol{b}_r \tag{3-19}$$

where $\mathbf{B}_\mathrm{r} = \left(\mathbf{M}_\mathrm{r} + \widetilde{\mathbf{M}}\right)^{-1}(\bar{\mathbf{M}} + \widetilde{\mathbf{M}})$ and $\mathbf{b}_\mathrm{r} = \left(\mathbf{M}_\mathrm{r} + \widetilde{\mathbf{M}}\right)^{-1}(\bar{\dot{\varepsilon}}_0 + \dot{\varepsilon}_{0,\mathrm{r}})$. Using the stress localisation Equation (3-19) in the local constitutive Equation (3-13), the strain rate in the grain is given by [109]:

$$\dot{\varepsilon}_r = \boldsymbol{M}_r \cdot \boldsymbol{B}_r \cdot \bar{\boldsymbol{\sigma}} + \boldsymbol{M}_r \cdot \boldsymbol{b}_r + \dot{\varepsilon}_{0,r} \tag{3-20}$$

The model enforces the assumption that the macroscopic and weighted-average quantities are equal such that $\bar{\dot{\varepsilon}}_r = \langle \dot{\varepsilon}_\mathbf{r} \rangle$, where the "⟨⟩" denotes the weighted average over the grains, using the volume fraction of each grain. The strain rate in the grain can be expressed in terms of the macroscopic constitutive equation, Equation (3-14) [109]:

$$\dot{\varepsilon}_r = \langle \boldsymbol{M_r} \cdot \boldsymbol{B_r} \rangle \cdot \bar{\boldsymbol{\sigma}} + \left\langle \boldsymbol{M_r} \cdot \boldsymbol{b_r} + \varepsilon_{0,r} \right\rangle \tag{3-21}$$

Here the homogeneous compliance and back extrapolated terms are equated from linear and independent terms in the self-consistent equations. When introducing grain shape and orientation general terms can be determined for the macroscopic moduli, and back-extrapolated term [109]:

$$\bar{\boldsymbol{M}} = \langle \boldsymbol{M_r} \cdot \boldsymbol{B_r} \rangle \cdot \langle \boldsymbol{B_r} \rangle^{-1} \tag{3-22}$$

$$\dot{\varepsilon}_0 = \left\langle \boldsymbol{M_r} \cdot \boldsymbol{b_r} + \varepsilon_{0,r} \right\rangle - \langle \boldsymbol{M_r} \cdot \boldsymbol{B_r} \rangle \cdot \langle \boldsymbol{B_r} \rangle^{-1} \cdot \langle \boldsymbol{b_r} \rangle \tag{3-23}$$

Using the general terms increases the robustness, speed, and stability of the convergence procedure.

3.4 VISCOPLASTIC SELF-CONSISTENT ALGORITHM

The local and macroscopic viscoplastic response for a polycrystal can be determined using the following process. Utilising the macroscopic velocity gradient, it can be decomposed into a symmetric strain rate, $\bar{\dot{\varepsilon}}$, and a skew-symmetric rotation rate, $\bar{\dot{\omega}}$. Here an iterative search of the local stress-strain states is performed, using an assumption of the deviatoric stress and moduli.

Starting with an initial guess of the strain rate, the initial stress, moduli, and back-extrapolated term can be calculated from Equation (3-13). These initial guesses allow for the calculation of the macroscopic stress, moduli, and back-extrapolated term from Equation (3-14). Afterwards the interaction tensor and localisation tensors can be found through Equation (3-18) and Equation (3-19), respectively. These tensors can be used to iteratively calculate a new macroscopic moduli and back-extrapolated term using the self-consistent equation, Equation (3-21) [109, 115].

The iteration is predicated on the convergence of the macroscopic moduli, stress, and interaction tensor. Once convergence has been achieved a new grain stress can be determined through the following equation [13, 109]:

$$\dot{\gamma}_0 \sum_s \boldsymbol{m}_s \left(\frac{\boldsymbol{m}_s \cdot \boldsymbol{\sigma}_r}{\tau_0^s} \right)^n - \bar{\dot{\varepsilon}}_0 = -\widetilde{\boldsymbol{M}}(\boldsymbol{\sigma}(\bar{x}) - \bar{\boldsymbol{\sigma}}) \tag{3-24}$$

The new grain stress is checked against the polycrystalline stress, and if the stresses are different a new iteration is needed. If not, the iteration scheme is completed and a new shear rate per grain per deformation mode is calculated through the following equation [13-15, 56, 109]:

$$\dot{\boldsymbol{\gamma}}_{s,r} = \dot{\gamma}_0 \left(\frac{\boldsymbol{m}_s \cdot \boldsymbol{\sigma}_r}{\tau_0^s} \right)^n \tag{3-25}$$

Finally, a new deformation velocity gradient is found through the strain rate and rotation rate determined through the new shear rate. The simplified flow chart of the VPSC algorithm can be found in Figure 3.2, showing the input necessary for simulation and the resulting data outputs.

3.5 COMPOSITE GRAIN MODEL

In order to simulate the twinning deformation of the AZ31 alloy, a composite grain model is used in conjunction with the VPSC model to create alternating lamellae layers of twin and grain domains (Figure 3.1). The lamellae layers of twin-grain interfaces act both as a barrier for dislocation motion and as a new mean free path for dislocations. Further details of the composite grain model can be found in another study [13].

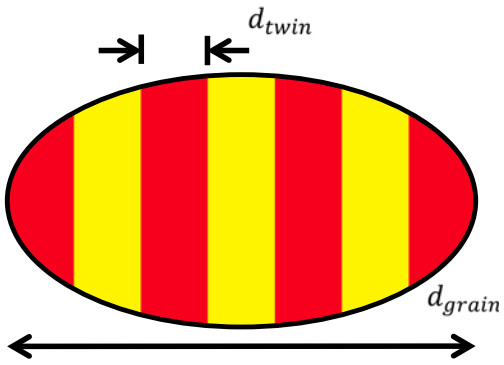

Figure 3.1 Lamellae structure of the composite grain model. The red and yellow regions show the twinned and untwinned grains, respectively. Adapted from [13].

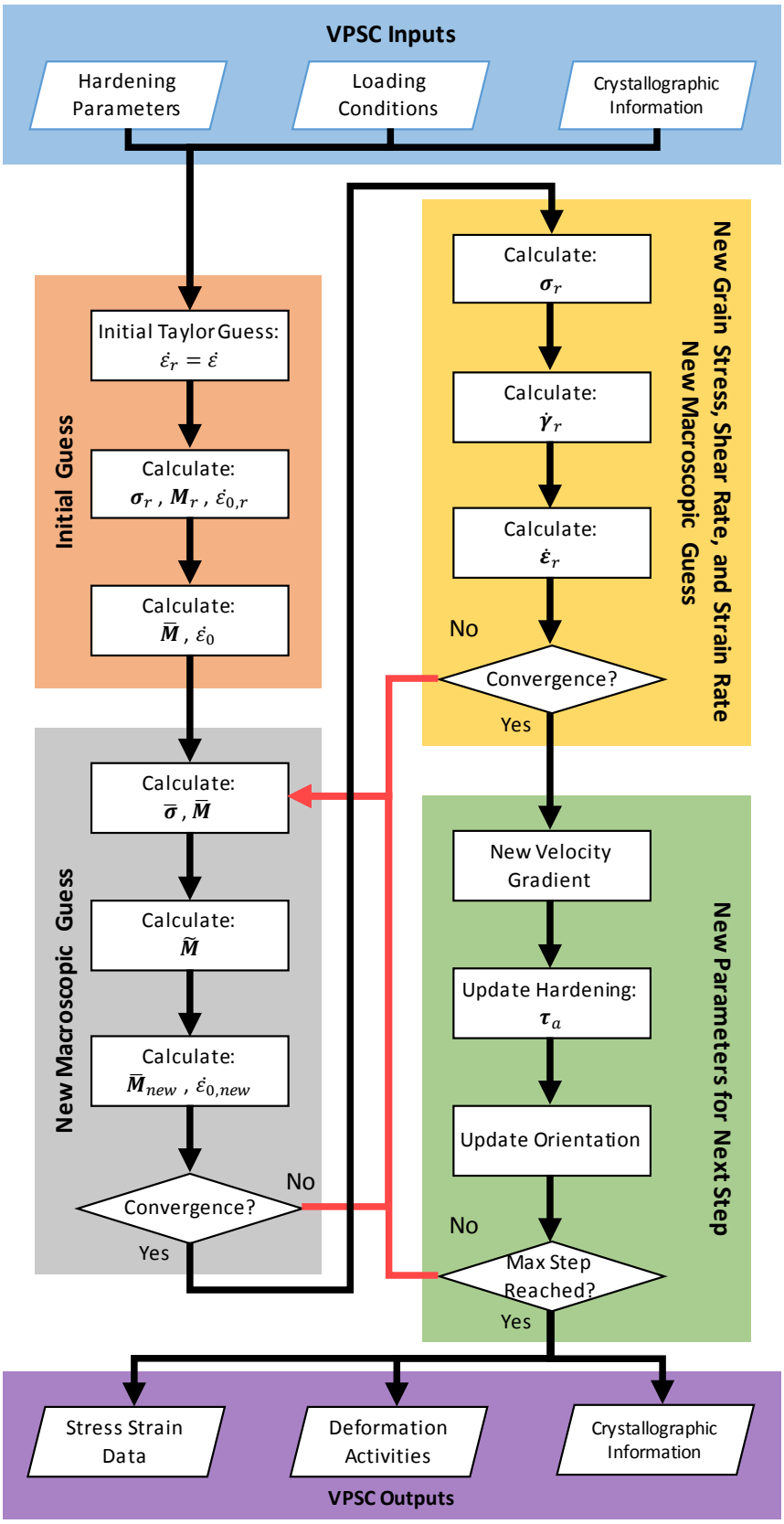

Figure 3.2 Basic flowchart of the VPSC algorithm.

3.6 HARDENING OF SLIP AND TWINNING SYSTEMS

The VPSC model used here also utilises a dislocation density based constitutive law with temperature and strain rate effects to describe the hardening behaviour of the deformation modes [14, 18, 21, 29, 109]. The hardening behaviour is expressed, for one part, through the evolution of the CRSS for slip, τ_{CRSS}^{s}, which is a function of the dislocation density, dislocation-dislocation interactions, dislocation interactions with grain or twin boundaries, and the initial slip resistance [14, 56, 109], according to the following equations:

$$\tau_{CRSS}^{s} = \tau_{0}^{s} + \tau_{for}^{s} + \tau_{deb}^{s} + \tau_{HP}^{s} \tag{3-26}$$

where τ_{0}^{s} is the initial slip resistance, a function of the slip mode, temperature, and strain rate. τ_{for}^{s} and τ_{deb}^{s} are the stresses associated with dislocations, due to forest and debris interactions, and τ_{HP}^{s} expresses the hardening contribution related to the Hall-Petch effect. The forest and debris refer to the interactions that are found between different glissile dislocations on different slip systems, and between glissile dislocations and ordered structures, respectively. These order dislocation structures are formed as a result from the interactions of various glissile dislocations.

The forest interaction term, τ_{for}^{s}, based upon the Mecking and Kocks formulation [116], describes the hardening due to the evolution of the glissile dislocation density randomly distributed within the grain [14, 57, 109, 116, 117];

$$\tau_{for}^{s} = \mu \boldsymbol{b}_{s} \sqrt{\rho_{for}^{s} \chi} \tag{3-27}$$

where μ is the shear modulus, $\boldsymbol{b}_{\mathrm{s}}$ is the Burger's vector, ρ_{for}^{s} is the glissile dislocation density for a deformation mode, and χ is the interaction matrix. During deformation, the dislocation density evolution is a thermally controlled mechanism and varies according

to the generation and annihilation of dislocations within a polycrystalline material [14, 109, 116]:

$$\frac{\partial \rho^s}{\partial \gamma^s} = k_1 \sqrt{\rho_{for}^s} - k_2^s \rho_{for}^s \tag{3-28}$$

where k_1 is a material constant, and k_2 is a function of strain and temperature. It is important to note that k_2^s is also a function of both drag stress and the interaction matrix [14, 109, 116]:

$$\frac{k_2^s}{k_1} = \frac{\boldsymbol{b}_s \left(\sigma_{drag} - \frac{kT}{\boldsymbol{b}_s{}^3} ln \frac{\dot{\varepsilon}}{\dot{\varepsilon}_0} \right)}{\sqrt{\chi} \sigma_{drag} Q_d} \tag{3-29}$$

where σ_{drag} is the drag stress, k is the Boltzmann's constant, T is the temperature, $\dot{\varepsilon}$ is the strain rate, $\dot{\varepsilon}_0$ is the reference strain rate, and Q_d is the activation energy for deformation.

The debris interaction term, τ_{deb}^s, correlates with the stored dislocations locked into stable structures or ordered distributions of dislocations in a grain, which is expressed as [14, 56, 109]:

$$\tau_{deb}^s = 0.086 * \chi \sqrt{\rho_{deb}^s} \, ln \left(1/\boldsymbol{b}_s \sqrt{\rho_{deb}^s} \right) \tag{3-30}$$

where ρ_{deb} is the stored dislocation density. Lastly, the grain size effects are established within the model using the following equation [14, 56, 109];

$$\tau_{HP}^s = HP_s \mu \sqrt{\vec{b}_s / d} \tag{3-31}$$

where HP_s is a dimensionless constant, and d is the grain size, or the mean free path accounting for the twin presence in the microstructure.

In order to simulate the twinning deformation of the AZ31 alloy, a composite grain twin is used in parallel with the VPSC model to create alternating lamellae layers of twin and untwinned domains [13]. The hardening is also expressed through the evolution of the CRSS for twinning, τ_{CRSS}^{t}, which is function of the initial twin propagation resistance, the latent hardening of the twins as a result of the slip dislocation density, and the grain size effect [14, 56]:

$$\tau_{CRSS}^{t} = \tau_{*}^{t} + \tau_{LH}^{t} + \tau_{HP}^{t} \tag{3-32}$$

where t represents the twinning system, τ_{*}^{t} is the initial twin propagation resistance, τ_{LH}^{t} is latent hardening of twins, and τ_{HP}^{t} expresses the stress related to the Hall-Petch effect. τ_{HP}^{t} for the twins can be evaluated in the same manner through Equation (3-31), however, instead of the grain size, the mean free path of the twinning system is used [13, 14].

The onset of twining is associated with a yield stress, σ_{nuc}, to commence the nucleation of a twin. When the local stress has not reached this yield stress the initial twin propagation resistance is equal to a critically high value, τ_{crit}^{t}. However, if nucleation occurs, the initial twin propagation resistance is equal to τ_{prop}^{t}, which is a constant for a fully formed twin. Therefore the initial twin propagation resistance can range between τ_{crit}^{t} and τ_{prop}^{t} [14, 56];

$$\tau_{*}^{t} = \tau_{prop}^{t} + \left(\tau_{crit}^{t} - \tau_{prop}^{t}\right) * P \tag{3-33}$$

where τ_{crit}^{t} and τ_{prop}^{t} are the critical shear stress for nucleation and the shear stress for propagation, and P is the probability function for the twin nucleation. Lastly, the latent hardening term determines the contribution of hardening as a result of the interactions between the dislocations and twins [14, 56];

$$\tau_{LH}^{t} = \mu \Sigma_s C^{ts} \boldsymbol{b}_t \boldsymbol{b}_s \rho_{for}^{s} \tag{3-34}$$

where C^{ts} is the latent hardening parameter, and $\boldsymbol{b}_t$ is the Burger's vector for the dislocations within the twinned grains.

3.7 IMPROVEMENTS ON THE TEMPERATURE DEPENDENT MODEL

The current VPSC model employs temperature dependent variables, namely the threshold stress, τ_0^s, enabling the model to be versatile to predict the stress-strain response for many loading conditions and materials. However, some terms in the VPSC model, described in the previous section, are temperature sensitive, however, have been set as a constant. This leads to the inaccuracies for low-moderate temperature modelling of Mg alloys, as there is a variety of active deformation mechanisms, which are temperature sensitive (slip and DRX) and temperature insensitive (twinning). Here a newly proposed VPSC model, known as VPSC-T, is able to utilise a single set of parameters and accurately model Mg AZ31 deformation under varying loading conditions. The main modifications concern the dislocation-dislocation interaction matrix and drag stresses, which are dependent on temperature, and are described in detail in the following sections.

3.7.1 Interaction Matrix

Mg and its alloys have a total of 18 slip systems from the three active slip modes; basal, prismatic, and pyramidal slip modes contain 3, 3, and 12 slip systems, respectively. Equations (3-27) and (3-28) utilise the interaction matrix to evaluate the latent hardening evolution as a result of the dislocation-dislocation interaction with other stored dislocations, Table 3.1 lists all the different interaction types that are possible for Mg alloys [32, 50, 118].

Table 3.2 shows an example of an interaction matrix defining all the interaction types as described in Table 3.1, indicated by the coefficients [50]. The primary system represents all the glissile dislocations found within a system, while the forest system represents the stored dislocations that the primary system interacts with.

Table 3.1 List of dislocation-dislocation interaction types found in magnesium alloys.

#	Interaction Type	#	Interaction Type
S1	Self-Interaction – Basal	8	Non-Collinear Basal/Pyramidal
S2	Self-Interaction – Prismatic	9	Semi-Collinear Prismatic/Pyramidal
S3	Self-Interaction – Pyramidal	10	Non-Collinear Prismatic/Pyramidal
1	Coplanar Basal/Basal	11	Semi-Collinear Pyramidal/Basal
2	Non-Coplanar Prismatic/Prismatic	12	Non-Collinear Pyramidal/Basal
3	Collinear Basal/Prismatic	13	Semi-Collinear Pyramidal/Prismatic
4	Non-Collinear Basal/Prismatic	14	Non-Collinear Pyramidal/Prismatic
5	Collinear Prismatic/Basal	15	Semi-Collinear Pyramidal/Pyramidal
6	Non-Collinear Prismatic/Basal	16	Non-Collinear Pyramidal/Pyramidal
7	Semi-Collinear Basal/Pyramidal		

Table 3.2 Example of an interaction matrix detailing the dislocation-dislocation interactions.

		Forest System																
		A	B	C	D	E	F	G	H	I	J	K	L	M	N	O	P	Q	R
Primary System																			
A	Basal-1	S1	1	1	3	4	4	7	8	8	7	8	8	7	8	8	7	8	8
B	Basal-2	1	S1	1	4	3	4	8	7	8	8	7	8	8	7	8	8	7	8
C	Basal-3	1	1	S1	4	4	3	8	8	7	8	8	7	8	8	7	8	8	7
D	Prismatic-1	5	6	6	S2	2	2	9	10	10	9	10	10	9	10	10	9	10	10
E	Prismatic-2	6	5	6	2	S2	2	10	9	10	10	9	10	10	9	10	10	9	10
F	Prismatic-3	6	6	5	2	2	S2	10	10	9	10	10	9	10	10	9	10	10	9
G	Pyramidal-1	11	12	12	13	14	14	S3	16	16	15	16	16	15	16	16	15	16	16
H	Pyramidal-2	12	11	12	14	13	14	16	S3	16	16	15	16	16	15	16	16	15	16
I	Pyramidal-3	12	12	11	14	14	13	16	16	S3	16	16	15	16	16	15	16	16	15
J	Pyramidal-4	11	12	12	13	14	14	15	16	16	S3	16	16	15	16	16	15	16	16
K	Pyramidal-5	12	11	12	14	13	14	16	15	16	16	S3	16	16	15	16	16	15	16
L	Pyramidal-6	12	12	11	14	14	13	16	16	15	16	16	S3	16	16	15	16	16	15
M	Pyramidal-7	11	12	12	13	14	14	15	16	16	15	16	16	S3	16	16	15	16	16
N	Pyramidal-8	12	11	12	14	13	14	16	15	16	16	15	16	16	S3	16	16	15	16
O	Pyramidal-9	12	12	11	14	14	13	16	16	15	16	16	15	16	16	S3	16	16	15
P	Pyramidal-10	11	12	12	13	14	14	15	16	16	15	16	16	15	16	16	S3	16	16
Q	Pyramidal-11	12	11	12	14	13	14	16	15	16	16	15	16	16	15	16	16	S3	16
R	Pyramidal-12	12	12	11	14	14	13	16	16	15	16	16	15	16	16	15	16	16	S3

Bertin *et al.* found values for the dislocation-dislocation interaction for pure Mg calculated through a discrete dislocation dynamics study (see Table 3.3) [50], which shows that the interactions are generally lower than the 0.5 and 0.9 values used by other authors [15, 42, 58, 85, 92].

Table 3.3 Coefficient of dislocation-dislocation interactions in pure Mg [50].

Coefficient	Value	Coefficient	Value	Coefficient	Value	Coefficient	Value
S1	-	3	0.707	8	0.293	13	0.025
S2	-	4	0.054	9	0.068	14	0.015
S3	-	5	0.535	10	0.088	15	0.018
1	-	6	0.060	11	0.017	16	0.042
2	0.038	7	0.367	12	0.011		

The complexity in describing the mechanical behaviour of Mg alloys is increased by the fact that all these deformation mechanisms can interact with one another. Dislocation-dislocation interactions can be grouped into six different categories, (1) glissile junctions, (2) Hirth junctions, (3) Lomer Junction, (4) collinear, (5) coplanar, and (6) self-interactions [118]. Computational studies use an interaction matrix to evaluate the strain hardening evolution due to these dislocation-dislocation interactions [116]. This matrix is commonly populated by constants (or even a single constant in some cases) to describe each type of latent hardening behaviour [14, 15, 42, 58, 85, 92, 119] for Mg AZ31. However, Lavrentev [117] has determined that the interaction matrix is a material parameter dependent on a variety of factors, including deformation rate, dislocation distribution/concentration, crystal orientation, alloying elements, and temperature. In particular, Lavrentev noted that temperature has an inverse relationship with components of this interaction matrix [117]. Overall, the interaction matrix plays a pivotal role in the hardening of a polycrystal [119], and as such, the development of an accurate interaction matrix is critical in crystal plasticity modelling to increase prediction accuracy.

In this new model, the coefficients for the interaction matrix are also dependent on the deformation temperature, due to the temperature sensitive nature of the dislocation-dislocation interactions [117]; an expression for the temperature dependent interaction matrix was also formulated [56, 120]. The values of the interaction matrix are given a multiplier to make the value decrease with increasing temperature [121]:

$$\chi_{temp} = \chi * M \tag{3-35}$$

where χ is the original value in the interaction matrix, M is the interaction matrix value multiplier, and χ_{temp} is the new value in the interaction matrix at a given temperature.

3.7.2 Drag Stress

Drag stress is a type of internal thermodynamic force acting on a material that retards dislocation motion [122] and is used to characterise the dislocation density and morphology [123]. Notably, drag stress influences the strain hardening behaviour of a given slip mode and can be used to couple the kinematic hardening behaviour [122, 124]. Historically, the drag stress is often regarded a constant [21, 124, 125], but it can also be regarded as equivalent to the yield strength [126], dependent on strain hardening [124, 125], or dependent on the deformation temperature [29, 124]. As the temperature increases there will be increased slip activity, as such the drag stress for each slip mode also plays an important role in the mechanical response of the material.

A number of authors have modelled the drag stresses of basal, prismatic, and pyramidal slip in Mg alloys across various temperatures, closely matching experimental results [21, 29, 47]. The drag stresses used in these studies are tabularised in Table 3.4. Some of these authors have the drag stresses as a constant regardless of the deformation temperature [29, 47], or investigations are focused on a single temperature [21, 127-130].

Table 3.4 Drag stresses for basal, prismatic, and pyramidal slip in different Mg alloys.

Temperature (°C)	Materials	Drag Stresses (MPa)			References
		Basal	Prismatic	Pyramidal	
25	Pure Mg	10000	3400	80	[21]
-	Pure Mg	-	-	10	[127]
-	Pure Mg	-	200	-	[128]
-	Pure Mg	650	-	-	[129]
25	WE43	245	250	285	[130]
25	Mg-4Li	1500	40537	3300	[29]
200	Mg-4Li	1500	3307	3300	[29]
25-150	AZ31	100	150	225	[47]

Risse *et al.* [29] noted the drag stresses decreased exponentially with increasing temperature for basal, prismatic, and pyramidal slip in Mg alloys. Risse *et al*. also concluded that the kinetics of the dynamic recovery of prismatic slip is more temperature sensitive than that found in either basal or pyramidal slip [29]. This is theorised to be a result of prismatic slip favourability for cross-slip or due to the highly thermally activated glide. Zecevic *et al.* [60] utilises Risse's drag stress formulation to simulate the texture evolution due to $\langle c + a \rangle$ pyramidal slip in Mg-4Li at room temperature to 200 °C.

Furthermore, Sehitoglu *et al.* [123] developed a complex model for the drag stress found in 319-T6 aluminium-copper alloy with regards to secondary dendritic arm spacing (SDAS). Here the dendritic arms could be interpreted or viewed as twin grains, and the drag stress is a function of temperature, where the drag stress is monotonically decreasing with increasing temperature, from 122 MPa at room temperature to 105 MPa at 250 °C [123].

In this study, we have adopted a similar approach to describe the relationship between drag stress and temperature as shown by Equation (3-36), where the values for basal and pyramidal slip are calculated to be slowly decreasing contrary to prismatic slip, which is highly temperature sensitive according to Risse *et al.* [29].

$$\sigma_{drag} = A_s - B_s * T \tag{3-36}$$

where A_s and B_s are material constants dependent on the slip mode.

Chapter 4 | Results and Discussions of the Temperature Sensitive Model

4.1 Material

The temperature sensitive model is used to predict the mechanical behaviour and textural evolution of a Mg alloy AZ31, which has a chemical composition of 3wt.%-Al, 1 wt.%-Zn, and 0.5 wt.%-Mn. This alloy was hot rolled into a plate with a thickness of 25 mm and was subsequently annealed for 12 hours at 350 °C in an argon atmosphere. After the rolling and annealing processes, the average grain size is 25 μm and this material has a strong basal texture as shown in Figure 4.1. Flat dog-bone tensile specimens were cut from the plate in three different directions: ND, TD, and ND45 as illustrated in Figure 4.1. The ND45 direction lies on the ND-RD plane. Tensile testing was conducted at 25 °C, 100 °C, 150 °C, and 200 °C in each of the three orientations, ND, TD, and ND45, using a constant strain rate of $5 \times 10^4\ s^{-1}$ by collaborators at Texas A&M University, College Station, TX, USA [8].

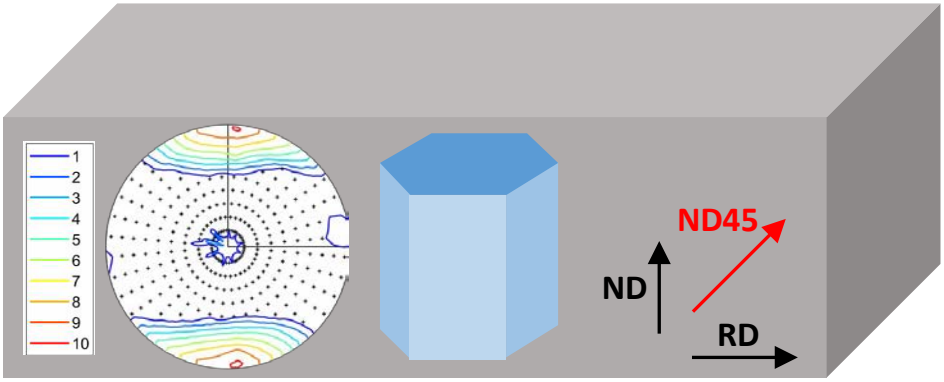

Figure 4.1 Initial texture of the AZ31 alloy shown with respect to the unit cell and plate directions.

These directions were chosen such that the loading directions are parallel to, perpendicular to, and at 45° from the unit cell c-axis, respectively, in order to highlight

the anisotropic nature of the material. The loading directions in line with the c-axis preferentially deform through the activation of tensile twinning [7, 9, 16-18, 20, 22, 28, 31, 39, 43, 51, 55, 56], while prismatic slip is activated when the loading direction is perpendicular to the c-axis [9, 17, 19, 39, 41]. Lastly, the loading direction 45° offset from the c-axis was selected to maximise basal slip activity [8, 9, 17]. Different loading directions are chosen to activate different deformation mechanisms at different temperatures, due to anisotropy achieved by the highly textured hot-rolled plate. Further data and analysis on that material can be found in [8].

4.2 VISCOPLASTIC SELF-CONSISTENT PARAMETERS

4.2.1 Slip and Twinning Hardening Parameters

The hardening parameters used in this study for slip and twinning are included in Tables 4.1 and 4.2, respectively, which were determined through physical experimental data. The τ_0^s values used in this study are obtained from different studies under different temperatures [18, 56, 131]. These values were combined together in the form expressed in Table 4.1, which are based on Li's study [18]. Figure 4.2 shows the resulting τ_0^s values as a function of temperature.

Table 4.1 Hardening parameters for slip deformation. Temperature for τ_0^s calculation is in Kelvin.

	Units	$\langle a \rangle$ Basal	$\langle a \rangle$ Prismatic	$\langle c+a \rangle$ Pyramidal	References
$\boldsymbol{b}_s$	nm	0.32	0.32	0.61	-
k_1	M	5.6×10^8	8.1×10^8	2.5×10^{11}	[18, 132]
$\dot{\varepsilon}_0$	s^{-1}	1×10^7	1×10^7	1×10^7	-
τ_0^s	MPa	$100\, exp\left(-\frac{T(K)}{90}\right)$	$150\, exp\left(-\frac{T(K)}{200}\right)$	$8.5E5\, exp\left(-\frac{T(K)}{40}\right)$	[18, 56, 131]
HP_s	-	75	150	10	-

Table 4.2 Hardening parameters for twinning deformation.

	$\{10\bar{1}2\}$ Tensile twinning	$\{10\bar{1}1\}$ Compressive twinning		References
τ_{crit}	35 MPa	150 MPa		[18, 21]
τ_{prop}	50 MPa	150 MPa		[18, 21]
HP_s	175	200		[18]
$\boldsymbol{b}_t$	0.049 nm	0.135 nm		-
C^{ts}	1	–	$\langle a \rangle$ Basal	[22]
	1	–	$\langle a \rangle$ Prismatic	[22]
	10	–	$\langle c + a \rangle$ Pyramidal	[22]

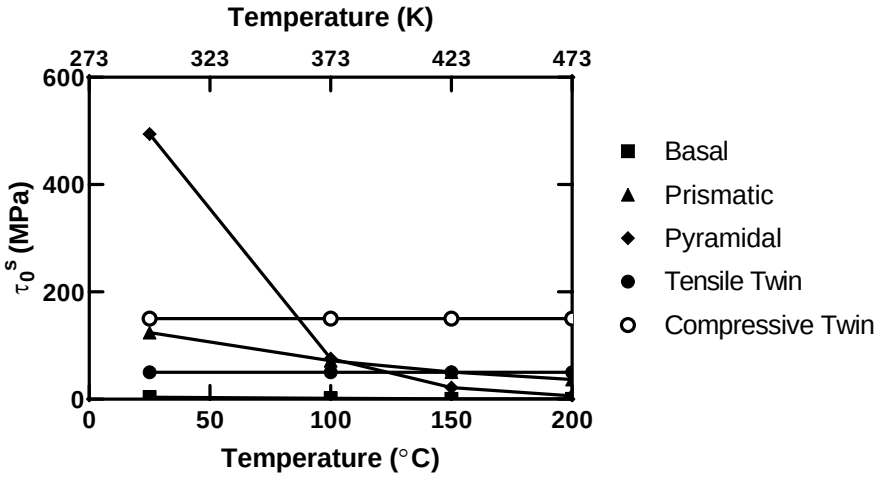

Figure 4.2 τ_0^s value evolution with temperature for the different deformation mechanisms.

4.2.2 Temperature Sensitive Model Parameters

The newly developed VPSC-T model utilises a temperature sensitive interaction matrix and drag stresses in order to accurately predict the deformation modes participating in strain accommodation in Mg alloys. The interaction matrix value multipliers used are given in Table 4.3 and were determined through a fitting process with the experimental data. The formula calculating the drag stress values used in this model can be found in Table 4.4, which are based upon experimental values found in literature [21, 29, 47, 127-130], and their resulting evolution with temperature is shown in Figure 4.3. The resulting

drag stress values in Figure 4.3 show that the drag stresses for pyramidal and basal slip are not highly sensitive to temperature, while the drag stress for prismatic slip are. Figure 4.3 reflects the observed experimental behaviour of the drag stresses in Mg alloys for each slip mode [21, 29, 123].

Table 4.3 Interaction matrix multipliers for basal, prismatic, and pyramidal slip systems.

Slip Mode	Temperature (°C)			
	25	100	150	200
Basal	1.000	0.800	0.700	0.650
Prismatic	1.000	0.850	0.785	0.750
Pyramidal	1.000	0.825	0.750	0.700

Table 4.4 Parameters for drag stresses in the basal, prismatic, and pyramidal slip systems.

Slip Mode	A_s (MPa)	B_s (MPa/K)
Basal	560	1.166
Prismatic	7250	12.919
Pyramidal	160	0.268

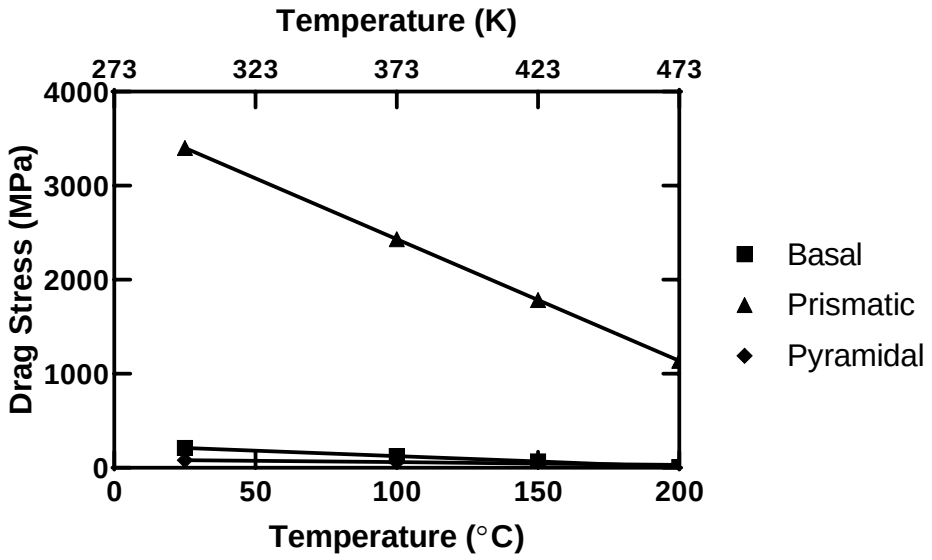

Figure 4.3 Drag stresses as a function of temperature for basal, prismatic, and pyramidal slip.

4.3 RESULTS

4.3.1 Normal Direction (ND)

The simulation true stress-strain curves are represented by the dotted curves in Figure 4.4 and they are in agreement with the experimental curves represented by the solid lines for all temperatures. It should be noted that all future stresses and strains noted are referring to true stresses and true strains. The stress-strain curves at room temperature and 100 °C both exhibit a downward curvature, or an "S" shape curve, indicative of a twinning predominant deformation (see Figure 2.9a). As temperature rises to 150 °C and 200 °C, this downward curvature is no longer evident and the curves morph into more "traditional" stress-strain curve (see Figure 2.6a), indicating increased slip activity with temperature such that slip deformation becomes the predominant deformation mode. Lastly, at 200 °C the stress-strain curve decreases after it reaches a peak stress at $\varepsilon = 10\%$, showing signs of softening that is attributed to DRX (see Figure 2.11a).

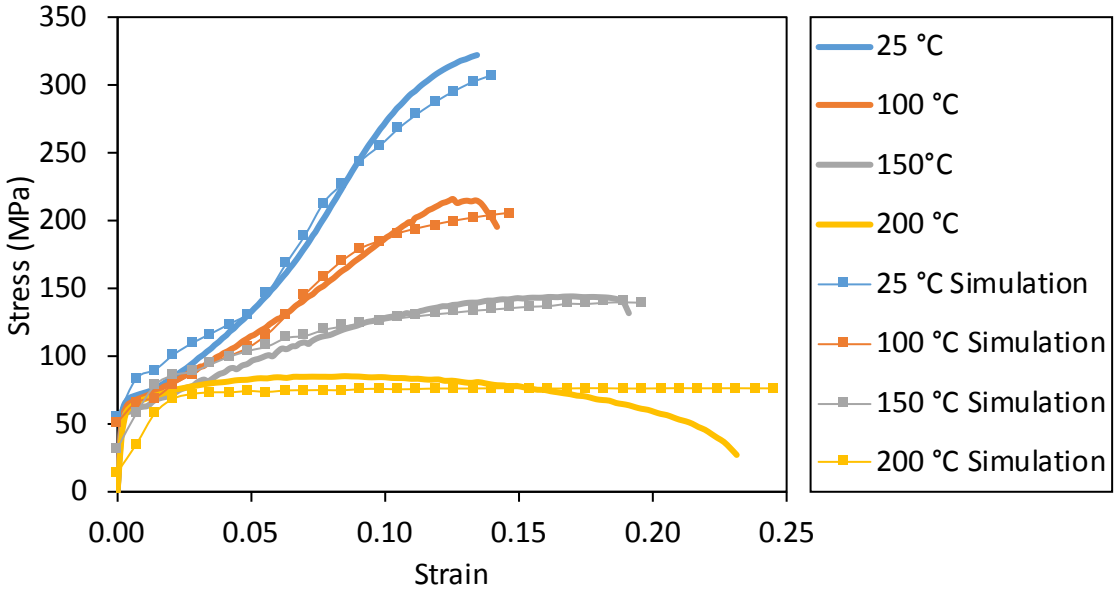

Figure 4.4 Stress-strain curves of AZ31 for loading in the normal direction at: 25 °C (in blue), 100 °C (in orange), 150 °C (in grey), and 200 °C (in yellow). The dotted lines represent the simulation results while the solid lines represent the experimental data.

The experimental work hardening curves are shown in Figure 4.5, it should be noted that these curves have been smoothed in an effort to reduce the noise in the data. At room temperature and 100 °C, the work hardening curves both have a decreasing curve followed by an increase in the hardening rate near the yield strength ($\sigma_{yield} \approx 75$ MPa) before decreasing at a higher stress. These curves create a cubic parabola, which suggests that twinning is the predominant deformation mechanism (see Figure 2.9b). For 150 °C the presence of twinning is not as definitive as with the two lower temperatures but there is a slight rise in the hardening before decreasing again. At 200 °C there is no increase in the hardening after yielding, and the curve decreases to zero, which indicates slip as the predominant deformation mode (see Figure 2.6b). Additionally, the work hardening curve decreases into the negatives, whilst the stress decreases. This behaviour of the work hardening curve is indicative of DRX (see Figure 2.11).

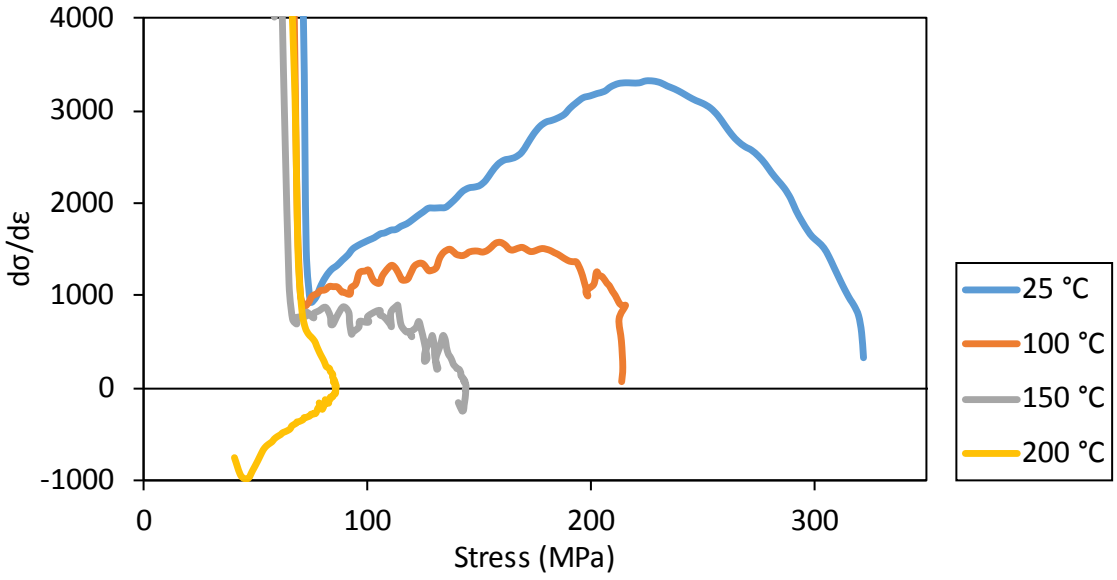

Figure 4.5 Work hardening curves of AZ31 for loading in the normal direction at: 25 °C (in blue), 100 °C (in orange), 150 °C (in grey), and 200 °C (in yellow).

All the activities within the ND case at various temperatures can be found in Figure 4.6. The yellow line illustrates the tensile twin activity and can be seen at all temperatures. While Figure 4.4 and Figure 4.5 depicts deformation slip as the predominant deformation mode at elevated temperatures, it should be noted that there is a significant degree of tensile twin activity. The twinning activity can be quantified through the black lines in Figure 4.6, at room temperature after a strain of $\varepsilon = 10\%$ there is 70% volume fraction of tensile twins, and at 200 °C the volume fraction decreases to 15% at a strain of $\varepsilon = 15\%$. At strain levels of $\varepsilon = 5\%$, there is significant hardening for twinning, resulting in a decrease in twinning activity. Basal activity, highlighted by the blue line, is active at all temperatures, which is expected as the CRSS value for basal slip is the lowest of all the deformation modes. Consequently, there is an increase in the overall slip activity with the introduction of prismatic slip, as indicated by the orange activity line in Figure 4.6a.

At 100 °C, the deformation activities for basal slip and tensile twinning are identical to room temperature, however, after tensile twinning has hardened ($\varepsilon = 5\%$) prismatic and pyramidal slip become active, as shown by the orange and grey curves, respectively, in Figure 4.6. At 150 °C pyramidal slip becomes the predominant deformation mode at a strain $\varepsilon = 7.5\%$, after tensile twinning has hardened. Prior to this, the deformation activities are similar to those found at room temperature and 100 °C. At 200 °C the main deformation modes that are active are basal and pyramidal slip and there is a small contribution from tensile twinning to strain accommodation. Despite the minimal levels of activity of tensile twinning, there is a 10% volume fraction of tensile twins, smaller than those obtained at the three other temperatures.

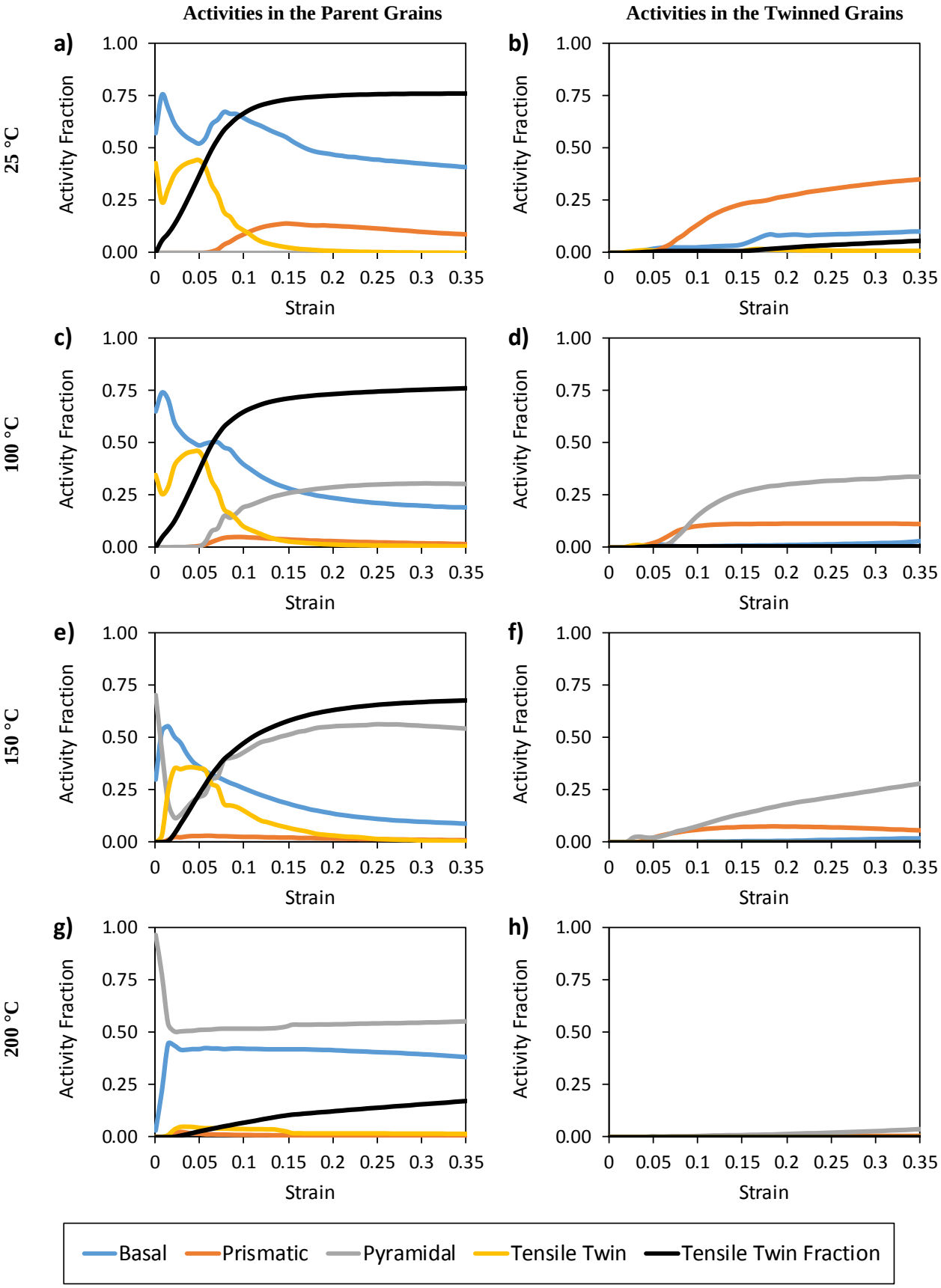

Figure 4.6 Predicted activities in the parent (a, c, e, and g) and twinned (b, d, f, and h) grains for loading in the normal direction at: (a, b) 25 °C, (c, d) 100 °C, (e, f) 150 °C, and (g, h) 200 °C

Similarly, to what was observed in the parent grains, pyramidal slip is only active at elevated temperatures in the twinned grains. Prismatic slip and, to a lower extent, basal slip are accommodating strain in twinned grains at room temperatures and the activities of these two modes decreases as temperature increases. The compressive twinning activity and volume fraction have been omitted from Figure 4.6 as they are negligible at all temperatures. A similar observation has been found across all the loading conditions, and as such all compressive twinning activities and volume fraction will also be omitted for the two other loading directions.

The experimental and predicted (0001) pole figures (PF) for the four different temperatures are shown in Figure 4.7. Initially, the (0001) PF (Figure 4.1) presented a strong basal texture with most grains having their c-axis parallel to the ND direction. At room temperature, tensile twinning causes significant microstructural textural changes as we can see in the experimental and simulated PF with now most grains' c-axis oriented normal to ND. With increasing temperatures, the model predicts a noticeable decrease in tensile twinning activity (Figure 4.6) and therefore a reduction in the twin volume fraction. This is observed in our experimental and simulated PFs as a large fraction of grains have their c-axis orientated along ND. The experimental PFs also illustrate the same tensile twinning microstructural changes with a similar increase of intensity across the centre of the PF. Furthermore, this reduction of the twin volume fraction is also categorised by an increase in the original basal textures at the top and bottom of the simulation PFs, with increasing temperature.

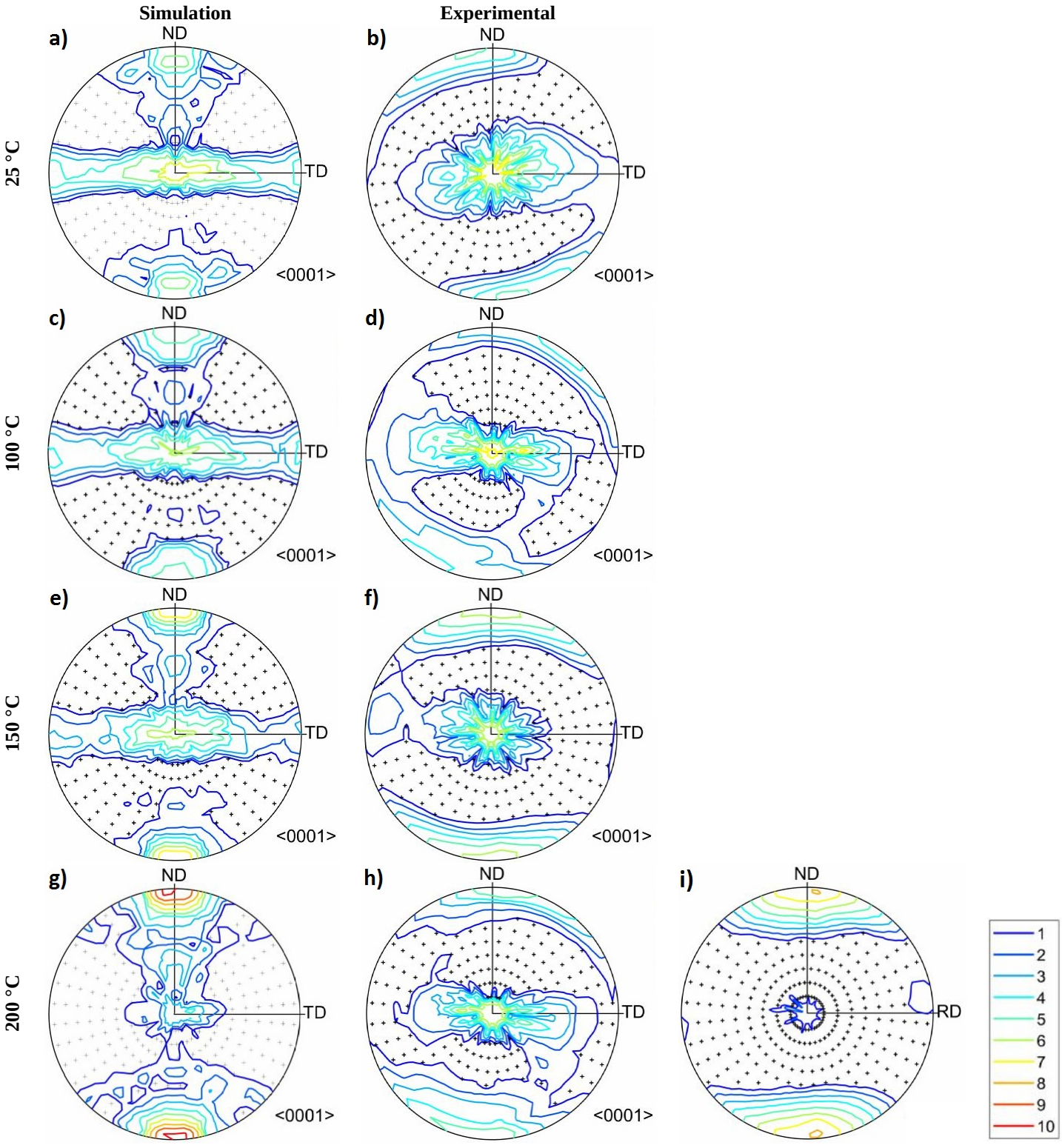

Figure 4.7 Pole figures of simulation and experimental for loading in the normal direction. The simulation pole figures are taken at a strain of 0.14 at 25 °C, a strain of 0.14 at 100 °C, a strain of 0.175 at 150 °C, and a strain of 0.21 at 200 °C. The initial texture (i) is included for comparison.

At elevated temperatures, the experimental PF shows a similar decrease in the intensity peak when compared to the predicted PF. However, the experimental PF still has a significant twinned grain volume fraction that was not predicted by the model. One probable possibility for this discrepancy is the fact that the experimental texture measurements were conducted close to the fracture surface where large twinning activity is expected. Other possibilities include the activation of double twinning, $\langle a \rangle$ pyramidal slip, and 2nd order pyramidal slip that are not included in the current model, as well as other slip-twin interactions, which could potentially alter the microstructure. It should be noted that due to the presence of DRX, grains are formed with random crystallographic orientation, which the current model does not capture.

4.3.2 Transverse Direction (TD)

In the transverse direction, the stress-strain curves at the four different temperatures (Figure 4.8) have the same shape for both experimental and simulation results, with the yield strength decreasing as the temperature increases. The downward curvature indicative of twinning, as seen in Figure 4.4, does not exist suggesting that the predominant deformation mode for loading along TD is dislocation slip (see Figure 2.6a). The predominant deformation mechanism can once again be qualitatively determined through the work hardening curves (Figure 4.9), wherein the slope of the work hardening curve is consistently negative, indicative of slip deformation (see Figure 2.6b).

When temperatures reach 150 °C and above, there is a softening phenomenon in the stress-strain curve due to DRX, akin to what was observed in the ND loading case at 200°C. Additionally, this softening effect is also observed at 100 °C at a lesser extent than at the two higher temperatures. The work hardening curves, shown in Figure 4.9, also

show this softening effect with a decrease in the hardening rate to a negative value as well as a sudden decrease in the stress when the hardening is equal to zero, depicted by a "hook" shape (see Figure 2.11b).

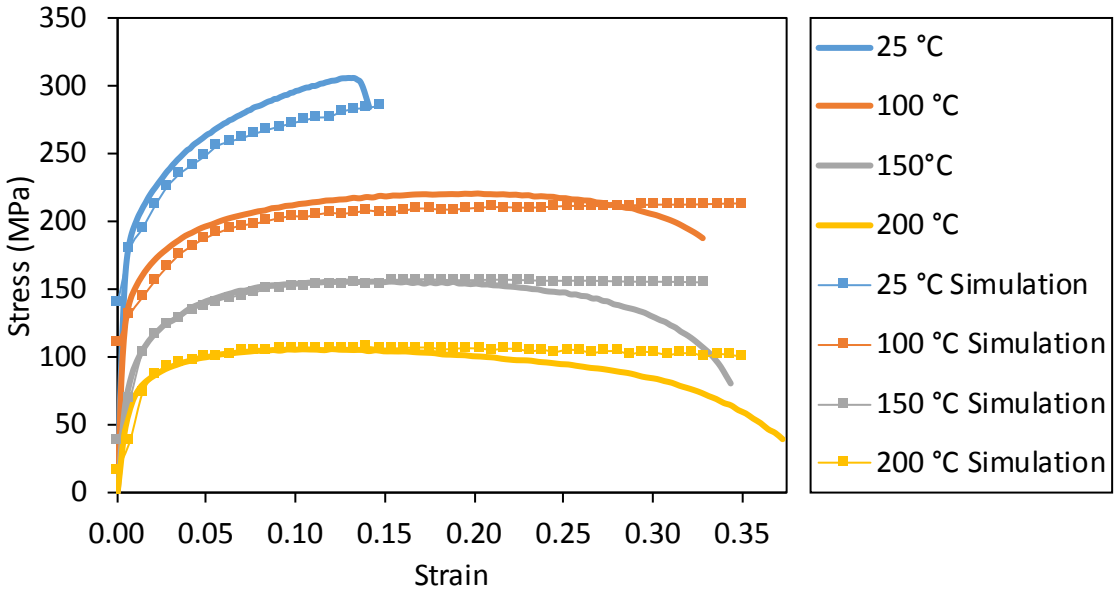

Figure 4.8 Stress-strain curves of AZ31 for loading in the transverse direction at: 25 °C (in blue), 100 °C (in orange), 150 °C (in grey), and 200 °C (in yellow). The dotted lines represent the simulation results while the solid lines represent the experimental data.

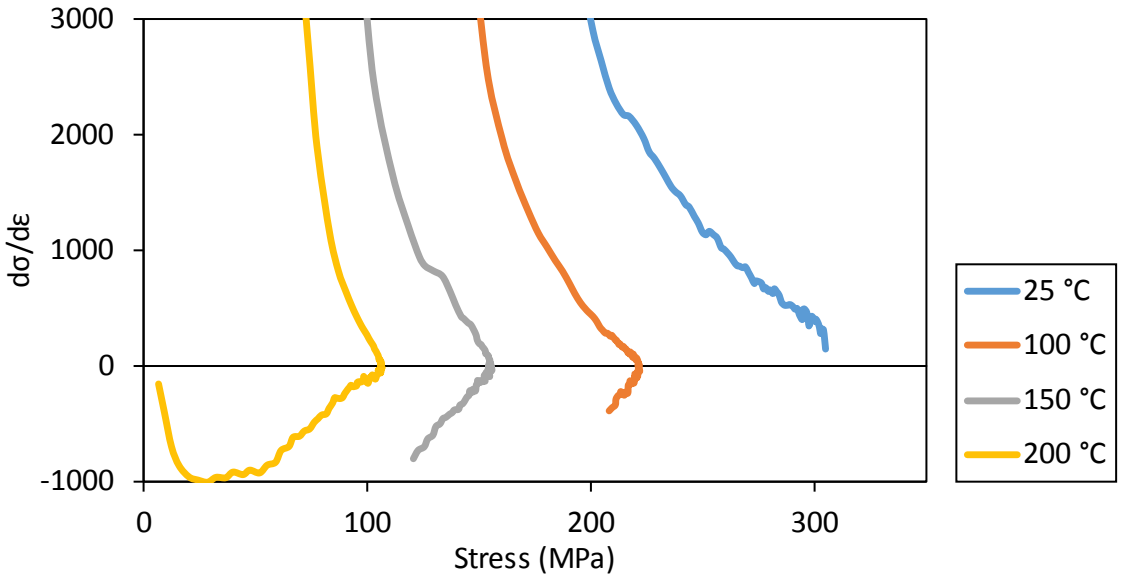

Figure 4.9 Work hardening curves of AZ31 for loading in the transverse direction at: 25 °C (in blue), 100 °C (in orange), 150 °C (in grey), and 200 °C (in yellow).

While loading in the transverse direction, the specimens do not experience a large amount of tensile twinning, indicated by the yellow and black lines in Figure 4.10. While tensile twins do occur at low strains up until $\varepsilon = 1\%$, it results in a twin grain volume fraction of 7% at room temperature and 5% at 200 °C. At room temperature basal slip is the predominant deformation model, until $\varepsilon = 5\%$ at which point the prismatic slip replaces basal slip as the predominant deformation mode. At 150 °C and 200 °C, the deformation mode at lower strains is a combination of prismatic and basal slip, and when the strain reaches 6% pyramidal slip becomes the predominant deformation mode.

In the TD cases, the main deformation mechanism is slip deformation, which does not cause large grain rotations. This implies that the deformed textures (Figure 4.11) are quite similar to the initial texture (Figure 4.1). Both experimental and simulated PF are in agreement with that statement, with similar intensity levels of the strong basal textures across all the deformation temperatures. The main difference between the experimental and simulated PFs is the orthotropic symmetry displayed by the experimental PFs and

that is absent in the simulated ones. The small amount of tensile twinning predicted by the model results in the two small peaks as indicated by the black arrows in Figure 4.11.

Furthermore, at 100 °C the experimental and simulation PFs closely resemble with one and another, as the orthotropic texture seen at the other temperatures is no longer present. This shows the variability of the deformed texture at different testing points, which supports the hypothesis that the experimental PFs were conducted close to or at the fracture surface.

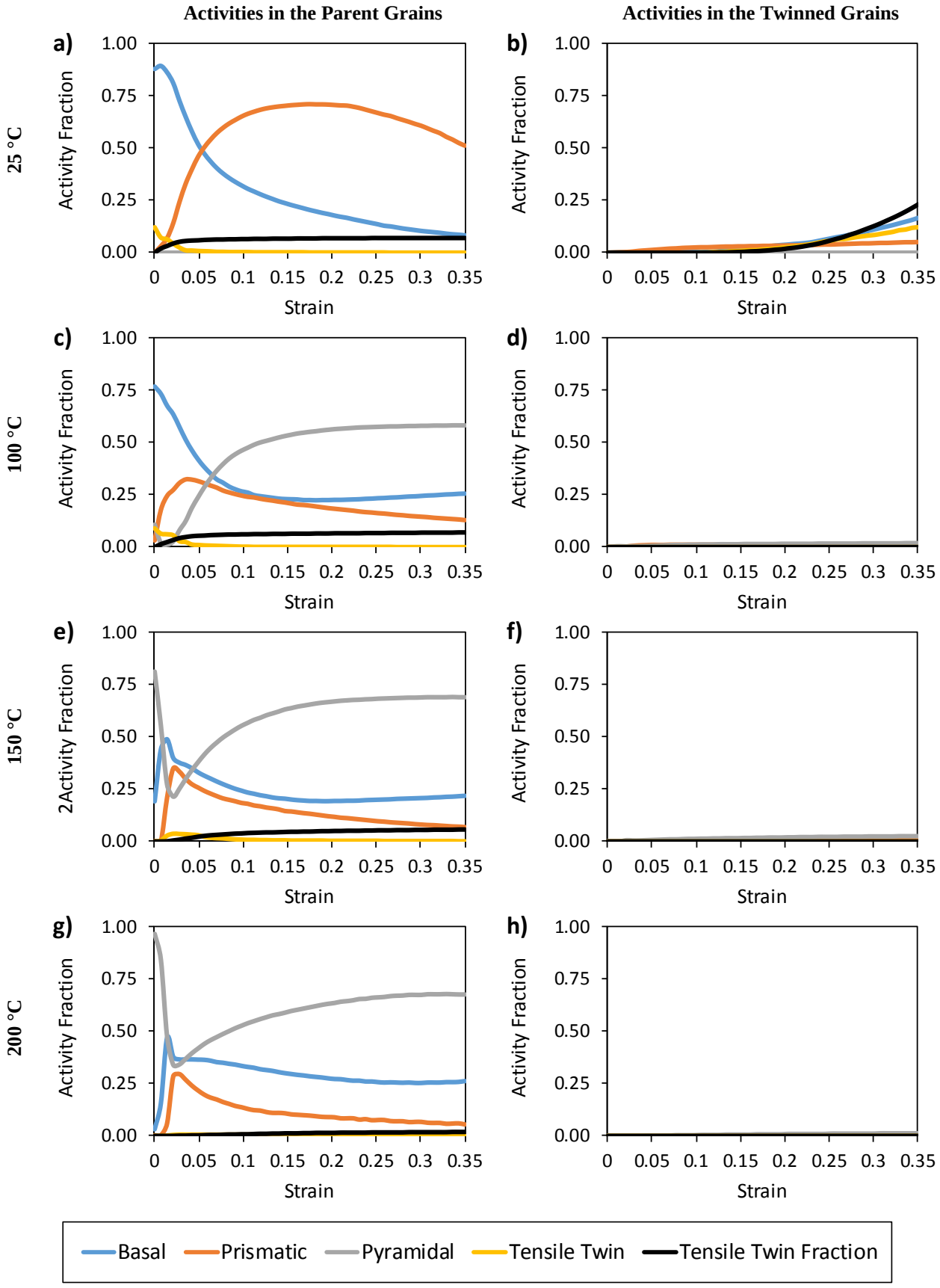

Figure 4.10 Predicted activities in the parent (a, c, e, and g) and twinned (b, d, f, and h) grains for loading in the transverse direction at: (a, b) 25 °C, (c, d) 100 °C, (e, f) 150 °C, and (g, h) 200 °C

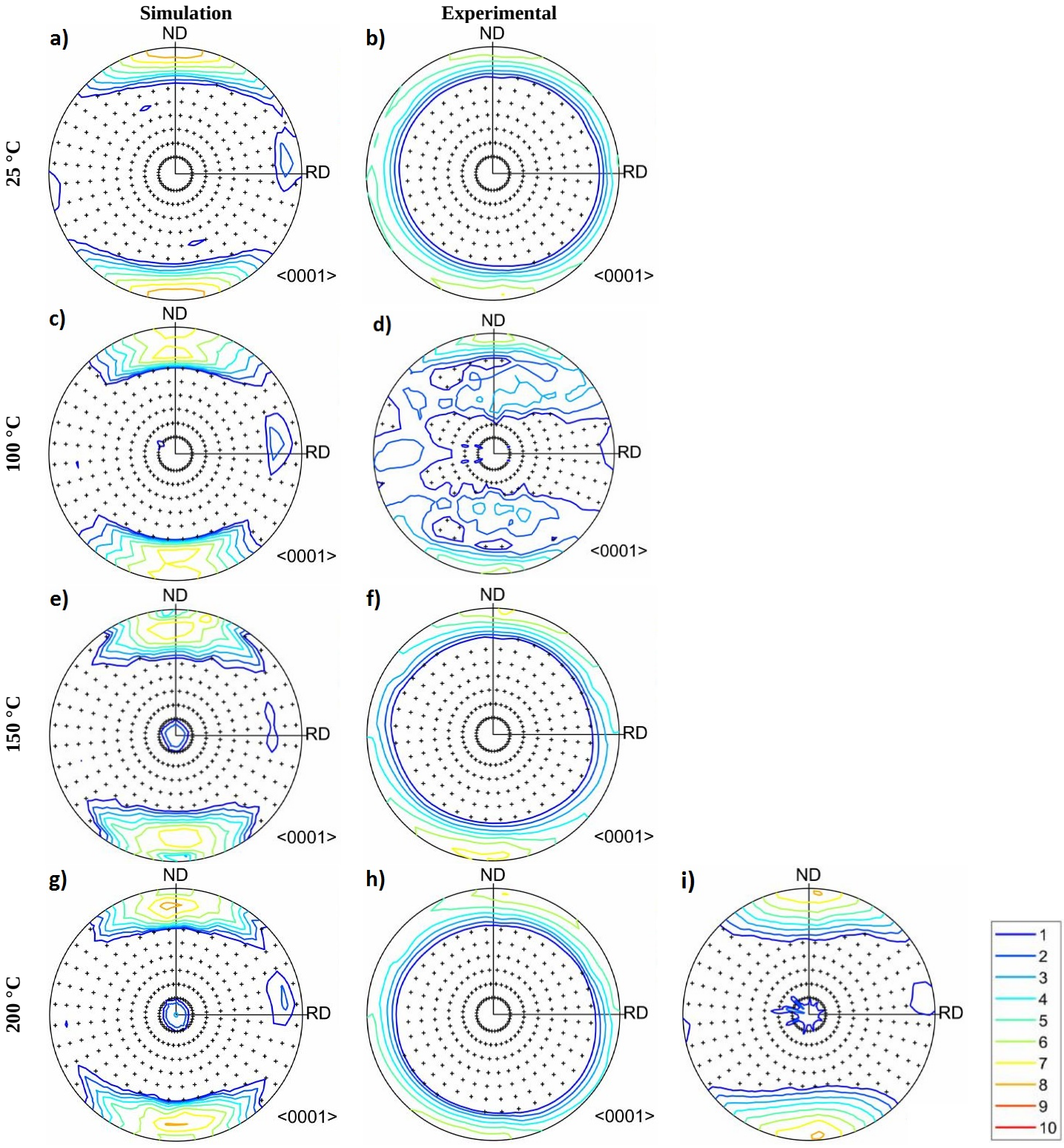

Figure 4.11 Pole figures of simulation and experimental for loading in the transverse direction. The simulation pole figures are taken at a strain of 0.14 at 25 °C, a strain of 0.315 at 100 °C, a strain of 0.315 at 150 °C, and a strain of 0.315 at 200 °C. The initial texture (i) is included for comparison.

4.3.3 45° to the Normal Direction (ND45)

It should be noted, in order to simplify the modelling process of the ND45 loading direction, the initial texture was rotated 45° counter-clockwise (see Figure 4.12), and the resulting PF after deformation was rotated 45° clockwise for the texture analysis.

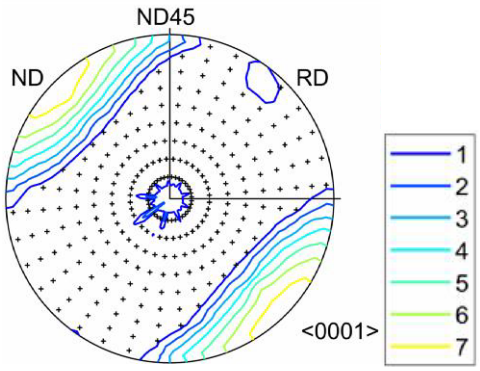

Figure 4.12 Initial (0001) pole figure for loading at 45° from the normal direction with reference to the material orientation.

At room temperature, the stress-strain curve for ND45 (Figure 4.13) exhibits a downward curvature, showing twinning activity as seen in the ND stress-strain curves (Figure 4.4). At 100 °C and above, this “S” shape curve is no longer evident, indicating that the predominant deformation mode is then slip deformation (see Figure 2.6a). Furthermore, at the temperature of 200 °C the experimental stress-strain curve shows a softening attributed to DRX (see Figure 2.11a). The work hardening curves for ND45 in Figure 4.14 reveals that there is a large twinning activity at room temperature (see Figure 2.9b), but at 100 °C and above twinning is not present anymore and the predominant deformation mechanism is slip deformation (see Figure 2.6b).

With the ND45 case the loading direction is 45° offset from the c-axis of the Mg unit cell, and there are components of the load that will be parallel to the c-axis and others perpendicular to the c-axis. The expected stress-strain curves and activities will be a

combination of those found in the ND and TD cases: basal and prismatic slip, and tensile twinning, reflected by the activities in Figure 4.15.

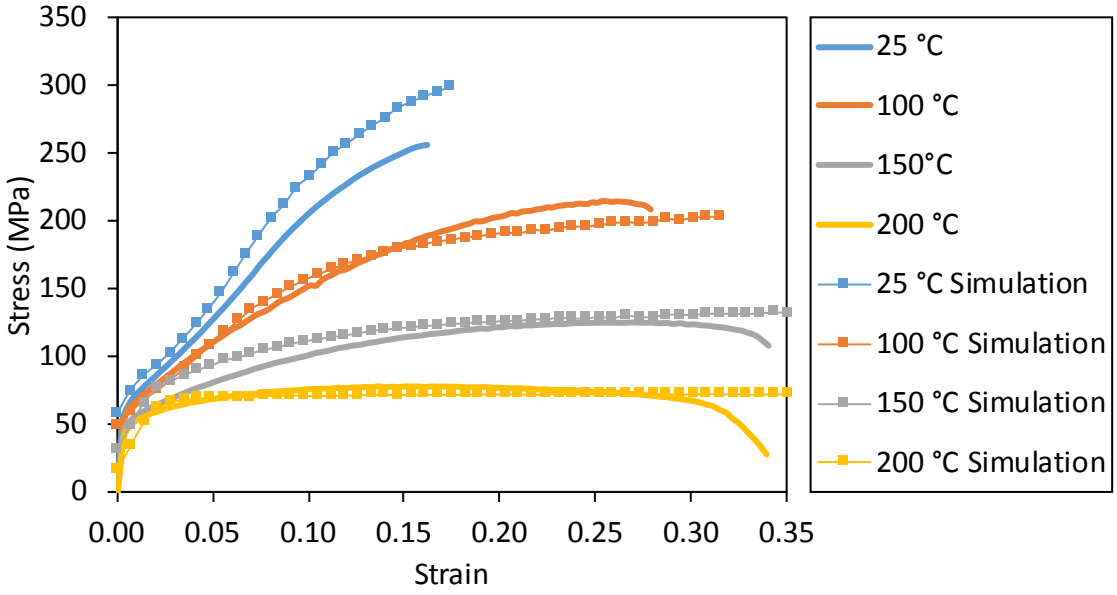

Figure 4.13 Stress-strain curves of AZ31 for loading at 45° from the normal direction at: (a) 25 °C (in blue), (b) 100 °C (in orange), (c) 150 °C (in grey), and (d) 200 °C (in yellow). The dotted lines represent the simulation results while the solid lines represent the experimental data.

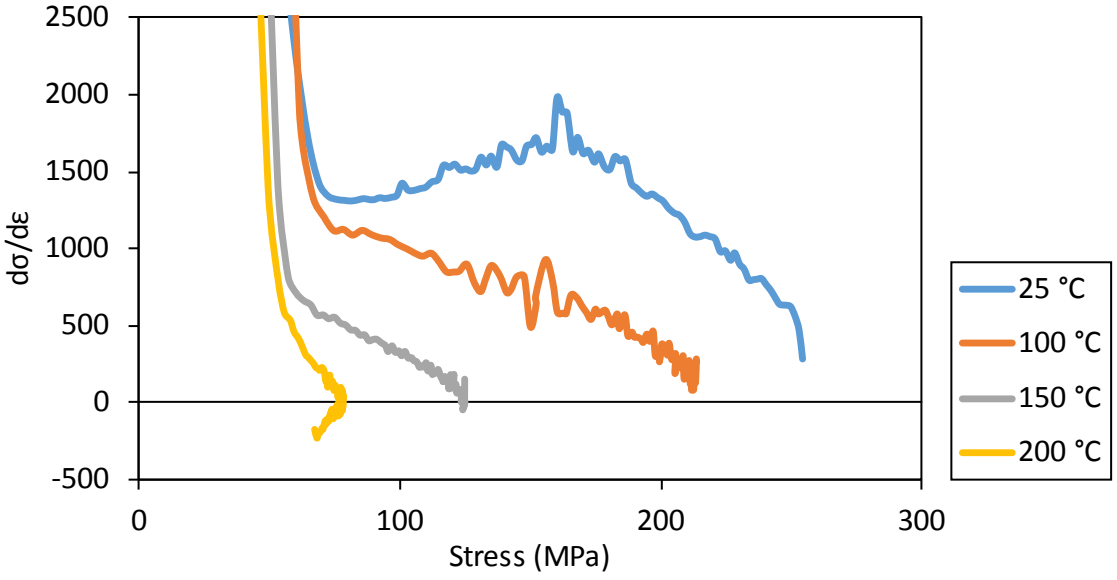

Figure 4.14 Work hardening curves of AZ31 for loading at 45° from the normal direction at: (a) 25 °C (in blue), (b) 100 °C (in orange), (c) 150 °C (in grey), and (d) 200 °C (in yellow).

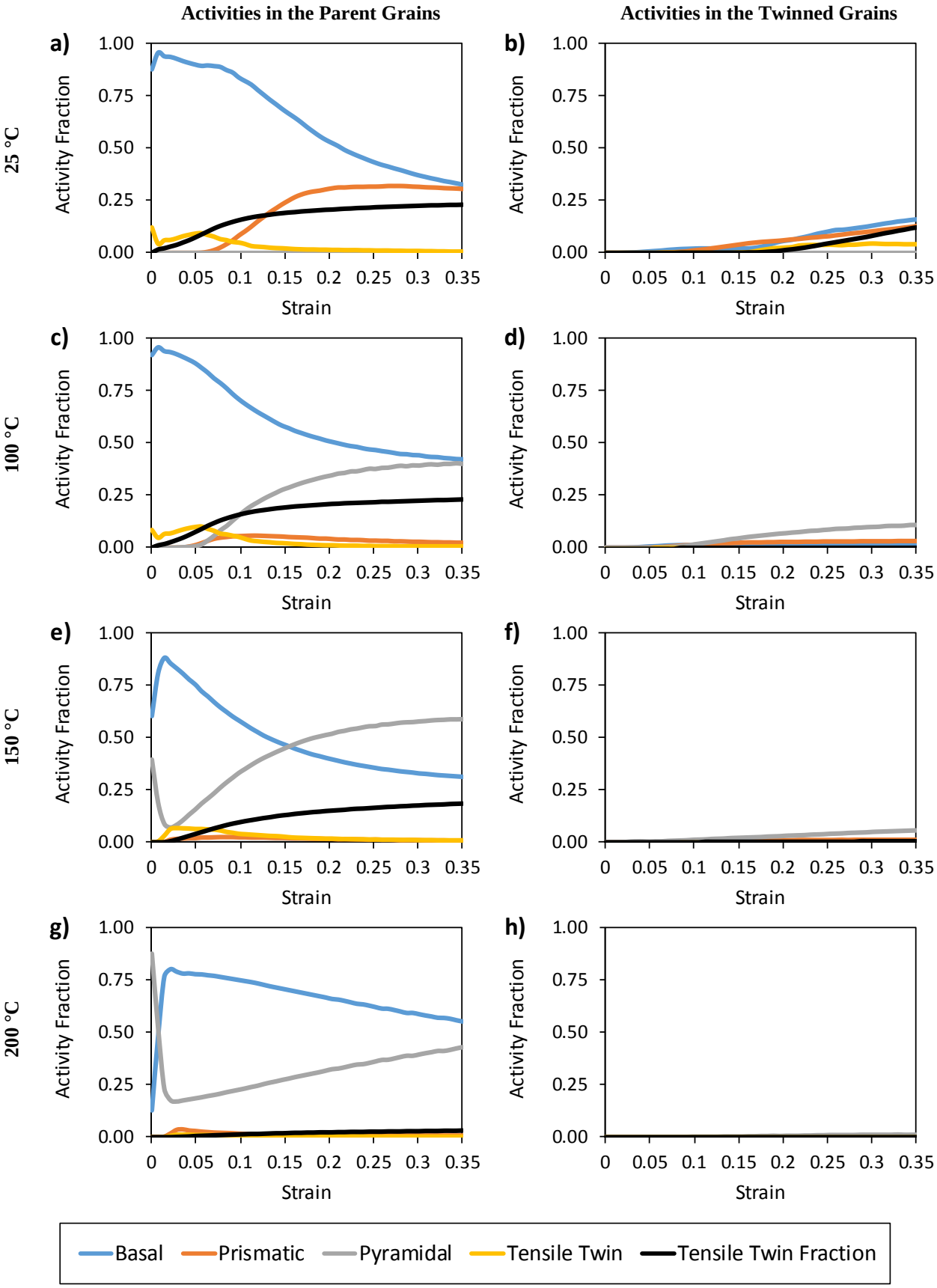

Figure 4.15 Predicted activities in the parent (a, c, e, and g) and twinned (b, d, f, and h) grains for loading at 45° from the normal direction at: (a, b) 25 °C, (c, d) 100 °C, (e, f) 150 °C, and (g, h) 200 °C

At room temperature, the two main deformation mechanisms are basal slip and tensile twinning at low strains and at higher strains, prismatic slip replaces tensile twinning. At higher temperatures, a decrease in twinning and prismatic slip activities is observed, while pyramidal slip activity increases and at 200 °C, there are no more tensile twinning and prismatic slip activities.

The twinned fractions are 22% at room temperature and 19% at 150 °C, and there is a significant drop to 3% at 200 °C due to the changes in the active deformation mode. At 100 °C, the initial deformation mechanisms are the same as at room temperature, however, at strains above 5%, pyramidal slip is active as opposed to prismatic. Similarly, within the twinned grains, basal and prismatic slip are active at room temperature, while at 100 °C the predominant deformation mode is pyramidal slip.

As with the TD case, the model predicts that deformation in the ND45 loading direction occurs predominantly through slip deformation, which results in textures (Figure 4.16) that are similar to the initial texture (Figure 4.1). The high intensity region in the centre of the PF and the two other regions indicated by the green arrows are attributed to tensile twinning. The intensity in these regions decreases at higher temperatures, which correlates with the decrease in twinning activity seen in Figure 4.15.

Furthermore, the simulation and experimental PFs show a decreasing intensity of the basal planes normal to the loading direction with increasing temperature. At room temperature, the experimental textures seem to show a higher twinning activity than those predicted by the model. However, another explanation could be that the regions analysed experimentally to measure the texture after deformation are at or near the fracture surfaces where high twinning activity is usually observed [8]. Additionally, the variability of the

experimental deformed texture, discussed in Section 4.3.2, is reinforced as the orthotropic texture is only visible at room temperature and 200 °C (see Figure 4.16b and Figure 4.16h). In the experimental PFs, the basal planes are skewed in the clockwise or counter-clockwise direction (see Figure 4.16d and Figure 4.16f, respectively), depending on the orientation from which the analysis was conducted.

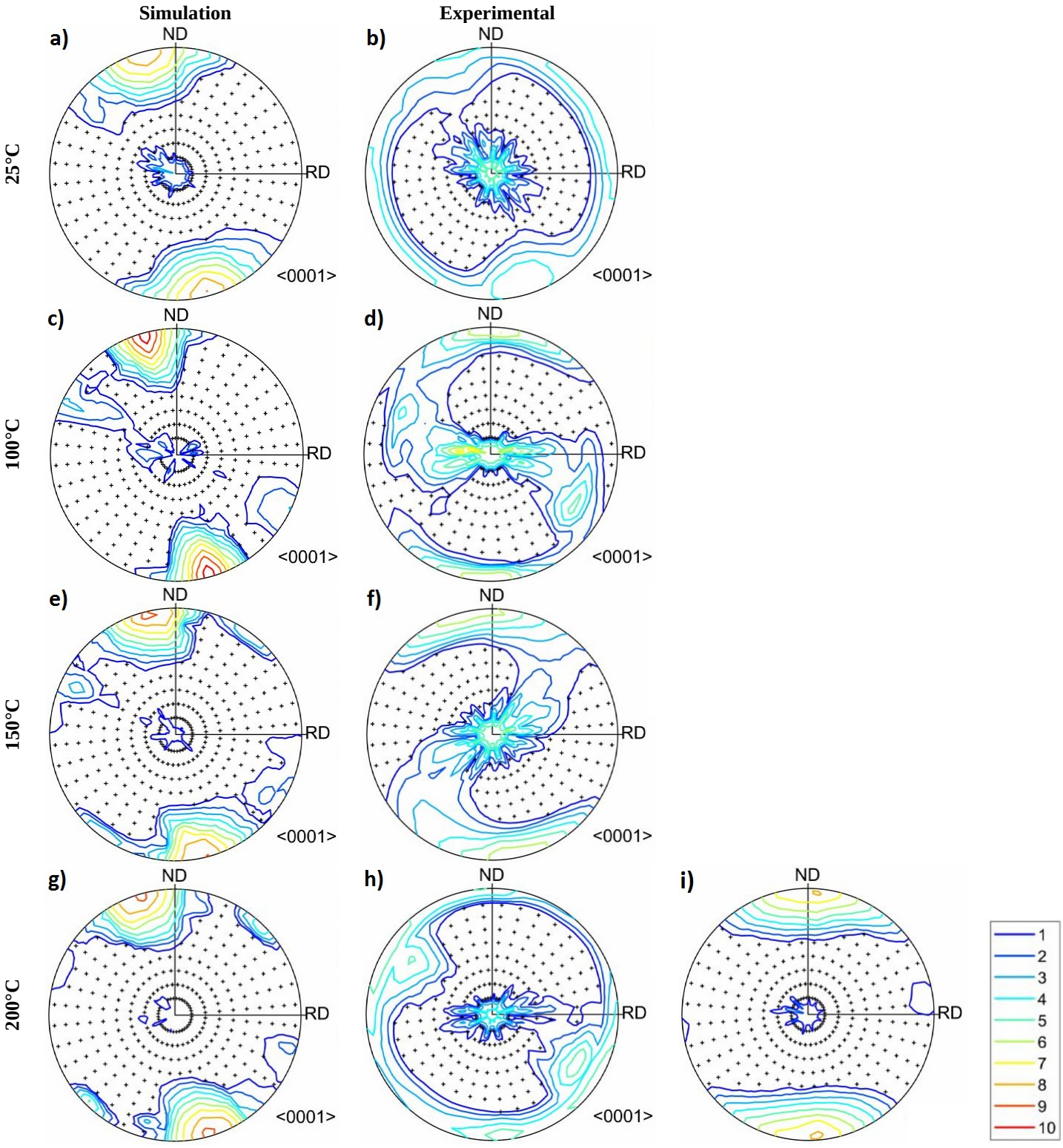

Figure 4.16 Pole figures of simulation and experimental for loading at 45° from the normal direction. The simulation pole figures are taken at a strain of 0.14 at 25 °C, a strain of 0.21 at 100 °C, a strain of 0.315 at 150 °C, and a strain of 0.315 at 200 °C. The initial texture (i) is included for comparison.

4.4 DISCUSSIONS

4.4.1 Interaction Matrix Effects

Despite the lack of research on the temperature effects on interaction matrices, the studies have shown that the interaction matrix has significant impacts on the plastic behaviour [56, 119, 133]. In this study, the interaction matrix was set to be a function of temperature such that it will approach unity at lower temperatures. A secondary study was conducted, to elucidate the effects of a temperature sensitive interaction matrix, which is compared to a constant interaction matrix. This study is able to reveal the influence the interaction matrix has on the stress-strain curves, shown in Figure 4.17, where the hollow symbol curves represent the temperature insensitive interaction matrix and the filled symbol curves represent the temperature sensitive interaction matrix. Across all temperatures and loading directions, the filled curves are in general higher than the hollow curves. This effect is consistent with the model as the temperature sensitive interaction matrix correlates with a softer hardening behaviour at elevated temperatures.

At 100 °C, in the ND case, there are minimal differences in the mechanical behaviour between the constant and variable interaction matrices. The variable model exhibits a decreased hardening behaviour at strains between 0% and 12%. At the end, both simulation models reach the same ultimate tensile stress of 200 MPa. When the temperature increases to 150 °C, there is a significant shift in the ultimate tensile stress reaches 159 MPa and 139 MPa for constant and variable interaction matrices, respectively.

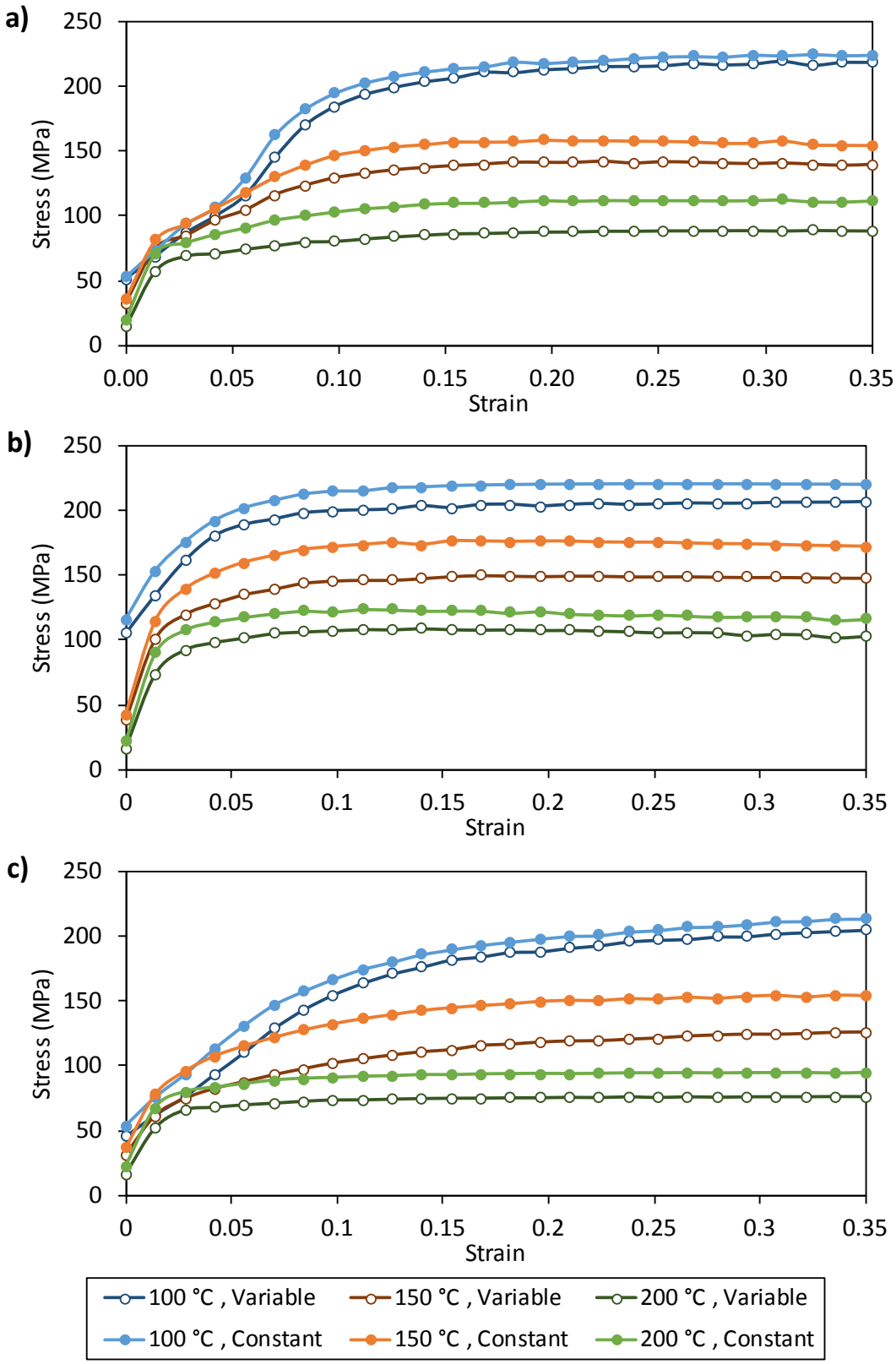

Figure 4.17 Interaction matrix comparison of stress-strain curves at the three different temperatures for loading in the: (a) normal direction, (b) transverse direction, and (c) 45° from the normal direction. The hollow symbols a temperature dependent interaction while the matrix filled symbols represent a constant interaction matrix.

When the temperature is 200 °C a similar reduction in the hardening behaviour is seen. Here the ultimate stresses are 112 MPa and 89 MPa for constant and variable interaction matrices, respectively. In the 150 °C and 200 °C cases, the hardening behaviour difference is seen across all strains. These changes in the mechanical behaviour reflects the reduced hardening behaviour when changing to the temperature sensitive model, which is more accurate in reproducing the experimentally observed behaviour. Similarly, when the temperature increases there is a corresponding decrease in the yield strength and a similar effect is seen between the temperature sensitive and constant interaction matrices.

As with the ND cases, the TD cases show a similar reduced hardening behaviour across all strains and temperatures, when the temperature sensitive interaction matrix is used. The main difference between the two models is that the hardening level is decreased in the temperature sensitive model, resulting in a 20 MPa decrease in stress for strains beyond 3%. The lower yield strengths predicted by the temperature sensitive model are also observed in this case.

Similarly, as before, the ND45 stress-strain curves show a similar reduction in the hardening behaviour and yield strengths across all strains and temperatures. The simulated stress-strain curves reveal a steady stress difference between the constant and temperature sensitive models, a difference which is temperature dependent. Furthermore, the yield strength shows a temperature sensitivity akin to the ND and TD cases as well. These effects show a decreased hardening behaviour with the temperature sensitive model, analogous with the effects seen in the ND and TD cases.

Overall, the VPSC model using a constant interaction matrix consistently overpredicts the hardening behaviour of the plastic deformation. This discrepancy can be attributed to

a higher dislocation interaction term (τ_{for}^{s}), determined through Equation (3-27) to describe the hardening behaviour [14, 57, 109, 116, 117], which is dependent on the interaction matrix and the dislocation density. The curves in Figure 4.17 demonstrate that the interactions between dislocations need to be made temperature dependent to accurately predict the hardening behaviour of Mg at different temperatures. The modified VPSC model, VPSC-T, with a temperature sensitive interaction matrix developed in this study is able to accurately predict the plastic behaviour of MgAZ31 at different temperatures.

4.4.2 Drag Stress Effects

Within the VPSC simulation the drag stress is used in the k_2/k_1 term of Equation (3-29) to describe the dislocation annihilation-generation ratio, which is used to calculate the changes in dislocation densities for each slip mode and inside each grain, as described by Equation (3-28). A greater drag stress value correlates with a larger dislocation generation, and an increase in dislocation density, which modifies the hardening behaviour. A secondary study was conducted to elucidate the temperature dependency of the drag stresses on the mechanical behaviour and the results are shown in Figure 4.18.

At 25 °C, it can be seen that there is no discernible difference in the mechanical behaviour for the various loading directions when using larger drag stress values for prismatic, pyramidal, or basal slip (Figure 4.18a, c, and e). This is due to twinning being the predominant deformation mode at this temperature, the drag stress will not produce a large effect, due to the limited slip activity. A larger deviation in the stress-strain curves can be seen in Figure 4.18c and e, in the TD and ND45 loading directions, respectively,

as the anisotropic nature of the material allows for the activation of prismatic slip in detriment to twinning [17, 19, 39, 41].

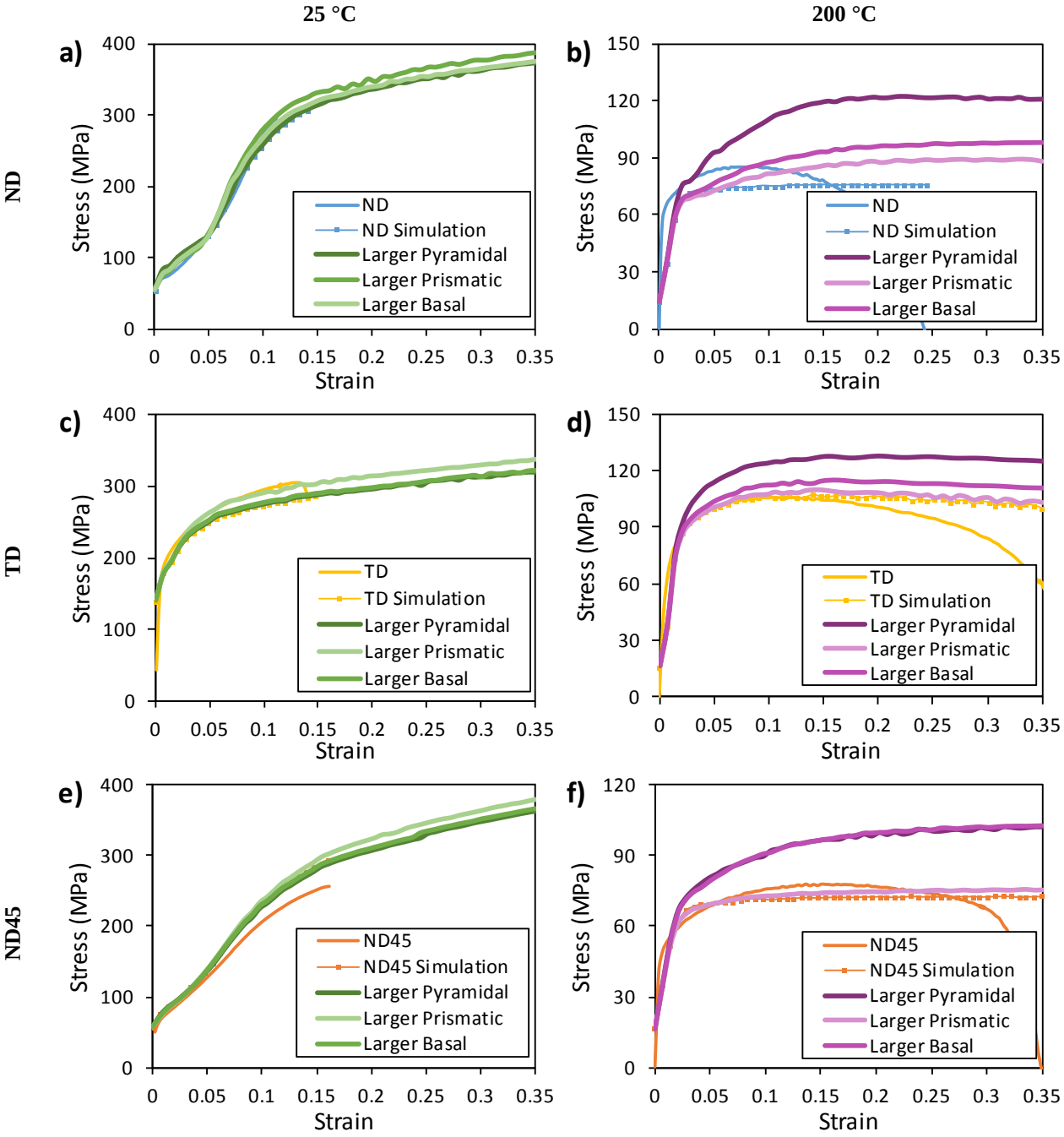

Figure 4.18 Stress-strain curves on the temperature dependency of drag stress at 25 °C (a, c, and e) and 200 °C (b, d, and f) for loading in the: (a-b) normal direction, (c-d) transverse direction, and (e-f) 45° from the normal direction

Meanwhile, at 200 °C, the use of large drag stress values elicits a greater change in the stress-strain curves than at room temperature (Figure 4.18b, d, and f). These differences

in the stress-strain curves are related to the increased slip activity, the increased drag stress here allows for a greater dislocation density to be generated. At 200 °C, the main deformation mechanisms are pyramidal and basal slip, which is reflected in a greater influence on the stress-strain curves from larger drag values for pyramidal slip and basal slip, as shown in Figure 4.18. This parametric study shows that the incorporation of temperature sensitive drag stresses for each slip mode is necessary in order to accurately predict the hardening behaviour of Mg alloys at elevated temperatures.

4.4.3 Yield Strength

An interesting feature of the stress-strain curves and work hardening curves is that the yield strength are approximately 75 MPa at all temperatures for ND (see Figure 4.4 & Figure 4.5). In the ND45 case, the yield strengths are approximately 75 MPa for 25 °C and 100 °C and reduces to 30 MPa at 150 °C and 200 °C (see Figure 4.8 and Figure 4.9). On the other hand, there is a noticeable drop in the yield strength value with increasing temperatures for TD (Figure 4.13 & Figure 4.14), where the yield strengths range from 80 MPa to 210 MPa.

The changes in the yield strength is a direct result of the changes in the CRSS value of the slip deformation modes as they are temperature sensitive, while the CRSS for twinning are temperature independent [19, 28, 29, 39, 43, 52]. This effect is exemplified in ND45 from 100 °C through to 200 °C, where there is a transition of the predominant deformation mode from tensile twinning to slip.

The VPSC-T model utilises a temperature sensitive drag stress to predict the hardening behaviour. Several studies have shown the drag stress is dependent on the deformation

temperature [29, 60, 124], while another study has shown drag stresses are equivalent to the yield strength [126]. Mg alloys are expected to experience a decrease in the yield strength with increasing deformation temperature through the activation of $\langle c + a \rangle$ pyramidal slip, a temperature sensitive deformation mechanism [28, 29, 52]. Ultimately, the drag stresses are reduced either as a direct result of increased deformation temperature or secondarily through yield strength, which decreases with increasing deformation temperatures as well. This obfuscates as to what the controlling factor is for the drag stress values, is temperature or yield strength more important? This question cannot be presently answered. Regardless of the controlling factor, Figure 4.18 shows that a reduced drag stress at elevated temperatures is necessary in order to accurately predict the Mg alloys behaviour.

4.4.4 Deformation Activities

Figure 4.19 illustrates the trends of the total deformation activities with increasing temperatures in the ND, ND45, and TD loading directions. These figures reveal several trends with increasing deformation temperature; there is a decrease in twin activity (and subsequent increasing slip activity), and pyramidal slip is preferentially activated over basal and prismatic slip. These trends are due to the temperature sensitive nature of the CRSS values for slip, while the CRSS values for twinning are constant at different temperatures [19, 39]. Additionally, it has been shown that, the CRSS values for pyramidal slip are highly sensitive to temperature [28, 29, 52], which is reflected in the results in Figure 4.19.

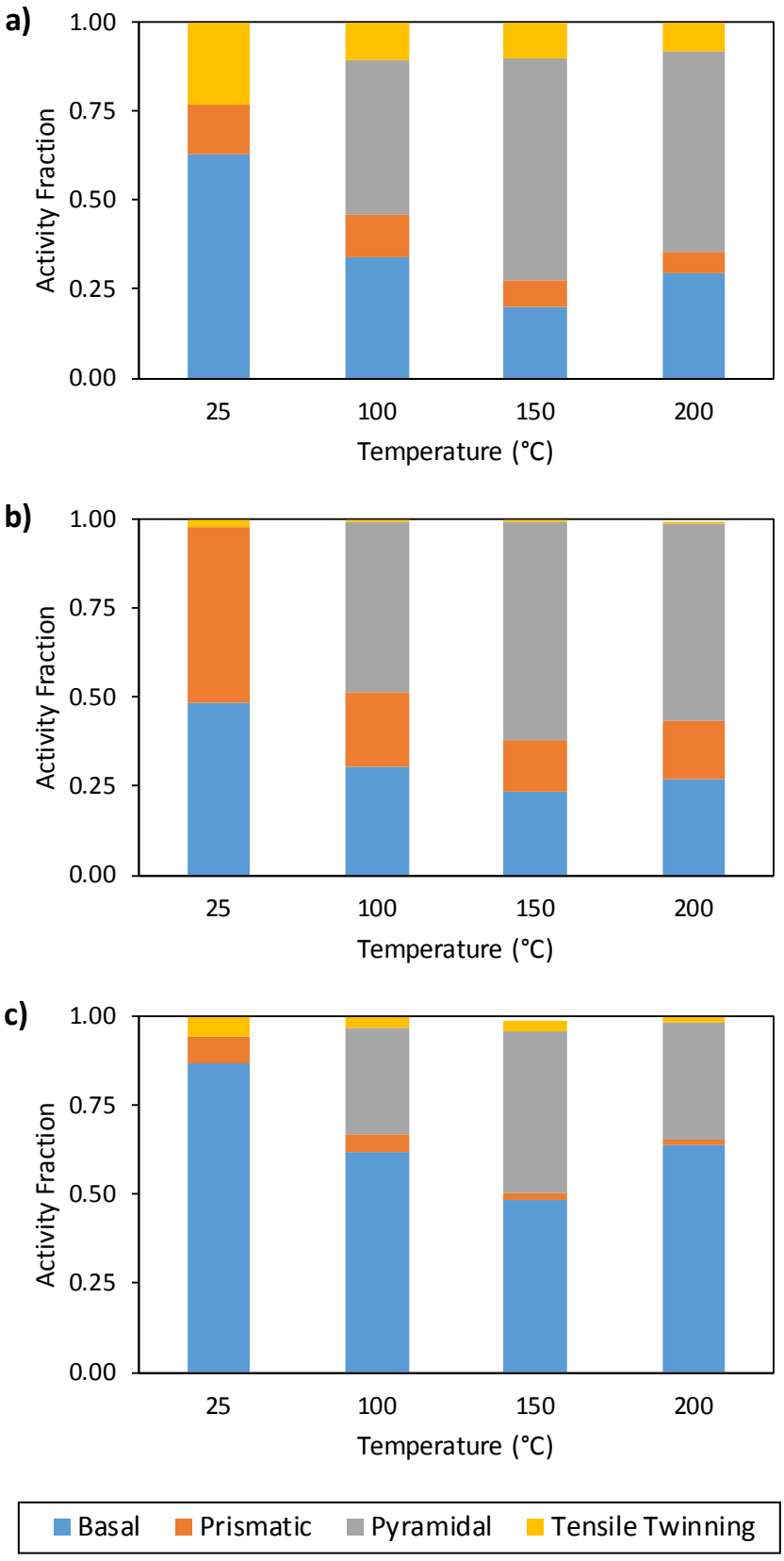

Figure 4.19 Comparison of the total deformation activities at different temperatures in the: (a) normal direction, (b) transverse direction, and (c) 45° from the normal direction.

At room temperature, the two important loading directions due to Mg's anisotropy, are parallel and perpendicular to the c-axis. When the loading direction is perpendicular to the c-axis, prismatic slip is preferentially activated [17, 19, 39, 41], while also having basal slip as another main deformation mode due to its low CRSS value. In this study, for the TD case, the loading direction is perpendicular to the c-axis, which results in the expected deformation modes prismatic and basal slip to be activated. On the other hand when the loading direction is parallel to the c-axis the predominant deformation mode is tensile twinning [46, 51], which is confirmed by the ND case. Furthermore, the twinned grains' c-axis is perpendicular to the loading direction as the tensile twinning rotates the grain by 86° [7, 16-18, 20, 22, 28, 31, 39, 43, 51, 55, 56], which results in the activation of the prismatic slip in the twin grains due to the twinned grains c-axis becomes perpendicular to the loading direction. Finally, when the loading direction is 45° offset to the c-axis, in the ND45 case, there are a combination of ND and TD deformation activities resulting in the activation of tensile twinning and prismatic slip in conjunction with basal slip [17].

At higher temperatures (100 °C and 150 °C), pyramidal slip becomes increasingly easier to activate allowing for the transition of the predominant deformation mode from twinning to slip, as shown in previous studies [19, 29, 31, 39, 46]. At deformation temperatures of 150 °C there is a notable similarity in all loading directions, wherein the predominant deformation mode is slip (Figure 4.4, Figure 4.8, and Figure 4.13). In the ND45 case, the loading direction is not favourable for the activation of tensile twinning and prismatic slip, this results in a larger level of basal slip activity compared to the other loading directions. Similarly, at 200 °C, the predominant deformation mode is slip for all

loading directions, with basal and pyramidal slip being the two main contributors to the total deformation, as expected from previous studies [28, 29, 43, 52].

At 200 °C the experimental stress-strain curves show a softening effect (Figure 4.4, Figure 4.8, and Figure 4.13) before fracture that can be attributed to DRX. At this higher temperature, Mg alloys are known to deform through DRX, albeit not as the main deformation mechanism [19, 43, 61, 62]. DRX is often identified through the use of the work hardening curves (see Figure 2.11b), which is shown first as the curve crossing the x-axis and then a reverse hardening effect creating a “hook” shape seen in Figure 4.5, Figure 4.9, and Figure 4.14 [85, 92]. The simulation data does not predict this softening behaviour as no DRX scheme is implemented in the VPSC-T model. The next chapters will present a recently developed VPSC model, VPSC-DRX, for modelling the recrystallisation effects on the plastic flow behaviour to possibly improve these predictions [134].

There is a notable feature in Figure 4.19, where there is a significant drop in pyramidal slip activity and an increase in the basal slip from 150 °C to 200 °C in all loading directions. Pyramidal slip is highly sensitive to temperature and is easier to activate at 200 °C [39, 43, 60, 61], which results in larger fractions of pyramidal slip activity at lower strains, shown in Figure 4.6, Figure 4.10, and Figure 4.15. However, due to the differing strain hardening rates exhibited between basal and pyramidal slip, with pyramidal slip having a higher strain hardening rate compared to basal slip [57, 135], this results in an overall drop in pyramidal slip.

4.4.5 Texture Analysis

The simulated textures found for the ND and TD cases are in close agreement with the current literature across all tested temperatures. On the other hand, with the ND45 cases it is difficult to verify the model as loading directions 45° to the c-axis are rarely investigated. As explained previously, our predicted PFs show less twinning activity than the experimental PFs, which could be an artefact of the experimental measurements.

As stated before, tensile twinning reorients the unit cell 86° about the $\langle 11\bar{2}0 \rangle$ axis [7, 16-18, 20, 22, 28, 31, 39, 43, 51, 55], which is easily noticeable on the (0001) PFs. Since the initial texture contains grains with their c-axis are parallel to the ND any twinning activity will be seen by a decrease of the initial high intensities at the north and souths of the initial (0001) PF [8, 14, 15, 19, 29, 41, 55, 136].

In the ND case, with increasing deformation temperature, the activity of tensile twinning has been shown to decrease [8], which can be seen on the deformed PFs with a smaller amount of twinning reorientation in Figure 4.7 [39, 42]. Similarly, the PFs for all the TD cases are also in close agreement with the current literature. When the loading is applied perpendicular to the c-axis, there is limited tensile twinning activity occurring; the material deforms predominantly through basal and prismatic slip [17, 19, 28, 31, 39, 41, 43, 52]. This limited tensile twinning activity occurring during deformation, consistent with the minimal changes in the texture after deformation [14-17, 19, 29, 31, 39, 41, 42, 55]. The little amount of deformation via tensile twinning is seen by the creation of two regions in the PFs indicated by two black arrows in Figure 4.11.

The deformation activities in the ND45 cases are a combination of the activities observed in the ND and TD cases, which is reflected in the deformed PFs in Figure 4.16. Tensile twinning activity is seen at room temperature on the (0001) PF by the presence of high intensity at the centre of the PF in Figure 4.16. As temperature increases, twinning activity decreases, which is observed by a lower intensity at the centre of the PF at 200 °C [8]. Additionally, at 200 °C, the green arrows in Figure 4.16 highlight region in the PF that correspond to grains that have twinned [8].

4.4.5.1 Texture evolution in the Normal Direction

The evolution of the deformed (0001) PFs after the material is loaded in the ND at 25 °C, 100 °C, 150 °C and 200 °C can be found in Figure 4.20, Figure 4.21, Figure 4.22, and Figure 4.23, respectively, for different strains and plotted using different material axis orientations. There are three different material axis orientations used to analyse the texture evolution in the ND directions: ND-RD-PF, with the RD in the centre of the PF, ND-TD-PF, with the TD in the centre of the PF, and ND-ND-PF, with the ND in the centre of the PF.

At room temperature the evolution of the activity of the tensile twinning is captured through the increasing presence of the twinned grains that have their c-axis rotated away by 86° from the ND, similarly to the PF in Figure 4.7. This is easily observed using the ND-RD-PFs and ND-TD-PFs. At low strains ($\varepsilon = 3\%$), there is already a significant level of twinning as indicated by the intensity peak highlighted by the red circle in Figure 4.20. With increasing strains, the twinned fraction increases, and this generates a band structure across the centre of the ND-RD-PFs and ND-TD-PFs. The ND-TD-PFs shows this band is comprised of multiple distinct peaks [7, 17, 22, 31, 39], highlighted by the three black

arrows in Figure 4.20. The intensity of these indicated regions increases at higher levels of strain. Furthermore, the ND-ND-PFs show that the band in the PF created by the twinned grains generates an orthotropic structure at higher levels of strain ($\varepsilon \geq 6\%$).

When the temperature increases to 100 °C and 150 °C, the predominant deformation mechanism at lower strains ($\varepsilon \leq 10\%$) is similar to the one observed at room temperature (Figure 4.6), namely twinning. A similar behaviour at lower strains can be seen in the texture evolution at 100 °C and 150 °C in Figure 4.21 and Figure 4.22, respectively. At a strain, $\varepsilon = 3\%$, Figure 4.21 and Figure 4.22 have the same red circle highlighting the intensity peak of the twinned grains seen in Figure 4.20, and with increasing strain the same banded structure in the ND-RD-PFs and ND-TD-PFs is generated. The banded structures in the 100 °C and 150 °C ND-TD-PFs show the same three peaks as at room temperature with a similar evolution resulting in a similar intensity peak at the final strain. Lastly, the ND-ND-PFs at 100 °C and 150 °C show the same room temperature twinned grain orthotropic structure at higher levels of strains ($\varepsilon \geq 6\%$).

At the deformation temperature of 200 °C, there is an expected drop in the tensile twinning activity, which was observed in Figure 4.6. The ND-RD-PFs in Figure 4.23 reflects this behaviour, as the region in the PF corresponding to the twinned grains has a lower intensity than observed at the other temperatures. The twinning peaks highlighted by the red circles in Figure 4.20 and Figure 4.23 have approximately the same intensity, occurring at $\varepsilon = 3\%$ and $\varepsilon = 16\%$ for room temperature and 200 °C. The reduction in twinning is reinforced by the fact that the three peaks across the middle of the ND-TD-PF, have a drastically lower intensity [7, 8, 39]. The effects of the reduced twinning deformation are reinforced by the absence of the orthotropic structure in the

ND-ND-PFs. The increased slip activity is reflected in all the PFs in Figure 4.23 by a majority of the grains' c-axis be aligned with the ND, causing concentrated intensities at the north and south poles of the PFs.

A unique feature of pyramidal slip, known as "basal split", causes the basal planes to separate into two halves as seen in ND-ND-PFs at $\varepsilon = 16\%$, and indicated by the green arrows in Figure 4.27 [11, 15, 19, 21, 42, 132, 137]. This effect is not seen at any of the other temperatures, which could be due to the fact that there is not a sufficient level of pyramidal slip activity at lower temperatures to activate this phenomenon.

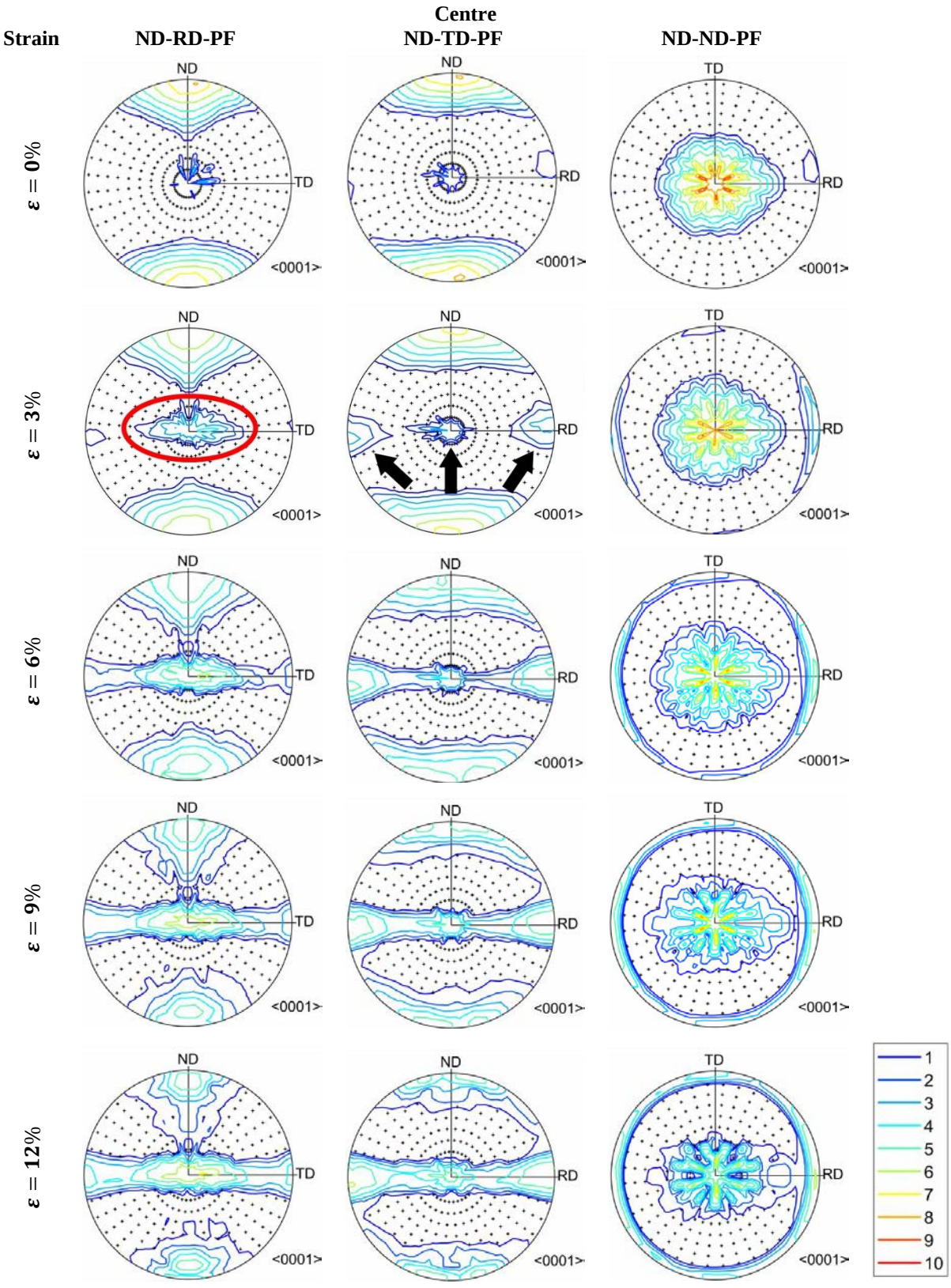

Figure 4.20 (0001) Pole figure evolution of AZ31 for loading in the normal direction at room temperature. The red circle and black arrows highlight regions of twinned grains.

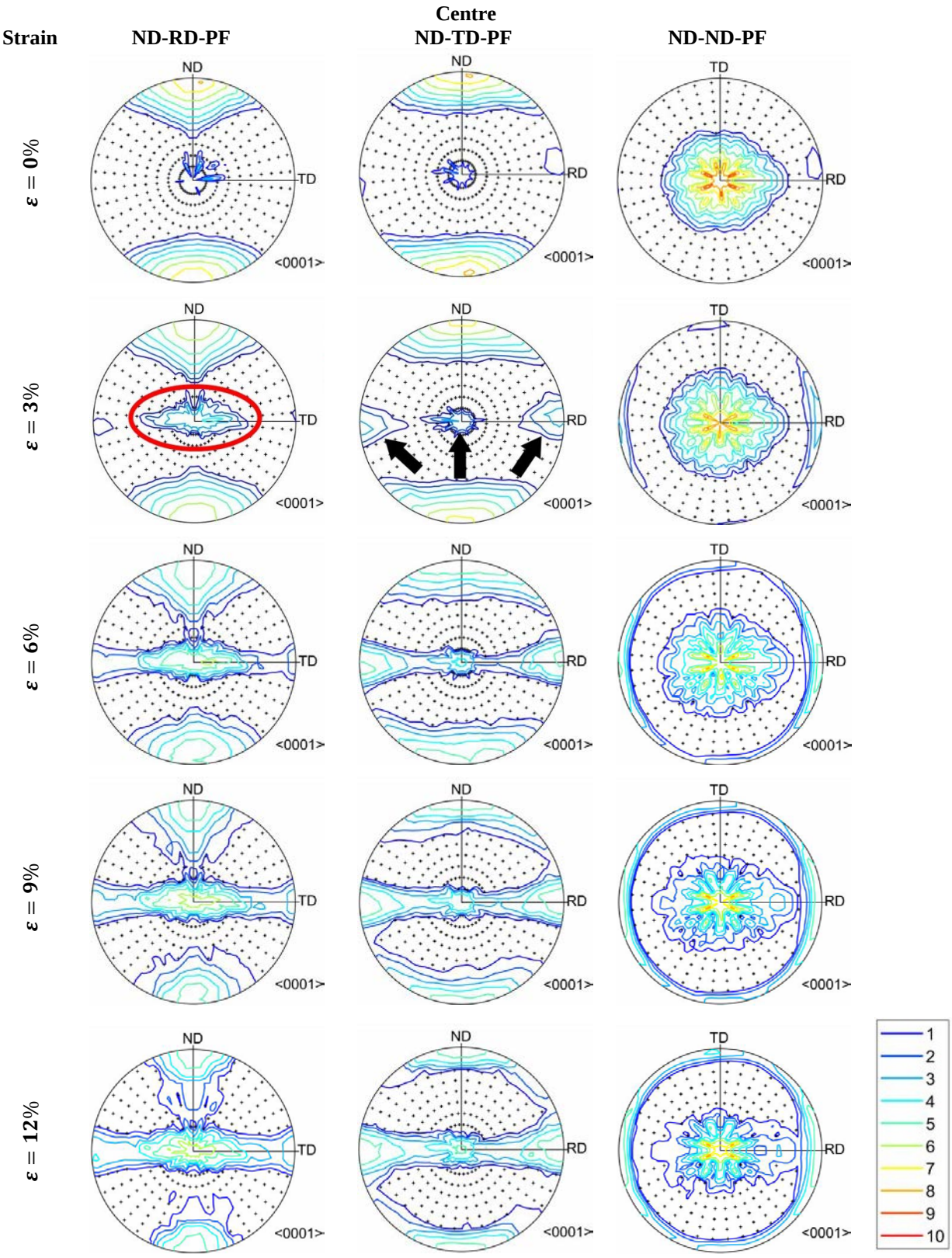

Figure 4.21 (0001) Pole figure evolution of AZ31 for loading in the normal direction at 100 °C. The red circle and black arrows highlight regions of twinned grains.

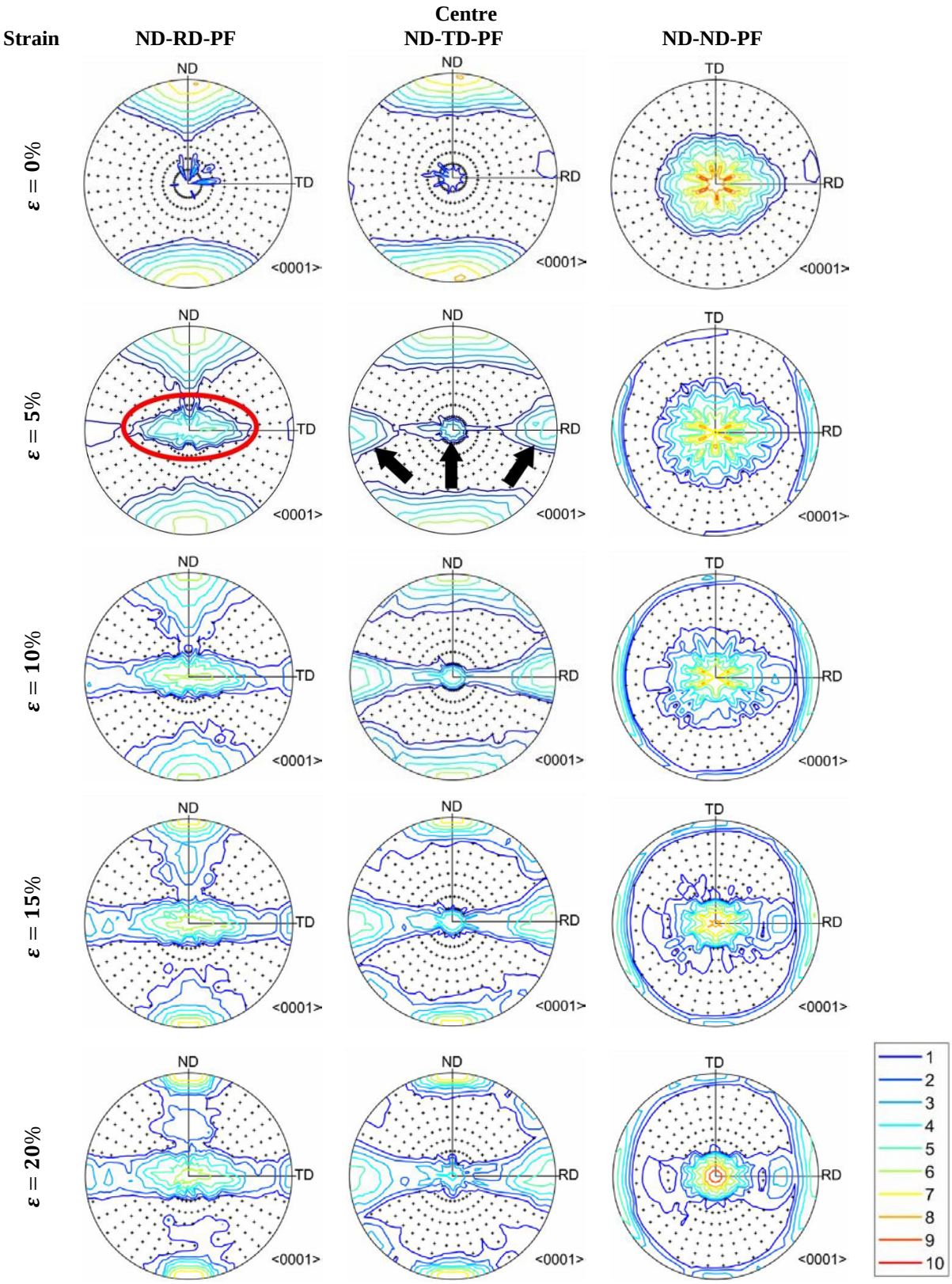

Figure 4.22 (0001) Pole figure evolution of AZ31 for loading in the normal direction at 150 °C. The red circle and black arrows highlight regions of twinned grains.

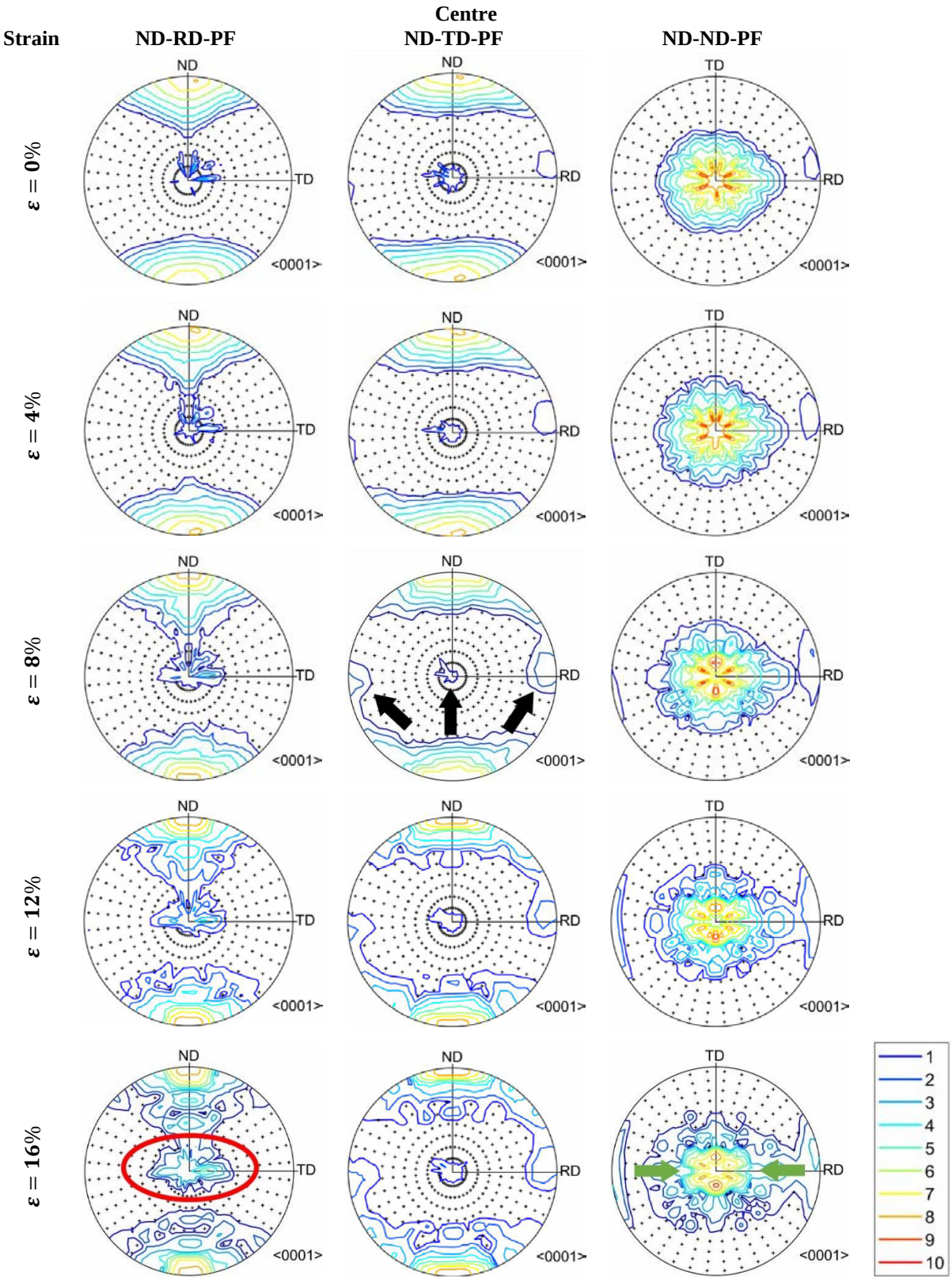

Figure 4.23 (0001) Pole figure evolution of AZ31 for loading in the normal direction at 200 °C. The red circle and black arrows highlight regions of twinned grains. The green arrows highlight the indented regions.

4.4.5.2 Texture evolution in the Transverse Direction

As a result of the anisotropic behaviour of Mg alloys, when the loading direction is in the TD direction the predominant deformation mechanism shifts from tensile twinning to prismatic slip (Figure 4.10). The evolution of the deformed (0001) and $(10\bar{1}0)$ PFs loaded in the TD at 25 °C, 100 °C, 150 °C and 200 °C can be found in Figure 4.24, Figure 4.25, Figure 4.26, and Figure 4.27, respectively, for different strains and plotted using different materials axis orientations. There are three different material axis orientations used to analyse the texture evolution in the TD direction: TD-TD-PF, with the TD in the centre of the (0001) PF, TD-ND-PF-1, with the ND in the centre of the (0001) PF, and TD-ND-PF-2, with the ND in the centre of the $(10\bar{1}0)$ PF.

Despite the deformation mechanism shift, at room temperature tensile twinning still occurs, due to the high CRSS values of prismatic slip [18, 28, 31, 56]. Tensile twinning creates the two high intensity regions in the (0001) ND-PFs indicated by the black arrows [8, 16, 17, 19, 31, 39, 41, 42], akin to the three peaks observed in the PFs obtained when loading direction is applied in the ND. These regions begin to emerge at a strain $\varepsilon = 3\%$, corresponding to the low level of twinning observed in Figure 4.10. Even with the significant level of slip activity, there is still a small level of tensile twinning activity at 100 °C and 150 °C at low levels of strain ($\varepsilon = 8\%$) [28, 31].Twinning, however, is not observed at all 200 °C [28], which correlates with the predicted deformation activities shown in Figure 4.10.

The predominant deformation mode, prismatic slip, is easily identified in the $(10\bar{1}0)$ ND-PFs in Figure 4.24 as six distinct peaks are present and arranged in a hexagonal formation [14, 15, 19, 29, 41, 55]. These are highlighted by the red arrows in Figure 4.24,

Figure 4.25, Figure 4.26, and Figure 4.27. For all the temperatures, these six peaks begin to form at a strain of $\varepsilon = 6\%$ and become increasingly defined as more prismatic activity occurs at higher strains (Figure 4.11) [14, 15, 19, 29, 41, 42]. At room temperatures, the prismatic activity results in a $(10\bar{1}0)$ PF with higher intensity peaks when compared to the PFs at elevated temperatures. This is due to the reduced level of prismatic activity at elevated temperatures as a consequence of the higher levels of pyramidal slip at these temperatures [19, 28, 29, 31, 39, 43, 46, 52].

Similarly to ND, the basal split due to pyramidal slip activity is also present in TD, as indicated by the green arrows in Figure 4.25, Figure 4.26, and Figure 4.27 [15, 19, 21, 42, 137]. At 150 °C and 200 °C, the basal split is clearly defined with two indents at opposite poles along the RD direction in the basal textures, highlighted by the green arrows in Figure 4.26 and Figure 4.27. However, at 100 °C the basal split produces four indents as opposed to the two formed at higher temperatures, shown by the green arrows in Figure 4.25. This effect is caused by the lack of pyramidal activity to completely produce the total split of the basal textures [138], reflected by the activities shown in Figure 4.10.

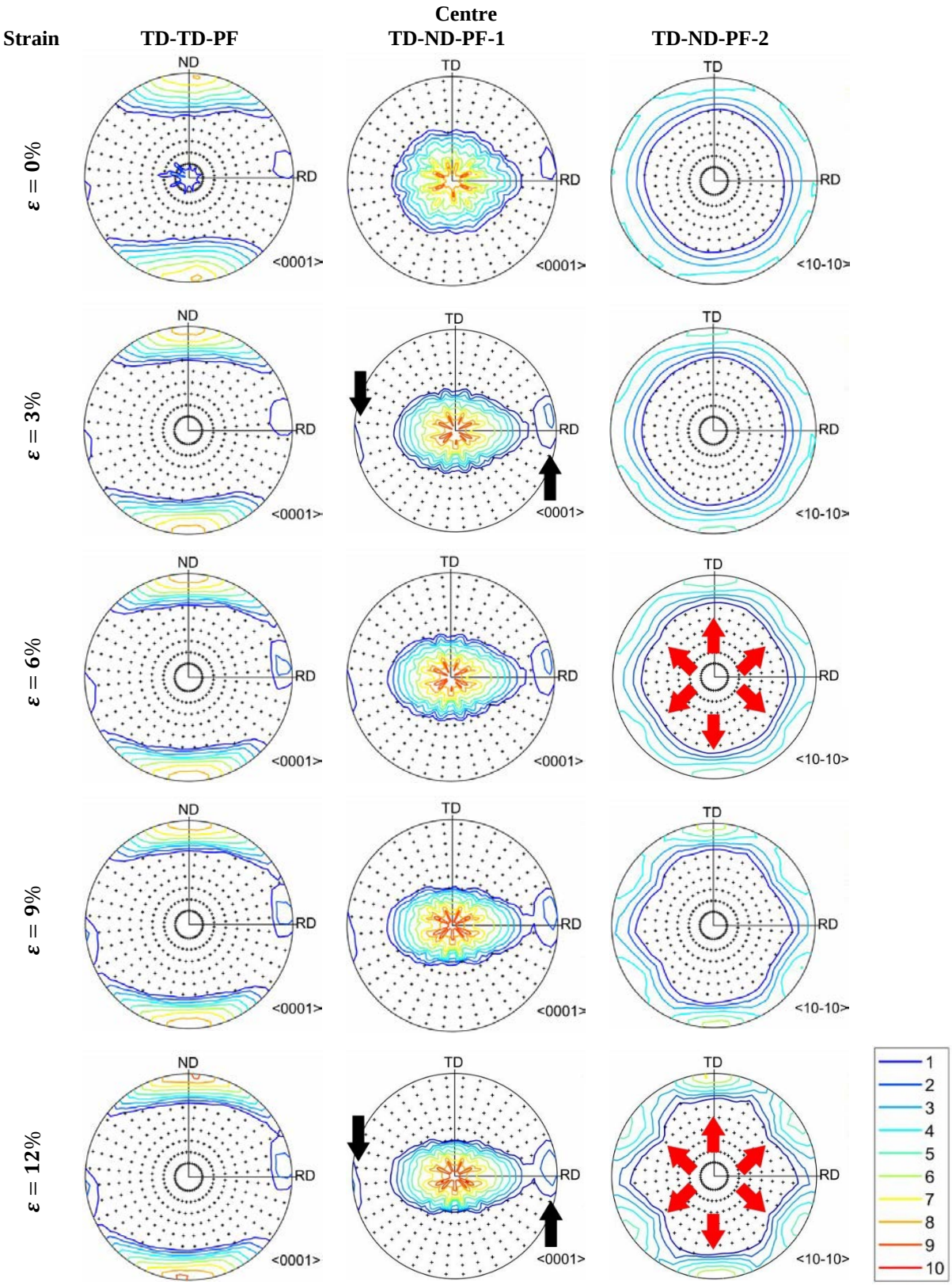

Figure 4.24 (0001) and (10$\bar{1}$0) Pole figure evolutions of AZ31 for loading in the transverse direction at room temperature. The black arrows highlight regions of twinned grains. The red arrows highlight the hexagonal created by the intensity peaks.

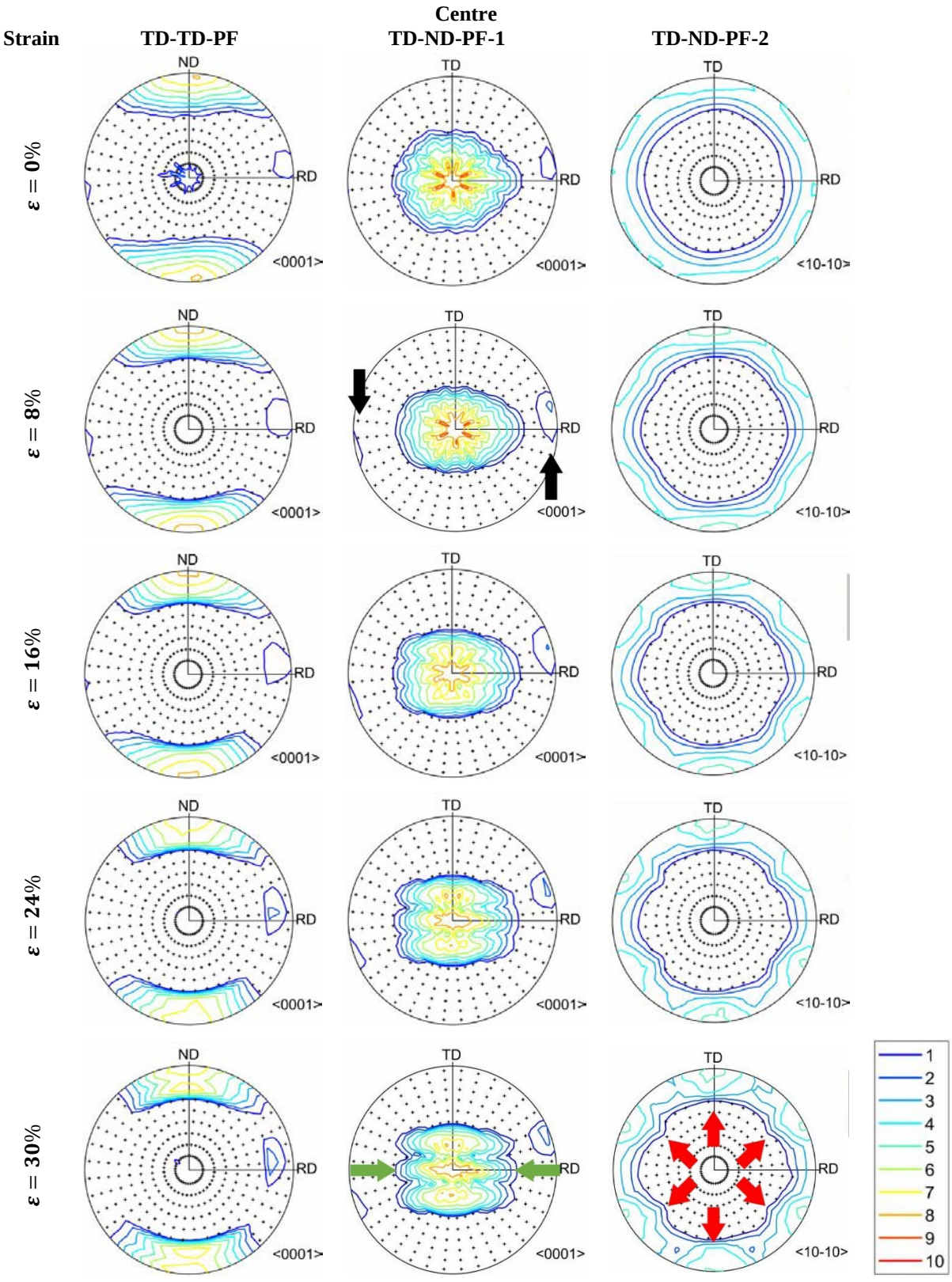

Figure 4.25 (0001) and (10$\bar{1}$0) Pole figure evolutions of AZ31 for loading in the transverse direction at 100 °C. The black arrows highlight regions of twinned grains. The green arrows highlight the indented regions. The red arrows highlight the hexagonal created by the intensity peaks.

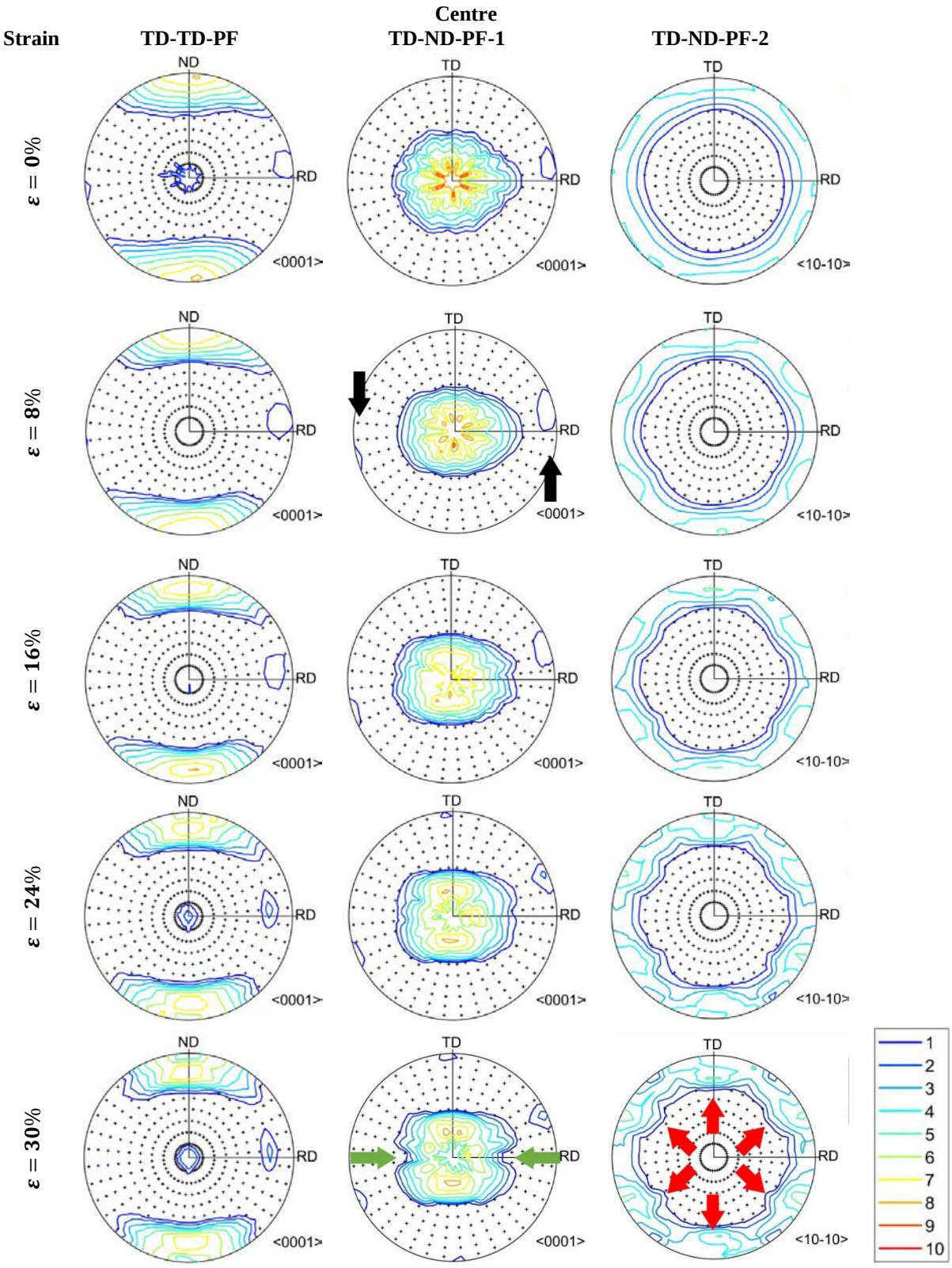

Figure 4.26 (0001) and (10$\bar{1}$0) Pole figure evolutions of AZ31 for loading in the transverse direction at 150 °C. The black arrows highlight regions of twinned grains. The green arrows highlight the indented regions. The red arrows highlight the hexagonal created by the intensity peaks.

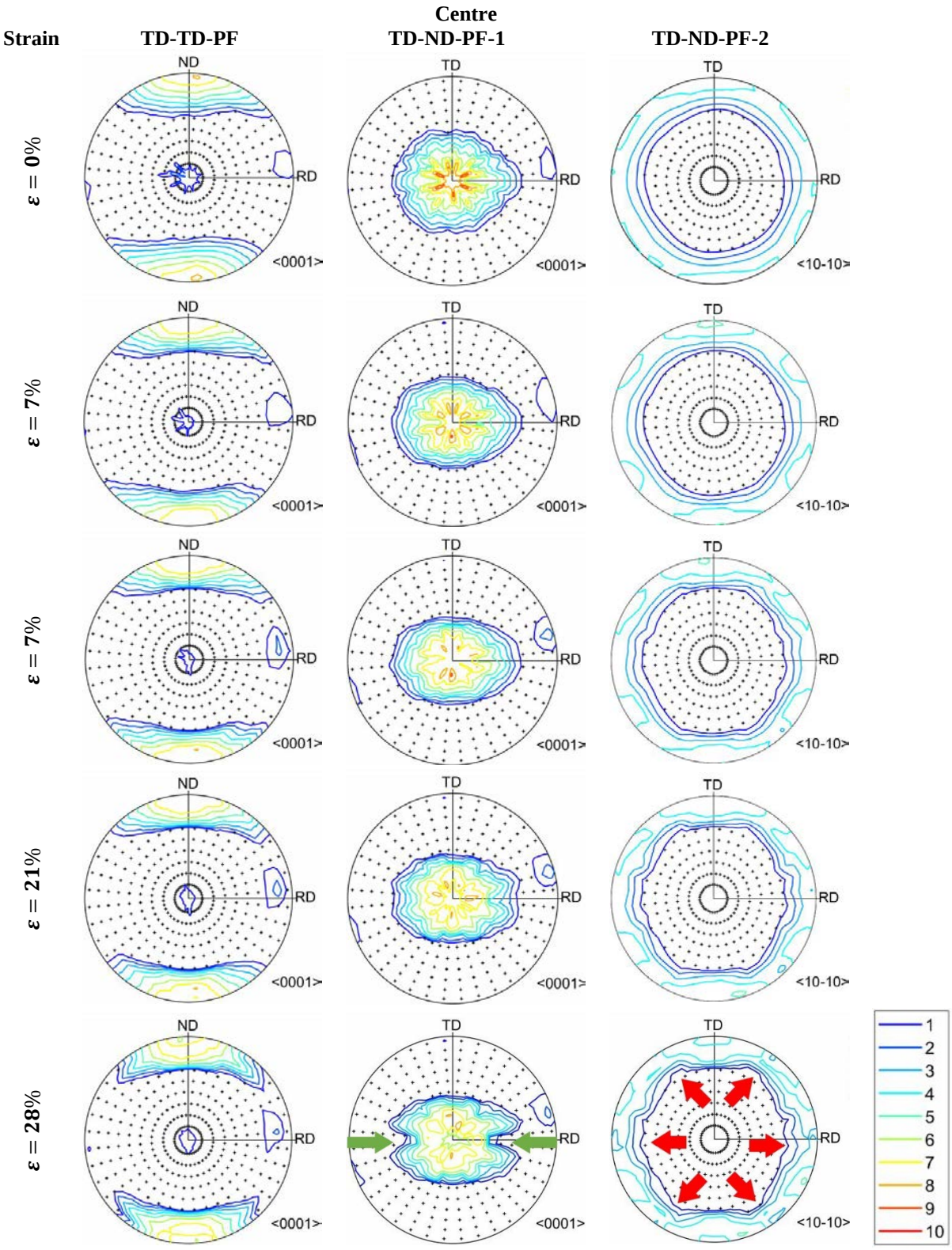

Figure 4.27 (0001) and (10$\bar{1}$0) Pole figure evolutions of AZ31 for loading in the transverse direction at 200 °C. The black arrows highlight regions of twinned grains. The green arrows highlight the indented regions. The red arrows highlight the hexagonal created by the intensity peaks.

4.4.5.3 Texture evolution 45° from the Normal Direction

The deformation mechanisms in the ND45 direction are a combination of the those found in the ND and TD (Figure 4.15), which is reflected by the deformed PFs (Figure 4.16). The evolution of the deformed PFs loaded in the ND45 direction at 25 °C, 100 °C, 150 °C and 200 °C can be found in Figure 4.28, Figure 4.29, Figure 4.30,and Figure 4.31, respectively, for different strains and plotted using different material axis orientations. There are two different material axis orientations used to analyse the texture evolution in the ND45 direction: ND45 -TD-PF, with the TD in the centre of the PF, ND45-ND-PF, with the ND in the centre of the PF.

At room temperature, the evolution of tensile twinning activity is seen in Figure 4.28 where three twinned grain regions once again appear in the PFs, they are highlighted by the black arrows in the TD-PFs. Two of the three twinned grain regions are actually masked by parts of the parent grains (initial crystallographic orientations) at low strains ($\varepsilon = 6\%$). As strain increases they, however, become more defined as expected from literature [8]. This is also seen at elevated temperatures with decreasing intensity as temperature increases as shown by the black arrows in Figure 4.29, Figure 4.30 and Figure 4.31, which is a result from the reducing twinning activity (see Figure 4.15). At 200 °C, the predicted PFs show that there is only a small amount of twinning reorientation occurring even at higher strains ($\varepsilon = 28\%$), as expected from literature [52, 139].

Slip activities are observable through the increased concentration of the basal planes in the centre of the PFs as highlighted by the purple arrow in the ND45-ND-PFs (see Figure 4.28), indicating basal and prismatic slip [139]. Notably, in Figure 4.28 with increasing strains, there is a noticeable decrease in the eastern region of the basal texture,

which is a result of tensile twinning. These grains have their c-axis are parallel with or slightly offset from the loading direction, allowing for the preferential activation of tensile twinning, as discussed previously. At elevated temperatures, 150 ℃ and 200 ℃, the basal split due to pyramidal slip activation is difficult to observed in Figure 4.30 and Figure 4.31.

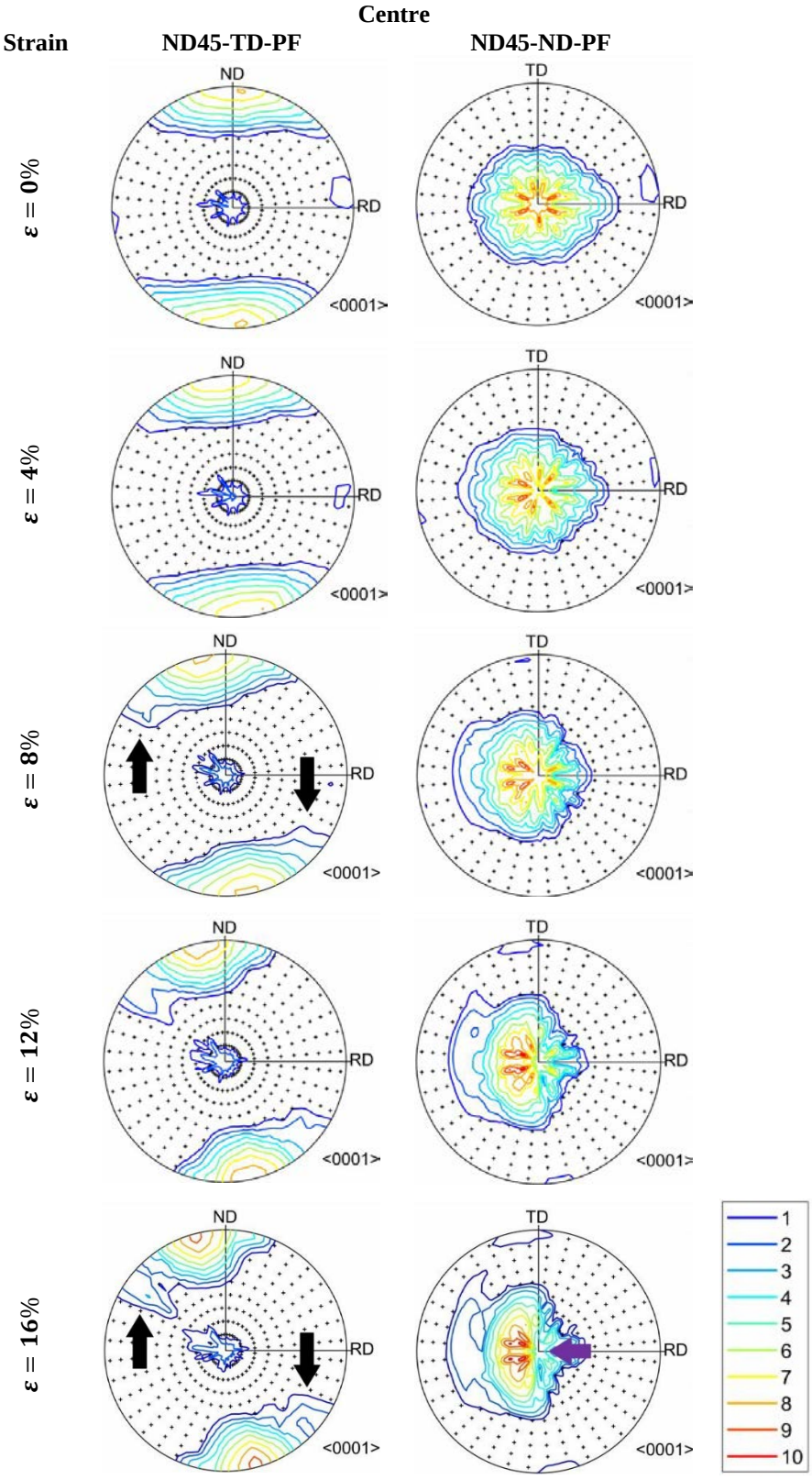

Figure 4.28 (0001) Pole figure evolution of AZ31 for loading at 45° from the normal direction at room temperature. The black arrows highlight regions of twinned grains. The purple arrow highlights the concentrated region of untwinned grains.

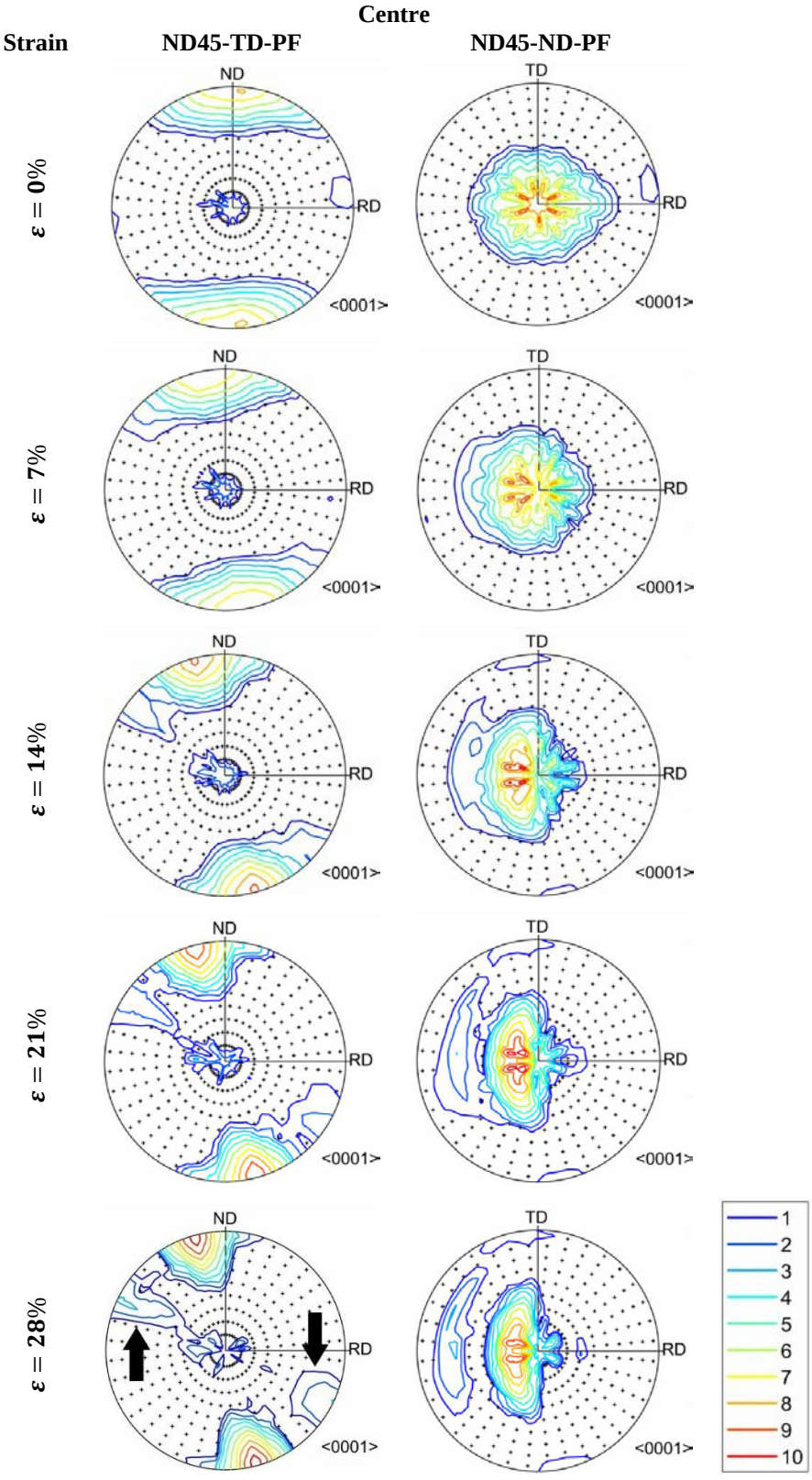

Figure 4.29 (0001) Pole figure evolution of AZ31 for loading at 45° from the normal direction at 100 °C. The black arrows highlight regions of twinned grains.

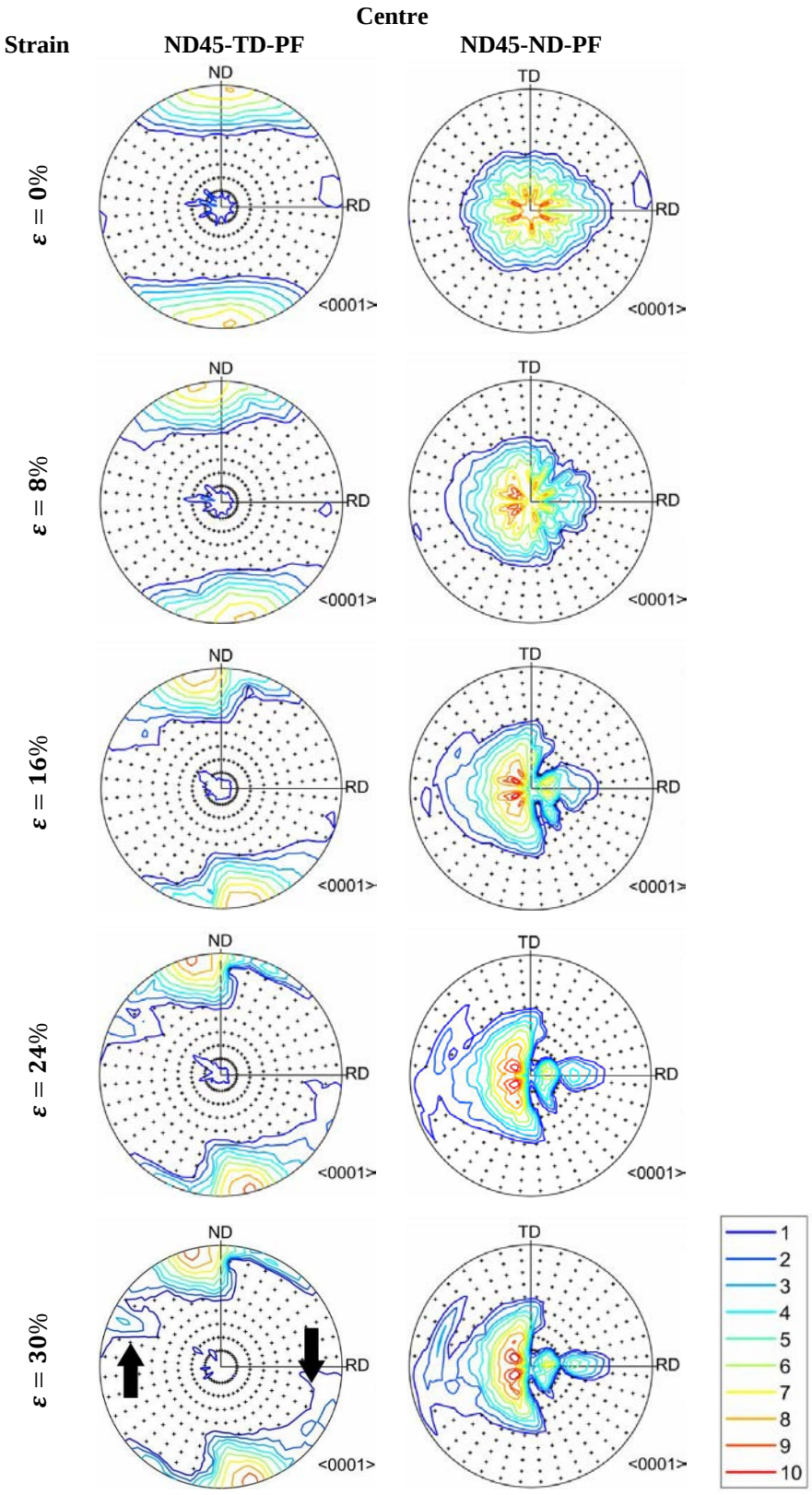

Figure 4.30 (0001) Pole figure evolution of AZ31 for loading at 45° from the normal direction at 150 °C. The black arrows highlight regions of twinned grains.

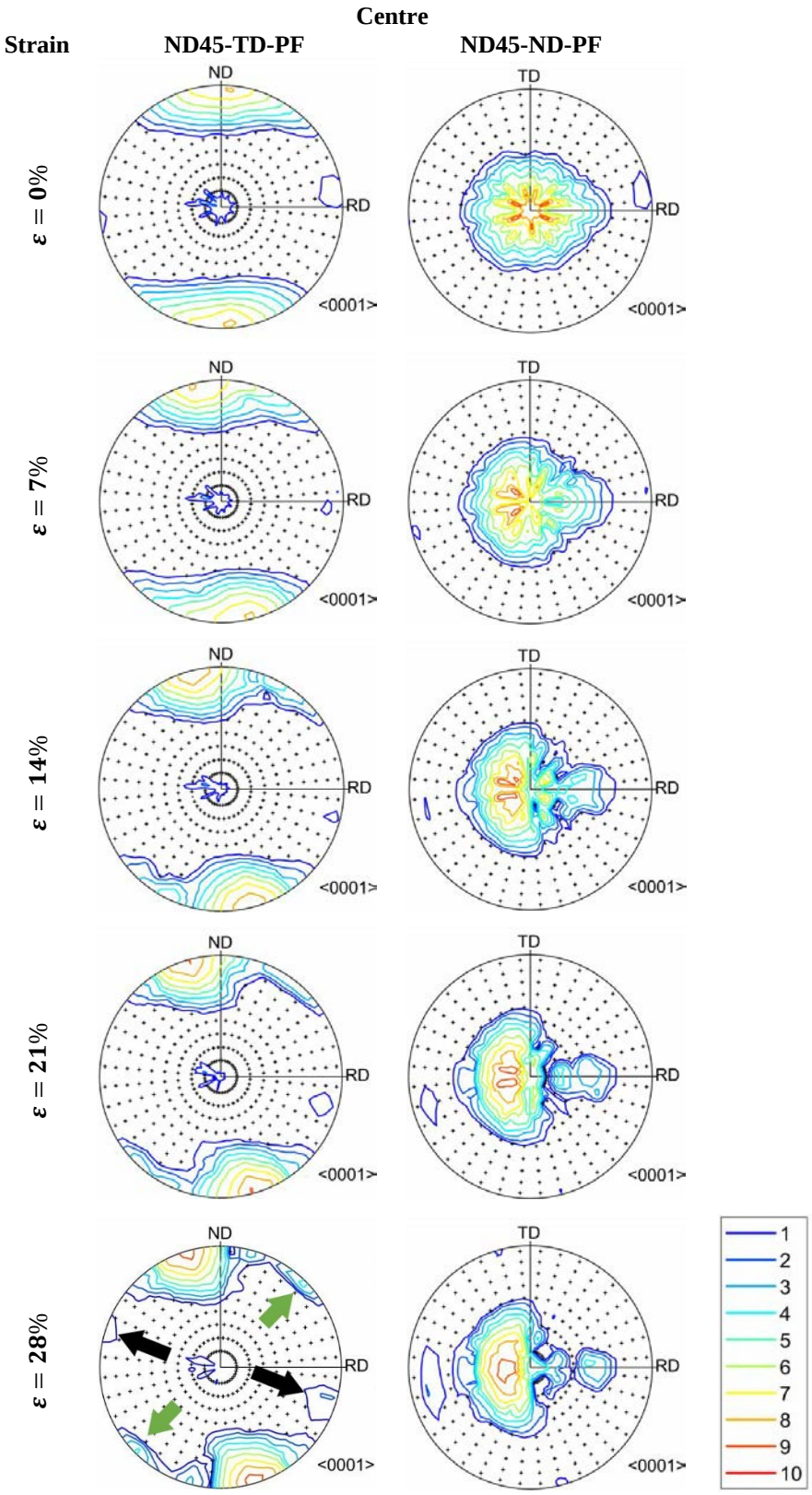

Figure 4.31 (0001) Pole figure evolution of AZ31 for loading at 45° from the normal direction at 200 °C. The black arrows highlight regions of twinned grains. The green arrows highlight the regions of untwinned grains.

4.4.6 Increased Twinning

It is hypothesised that the experimental PFs (Figure 4.7, Figure 4.11, and Figure 4.15) were measured close to or at the fracture surface in Section 4.3. This could explain the higher level of twinning due to stress concentration at the fracture surface [8]. However, the simulation PFs (Figure 4.7, Figure 4.11, and Figure 4.16) show that the model predicts a lower level of twinning than that of the experimental PFs. A secondary simulation study was conducted to determine what would happen if more twinning was taking pace during deformation. These new simulations were realised by using a modified set of hardening parameters to allow for an increased tensile twinning propensity.

4.4.6.1 Normal Direction

The PFs predicted with an increased tensile twinning activity for loading carried out in the ND are found in Figure 4.32. Despite the increased tensile twinning activity, the amount of twinning occurring in the material does not match the experimental data. The intensity of the centred peak does not reach the same value in the predicted PFs than in the experimental PFs. From 25 °C to 150 °C, the twin-enhanced PFs show a similar texture as previously predicted. However, at 200 °C, the new PFs are in better agreement with the experimental PFs. Additionally, the new PFs show a decrease of the high intensities at the north and souths of the initial PFs, such that it is comparable to the levels seen in the experimental PFs.

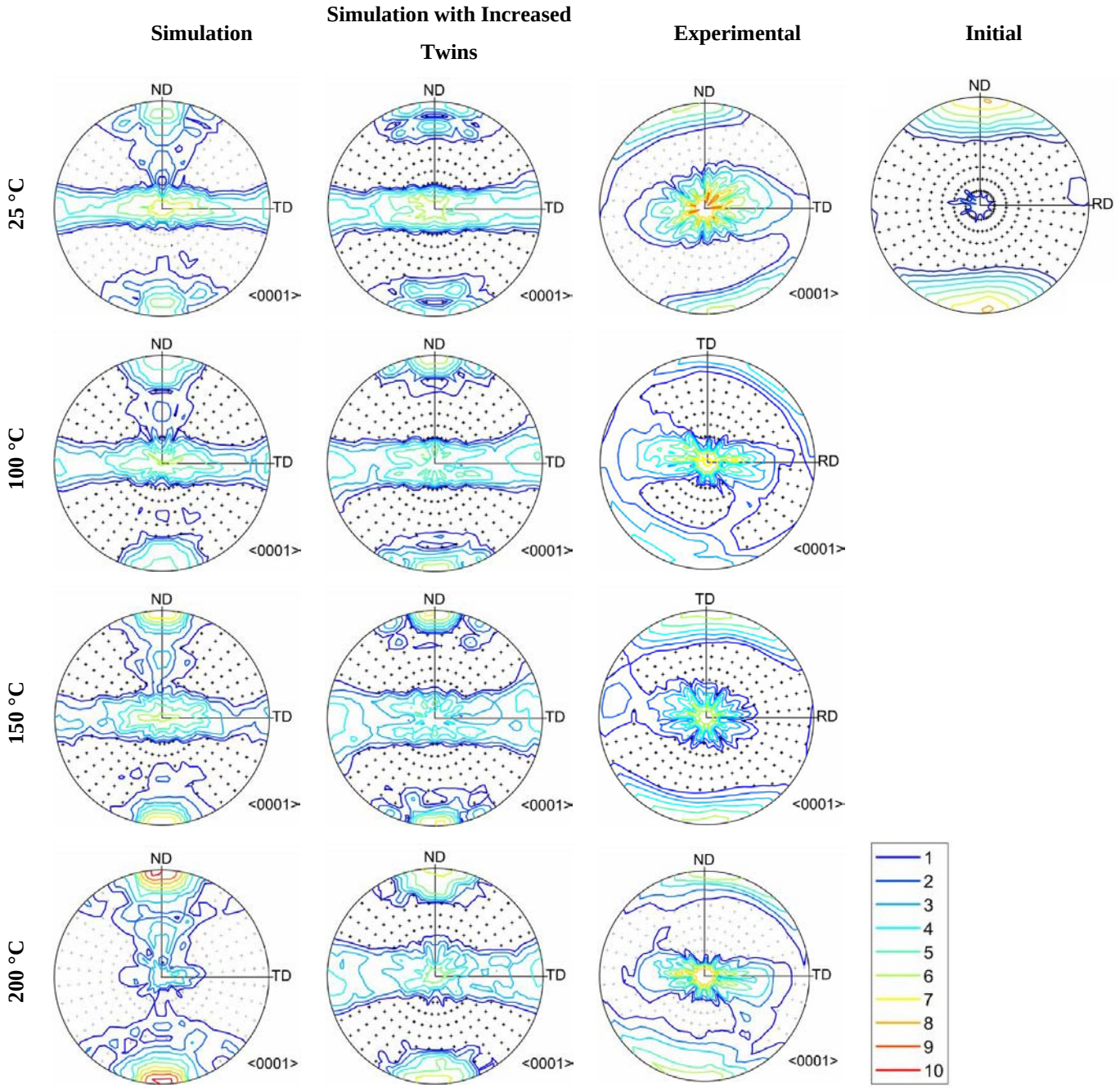

Figure 4.32 Tensile twin enhanced deformed (0001) pole figures of AZ31 for loading in the normal direction at different temperatures. The original simulation, experimental, and initial pole figures are included for comparison.

4.4.6.2 Transverse Direction

The PFs predicted with increased tensile twinning activity for loading carried out in the TD are found in Figure 4.33. While the complete orthotropic texture of the experimental PFs is not found in the twin enhanced PFs, there is a stronger orthotropic effect found

than previously. This reinforces the hypothesis that the measurement of the experimental PFs are conducted close to or at the fracture surfaces. Studies have shown that the fracture mechanism for loads applied perpendicularly to the c-axis is through twinning [19, 140, 141], where the twin boundary act as a fracture initiation site [28, 141]. In the 100 °C case, the twin enhanced PF show a near complete orthotropic texture, which is not present in the corresponding experimental PF. This also reinforces the previous hypothesis, that the measurements of the experimental PF at 100 °C was done away from the fracture surface, contrarily to the specimens deformed at the other temperatures.

4.4.6.3 45° to the Normal Direction (ND45)

The PFs predicted with an increased tensile twinning activity when the load was applied in the ND45 are found in Figure 4.34. The twin enhanced PFs' regions of twinned grains with their c-axis normal to the ND show similar intensity levels than observed experimentally across all temperatures. A similar texture was created by the increased twinning activity for the 100 °C and 150 °C cases, with the creation of the "S" shape of the texture seen in the experimental PFs. However, at room temperature and 200 °C, the orthotropic texture shown in the experimental PFs is not present in the twin enhanced PFs.

In each of the loading directions, the twin enhanced PFs show a better agreement in general with the experimental PFs, than the originally predicted PFs. This effect is repeated across all the deformation temperatures tested, from 25 °C to 200 °C, and thus, confirms the hypothesis in Section 4.3.

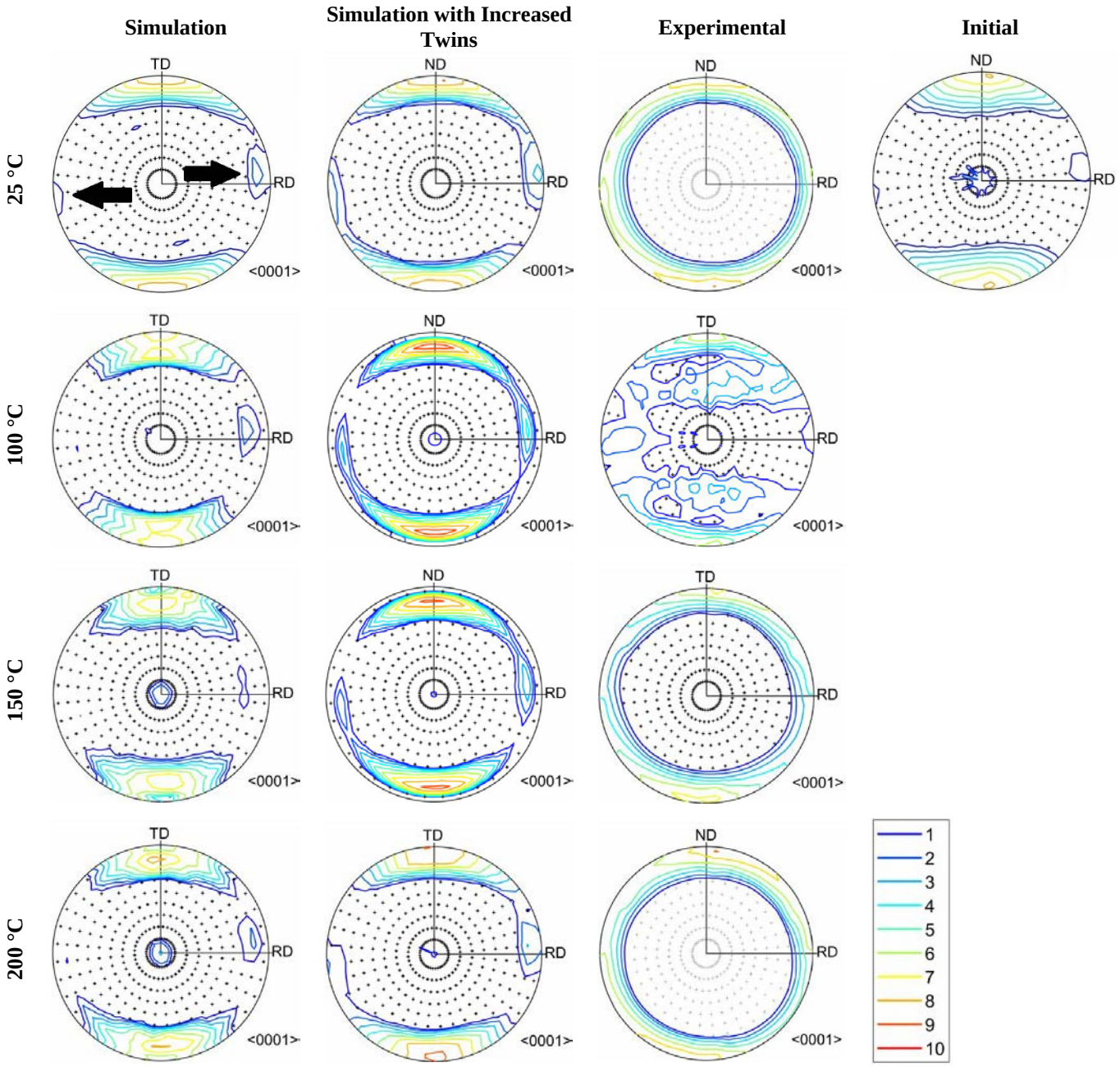

Figure 4.33 Tensile twin enhanced deformed (0001) pole figures of AZ31 for loading in the transverse direction at different temperatures. The original simulation, experimental, and initial pole figures are included for comparison.

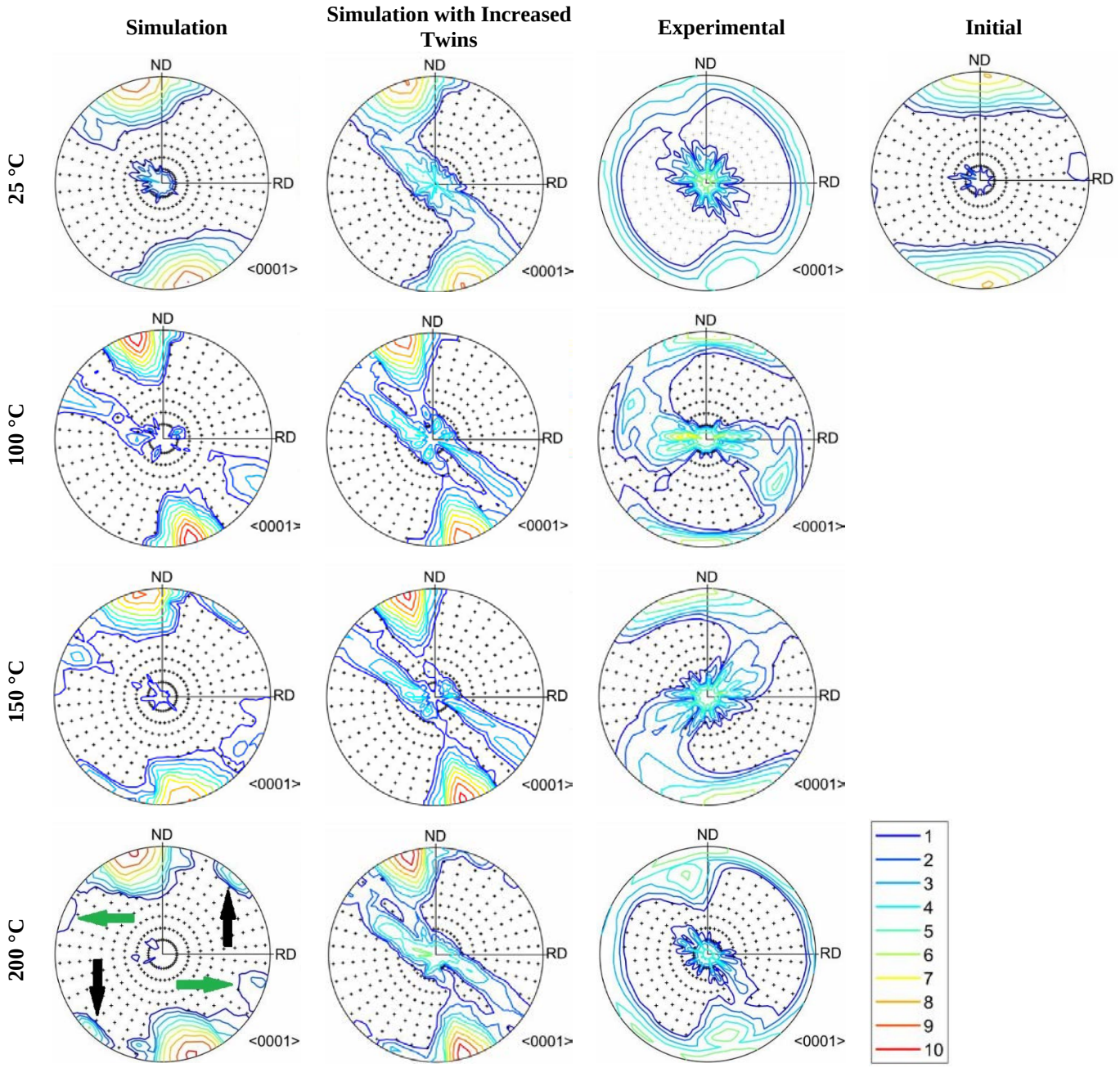

Figure 4.34 Tensile twin enhanced deformed (0001) pole figures of AZ31 for loading at 45° from the normal direction at different temperatures. The original simulation, experimental, and initial pole figures are included for comparison.

4.5 VPSC-T MODEL CONCLUSIONS

The VPSC-T model presented here is a modified VPSC model that includes the interaction matrix and drag stresses as temperature sensitive parameters. The varying interaction matrix and drag stresses are able to predict the shift of plastic deformation behaviour of the Mg alloy AZ31 over a range of temperatures, from 25 °C to 200 °C, and different loading directions. At room temperature, the main deformation mode is twinning, which changes to slip at elevated temperatures (>100 °C). The VPSC-T model is able to simulate the hardening behaviour and the textural evolution for each temperature and loading direction, in close agreement with experimental data. However, the main shortcoming of the model is its inaccuracy at 200 °C, as the model is unable to predict the DRX deformation mode and therefore the softening that has been experimentally observed.

Chapter 5 | DYNAMIC RECRYSTALLISATION VISCOPLASTIC SELF-CONSISTENT MODEL

5.1 HISTORY AND INTRODUCTION

The first complete and comprehensive DRX model implemented in a crystal plasticity framework was developed by Ding and Guo [23], which combined a CA model with the fundamental metallurgical principles of the DRX process. Ding and Guo's model was developed to bridge the dislocation activity with the microstructural evolution as a response to the thermomechanical process, allowing the accurate prediction of these behaviours [23]. This model was developed for an oxygen free high conductivity copper, by identifying key the relationships of the DRX process: the degree of DRX is related to the Zener-Holloman parameter, the nucleation rate, and the initial microstructure. This model can be adapted to other materials.

Ding and Guo's model's prediction of the microstructural evolution is achieved through the use of the CA model where a two-dimensional grid, representing grains, is given the ability to recrystallise by on the dislocation density. When one grain recrystallises, there is an increased propensity of recrystallisation to occur in one of the neighbouring grains, which aids in showing the directionality and shape of the DRX evolution. Since the Ding and Guo's model only defines the principles of the DRX process, it is necessary for it to be paired with another model in order to predict the microstructural behaviour, i.e. CA [23], FEM [106], and VPSC [83].

5.2 GENERAL DYNAMIC RECRYSTALLISATION MODEL FORMALISATION

The DRX process can be separated into three main components: the onset for DRX, the nucleation of the DRX grains, and the growth of the DRX grains. In general, the DRX

mechanism initiates under specific conditions and once these conditions are met, nucleation can occur. However, this alone is not sufficient to define the nucleation process, and probability function is used to determine the likelihood of the total DRX grain nucleation. Once the initiation and nucleation processes are satisfied, the growth phase of the DRX grain can finally occur.

5.2.1 Critical Onset of Dynamic Recrystallisation

The onset of DRX can be determined through two different methods: a critical strain [84, 100], or a critical dislocation density [15, 23-25] criterion. The critical strain for the onset of DRX is determined through the use of the experimental stress-strain curve and/or the work hardening curve [83-85, 89, 142-154].

In the model developed here, the onset of dynamic recrystallisation is determined through the use of a critical dislocation density. The following equation incorporating strain rate and temperature effects can be used to calculate the critical dislocation density [15, 23, 83, 89, 107, 152, 153]:

$$\rho_{crit} = \left(\frac{20\ Q_{gb}\dot{\varepsilon}}{3blM\tau}\right)^{\frac{1}{3}} \tag{5-1}$$

$$where\ M = \frac{b\delta}{kT} D_0\ exp\left(-\frac{Q_{diff}}{RT}\right) \tag{5-2}$$

$$where\ \tau = \frac{1}{2}\mu b^2 \tag{5-3}$$

where Q_{gb} is the grain boundary energy, l is the mean free path for dislocations, Q_{line} is the dislocation line energy of each slip mode, M is the mobility of the grain boundary , δ is the characteristic boundary thickness, k is the Boltzmann constant, D_0 is the diffusion

coefficient across the grain boundary, Q_{diff} is the activation energy for diffusion, and R is the gas constant.

5.2.2 Dynamic Recrystallisation Nucleation

Once the criterion for the onset of DRX has been met, the DRX process can proceed with the remaining two stages [23, 24, 107]: nucleation and growth of the DRX grains. These two stages become the controlling factors for the microstructural evolution as a result of DRX. There have been several models proposed to determine the nucleation rate of DRX [23], and these studies have shown that the nucleation rate is a function of the strain rate and temperature;

$$\dot{n} = C\dot{\varepsilon}^m \, exp\left(-\frac{Q_{diff}}{RT}\right) \tag{5-4}$$

where C is a constant and a fitting parameter, and m is a constant. Previous studies have shown the C value to be a constant and controlling parameter [15, 42, 83, 92, 106, 107, 155], or given as a materials constant [23, 85, 89, 92]. The exponent term, m, generally has value of 1 [23, 92, 155, 156] or 0.9 [15, 24, 42, 83, 89]. Some authors have used this term as a fitting parameter [85], or and others consider it as a materials constant [107].

The critical dislocation density is not sufficient to describe the nucleation behaviour of the DRX mechanism, as there are other factors involved during the nucleation process [15, 23, 24, 107]. A probability function, in terms of the surface energy of the parent grain and nucleation rate, is necessary to determine the actual likelihood of DRX grain nucleation [15, 24].

$$P(\dot{n}) = \frac{4}{3}\pi r^3 \dot{n} \Delta t \tag{5-5}$$

where r is the radius of the parent grain, and Δt is the time step increment.

5.2.3 Dynamic Recrystallisation Grain Growth

The growth rate of the DRX grains is quantified through the grain boundary velocity, V, which is expressed through the mobility of the grain boundary, M, and the driving force, P [23, 89]:

$$V = MP \tag{5-6}$$

The driving force is quantified through the stored energy disparity between grains, which are quantified from the dislocation density and grain boundary variations between the parent and DRX grains [15, 23, 24, 42, 58, 83, 85, 89, 92, 107, 148, 150, 155-159]:

$$P = \frac{1}{2}\mu b^2\left(\rho_p - \rho_r\right) - \frac{2}{r_r}\gamma \tag{5-7}$$

where ρ_p and ρ_r are the dislocation densities for the parent and new DRX grains, respectively, r_r is the radius of the DRX grain, and γ is the misorientation angle between the parent and DRX grains.

A number of authors have found success in using a simplified version of Equation (5-7) for modelling the DRX process of Mg alloys [15, 42, 58]. The driving force for CDRX in Mg alloys can simply be regarded as the stored energy disparity between the parent and DRX grains, following the equation:

$$P = \frac{1}{2}\mu b^2(\rho_p - \rho_r) \tag{5-8}$$

The simplification of Equation (5-7) is possible, in part, due to the active CDRX mechanism in these studies [15, 42, 58]. Since the newly nucleated grains have the same

texture as the parent grain, the misorientation angle, in Equation (5-7), between the parent and DRX grain is zero.

5.3 VISCOPLASTIC SELF-CONSISTENT DYNAMIC RECRYSTALLISATION MODELLING

The new version of the Ding and Guo's DRX model is integrated within the temperature sensitive VPSC model, VPSC-T, coupled with a composite grain twinning model. This is realised on the Mg alloy AZ31 at low to moderate temperatures where a mixture of slip and twinning modes are active, each with a different influence on the DRX behaviour. The VPSC model utilises a dislocation density hardening law, enabling the nucleation of DRX grains in the VPSC-DRX model to be based on a critical dislocation density criterion as described in Chapter 3. The VPSC model's dislocation density evolution of a grain is dictated by Equation (3-28), and when the dislocation density of any grain exceeds the critical value calculated in Equation (5-1), DRX can occur.

Once the DRX grains have successfully nucleated, according to the probability function, the model ultimately calculates the grain boundary velocity, which is able to dictate the growth of the DRX grains through the evolution of the DRX grain radius using the following equation;

$$r_{new} = r_{old} + \Delta r = r_{old} + V\Delta t \tag{5-9}$$

where r_{new} and r_{old} are the new and old radius of the DRX grains. The newly formed DRX grains are assumed to nucleate into perfect spheres, free of any imperfections, allowing the nucleating volume to be governed by the nucleating radius and the volume of a sphere;

$$V_{DRX} = \frac{4\pi}{3} r_{nuc}^3 \tag{5-10}$$

where V_{DRX} is the volume of the DRX grain. This volume is then compared to the volume of the parent grain, to calculate the DRX grain volume fraction:

$$v_{grain} = \frac{V_{DRX}}{V_{Parent}} * v_{Parent} \tag{5-11}$$

where v_{DRX} and v_{Parent} are the volume fraction of the DRX and parent grains, respectively, and V_{Parent} is the volume of the parent grain. As most materials have an average grain size of tens of microns, the nucleating radii of DRX grains are in the submicron range (100 nm to 1 μm), the resulting initial volume fractions of the DRX grains are very small with a magnitude of 10^{-8}~10^{-11}. As a result, the DRX grain must grow to an initial threshold limit, which is a fraction of the DRX grain, before it starts influencing the behaviour of the material and therefore being counted as an actual grain in the model.

5.4 DYNAMIC RECRYSTALLISATION MODEL ALGORITHM

Beyond the DRX onset criterion, the DRX process can be split into two stages, which is reflected in the VPSC-DRX model; the first stage defines the nucleation of DRX grains (VPSC-DRX-Nucleation), while the second stage defines the growth of the grains (VPSC-DRX-Growth). Using a simplified flow chart of the VPSC model from Figure 3.2, the integration of the DRX framework into the VPSC model is shown in the flow chart in Figure 5.1.

The VPSC model relies on dislocation density based constitutive laws to describe the hardening behaviour of the deformation modes, wherein the dislocation density is updated.

Here the VPSC-DRX model checks the dislocation density across all parent and twinned grains against the critical dislocation density. If the dislocation density of a particular grain reaches the critical threshold value, the grain is flagged for potential DRX nucleation, and the probability function is used to determine whether a DRX grain can be nucleated.

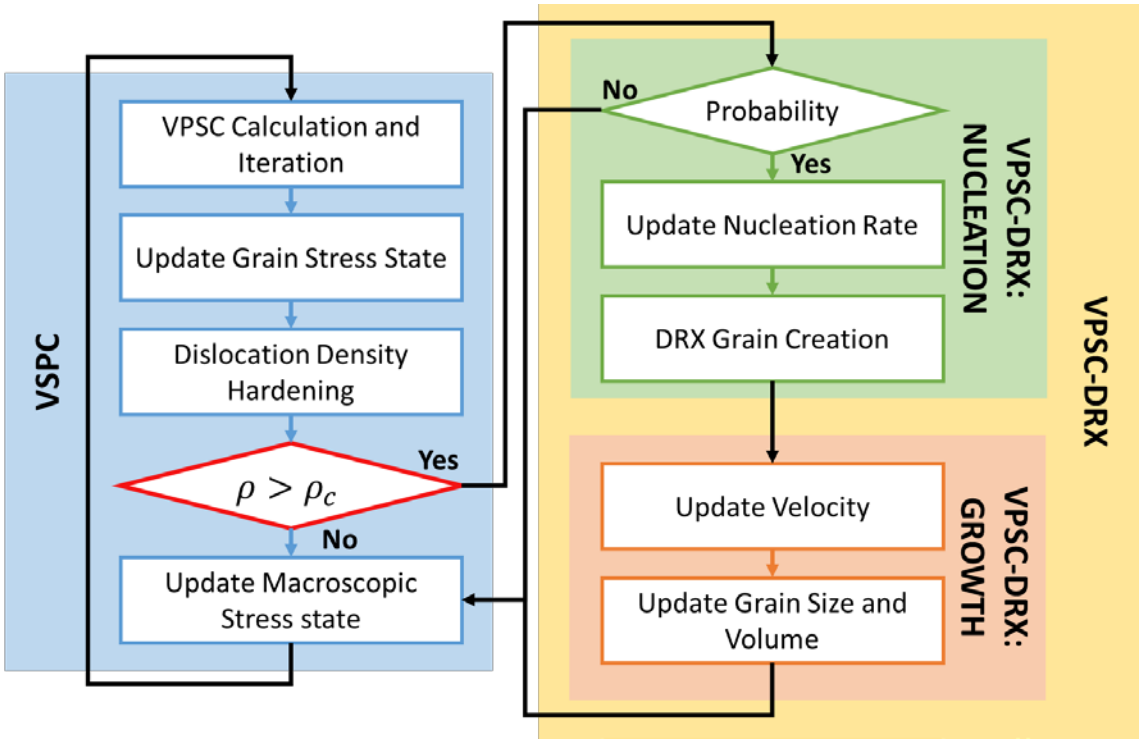

Figure 5.1 Flowchart of the VPSC-DRX model within the VPSC algorithm.

The VPSC-DRX-Nucleation model only creates a “pseudo” DRX grain, where a grain is only nucleated in the background and not part of the VPSC calculation. This pseudo nucleation is implemented in part to reduce the computational time and load, by avoiding calculations across insignificant grains. This new pseudo-DRX grain becomes a “full” grain once it reaches a predefined grain size, after which a volume fraction is calculated. A dislocation density and a crystallographic orientation are assigned to this new “full” grain in preparation for the growth phase. Additionally, there is a limit placed on the

number of DRX grains that can be nucleated in each parent or twinned grain, in order to reduce the computational load and time.

The VPSC-DRX-Growth model calculates the grain boundary velocity to be used for the growth of each DRX grain. If a pseudo-DRX grain grows to reach a threshold size (when the volume fraction of the DRX grain becomes 1% of the parent), a DRX grain is finally created within the model, and will be used to calculate the macroscopic behaviour of the material using the VPSC formalisation. In addition, the VPSC-DRX-Growth model monitors the growth of the DRX grains in order to prevent the sum of the volumes of all the DRX grains and the remaining volume of the initial grain to be larger than the initial parent grain volume. A second check is done on the DRX growth to ensure that each DRX grain does not reach a volume larger than a threshold value that corresponds to a given fraction of the original grain. If a DRX grain reaches either threshold values, then it cannot grow anymore.

5.5 PARAMETERS FOR DYNAMIC RECRYSTALLISATION MODELLING

During the DRX process, the newly formed DRX grains are assumed to be nearly perfectly crystalline or devoid of any flaws. In this model, the newly nucleated DRX grains are assigned values that are considered perfectly crystalline when compared to the deformed parent grains [23, 89, 100, 156]. In this study the newly formed DRX grains are assigned a dislocation density of $10^4\ m^{-2}$, which is considered perfect in comparison to the parent grains that have an initial dislocation density of $10^{13}\ m^{-2}$.

Once the DRX grain is created, a crystallographic orientation is assigned to the new grain. There are various mechanisms by which Mg alloys deform through, as such this initial

DRX crystallographic orientation will be critical to describe the DRX process. This new orientation of the DRX grain is dependent on the DRX type, as DDRX and CDRX have their own microstructural evolution [74, 78, 79, 81, 86, 88, 91, 93, 94, 99]. At low temperatures, the DRX process in Mg alloys is CDRX where the newly formed DRX grains have a similar crystallographic orientation as the parent grain. At elevated temperatures DDRX is active in Mg alloys, and newly nucleated DRX grains have a crystallographic orientation with a HAGB with respect to the parent grain. Previous studies have modelled the DRX behaviour either by assigning random crystallographic orientations to the newly formed DRX grains [15, 23, 100] or by assigning the same crystallographic orientation as the parent to the newly formed grains [100], to reflect DDRX or CDRX, respectively.

In this model, the newly formed DRX grains are assigned crystallographic orientations that are linked to the parent grains' crystallographic orientations through a randomising process. This is achieved through a random number generator that is used to define an axis for rotation, with a set rotation angle of 15°, to generate a rotation matrix. The crystallographic orientation of the new DRX grain is calculated by rotating the parent grain's orientation using the defined rotation matrix. Every time a new DRX grain is created a new rotation matrix is calculated. The values of the parameters used in this study can be found in Table 5.1. Additionally, a variety of different parametric studies were conducted in this study to show the importance of various properties of the DRX grains. The results will be presented in the next chapter.

Table 5.1 Parameters for DRX modelling of the AZ31 Mg alloy.

Material Constant	Value	Units	References
Interfacial Energy, Q_{gb}	0.34	J/m^2	[160]
Characteristic Thickness, δ	$1.2x10^{-9}$	M	[107, 158]
Diffusion Energy, Q_{diff}	135	kJ/mol	[88, 161, 162]
Diffusion Coefficient, D_0	$5.59x10^{-2}$	m^2/s	[162]
Nucleation Pre-exponential, C	$2.5x10^{30}$	$(s^{-1}m^{-2})$	[24]
Nucleation Exponential, m	1	-	[23, 92, 155, 156]
Nucleating Dislocation Density, ρ_0^{drx}	10^4	$1/m^2$	[23, 89, 100, 156]
Radius of Nucleation, r	1	μm	Fitting Parameter

Chapter 6 | Results and Discussion of Dynamic Recrystallisation Modelling

6.1 Mechanical Response

6.1.1 Prediction of the Stress-Strain Response at 200 °C

The model described in the previous chapter was used to predict the deformation behaviour of the Mg alloy AZ31 that was presented in Chapter 4 of this thesis. These new simulations utilises the same initial texture (see Figure 4.1), the same hardening parameters (see Tables 4.1 - 4.3) as presented in Chapter 4, and the DRX parameters were defined in the previous chapter.

The simulation stress-strain curves at 200 °C from the VPSC-DRX model are represented by the lighter curves in Figure 6.1 and they are in good agreement with the experimental curves represented by the dotted lines for the TD and ND45 cases. The curves also show a similar softening behaviour after a peak stress showing the presence of DRX during deformation. The main difference between the simulations and experimental results is the initial hardening behaviour at strains below 7.5%, where the simulations show a higher degree of hardening than those found in the experimental curves in both the ND45 and TD cases, while the ND case fits the experimental curve quite closely. The peak stresses of the simulation results are marginally greater than the experimental data. Despite these discrepancies, the VPSC-DRX model is able to successfully predict the deformation behaviour of the Mg alloy and especially the DRX process.

However, for the ND case, the simulation does not predict a softening behaviour as it is observed in the experimental curve. One possibility for this deviation, is that there is early fracture occurring in the ND loading direction, as it appears to have a reduced ductility

when compared to the other loading directions. Another possibility is that there is a stronger influence from the increased twinning seen in this loading direction, than anticipated, allowing for more twin-assisted DRX, which is not accounted for in this model.

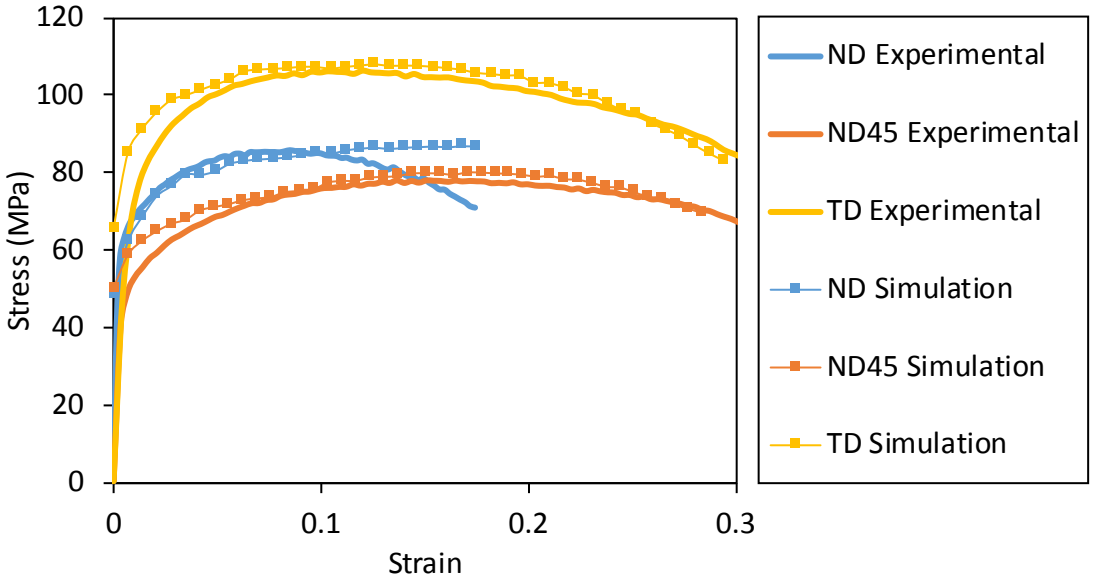

Figure 6.1 Stress-strain curves of AZ31 at 200 °C in the: normal direction (blue), transverse direction (yellow), and 45° from the normal direction (orange). The solid lines represent the experimental results while the dotted lines represent the simulation data.

When the ND simulation model is run to larger strains, the softening mechanism is then observed as with the other loading directions (see Figure 6.2). Figure 6.2 shows that the VPSC-DRX model can predict the anisotropic behaviour of the Mg alloy, with the peak stress occurring at different strains. This anisotropic behaviour is also highlighted in the difference in the yield strengths with each loading direction. The lowest yield strength is 45 MPa for the ND45 case, 48 MPa for the ND case, and the TD case has the highest yield strength at 65 MPa.

The VPSC-DRX model monitors each grains dislocation density to determine the DRX behaviour and can also be used to determine the validity of model. The VSPC-DRX

model predicts an average dislocation density of $3.56 \times 10^{12}\ m^{-2}$, $5.47 \times 10^{12}\ m^{-2}$, and $3.44 \times 10^{12}\ m^{-2}$ for the ND, TD, and ND45 loading directions, respectively, lower than the initial dislocation density of $10^{13}\ m^{-2}$. Several experimental studies show that the average dislocation density decreases due to DRX causing the creation of near-perfect grains [150, 163, 164], which is reflected by the model.

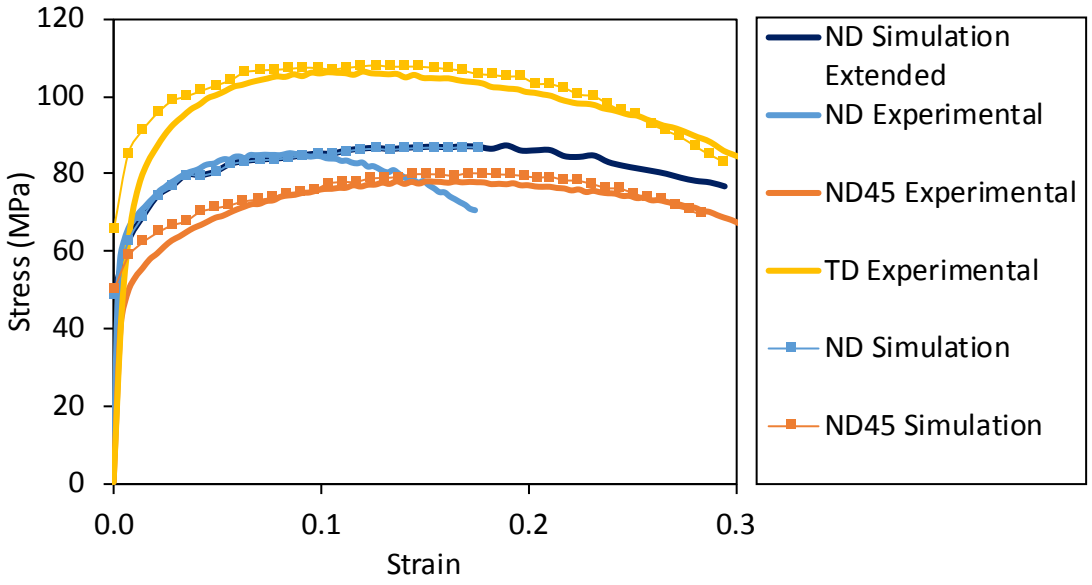

Figure 6.2 Stress-strain curves of AZ31 at 200 °C showing the DRX softening in the ND loading direction in the dark blue line.

6.1.2 Dynamic Recrystallisation Softening Mechanism

Figure 6.3 compares the experimental data and the VPSC model with and without DRX, which highlights the softening behaviour that accompanies DRX across the three loading directions. The peak stress occurs in the simulations at a lower strain for TD ($\varepsilon = 11\%$) while in ND and ND45 ($\varepsilon = 18\%$). The peak stress occurring at a lower strain in the TD case can be attributed to the increase slip activity for this particular loading direction, due to the anisotropic nature of Mg [17, 19, 39, 41]. In the two other loading directions, there is some twinning activity as Mg alloys tend to twin at the deformation temperature (200 °C) [8, 9, 12], which allows for the possibility of twin-assisted DRX [15, 31]. The

increased slip activity results in a quicker accumulation of dislocations, with the dislocation density able to reach the critical value at lower strains.

6.1.3 Deformation Stress-Strain Curves at Lower Temperatures

Since the VPSC model used in this study is a temperature sensitive model, it can accurately predict the deformation behaviour of the Mg alloys AZ31 for temperatures ranging from 25 °C to 200 °C (Figure 6.4). At the lower temperatures, twinning deformation is the dominant mechanism; it creates a downward curvature in the stress-strain curves that are observed experimentally at 25 °C and 100 °C (Figure 6.4a & b). As the temperature increases to 150 °C there is a shift to a dislocation slip dominant deformation mode for the ND and ND45 cases, seen in Figure 6.4c where the downward curvature is no longer evident [8, 9]. The VPSC-DRX model is able to predict the lack of DRX, which is associated with a softening behaviour [8, 15, 24, 30, 82-89], across all loading directions. It should be noted that DRX is observed, although with minor effect, at 150 °C. The low temperature results are similar to those found through the VPSC-T model described in Chapter 4.

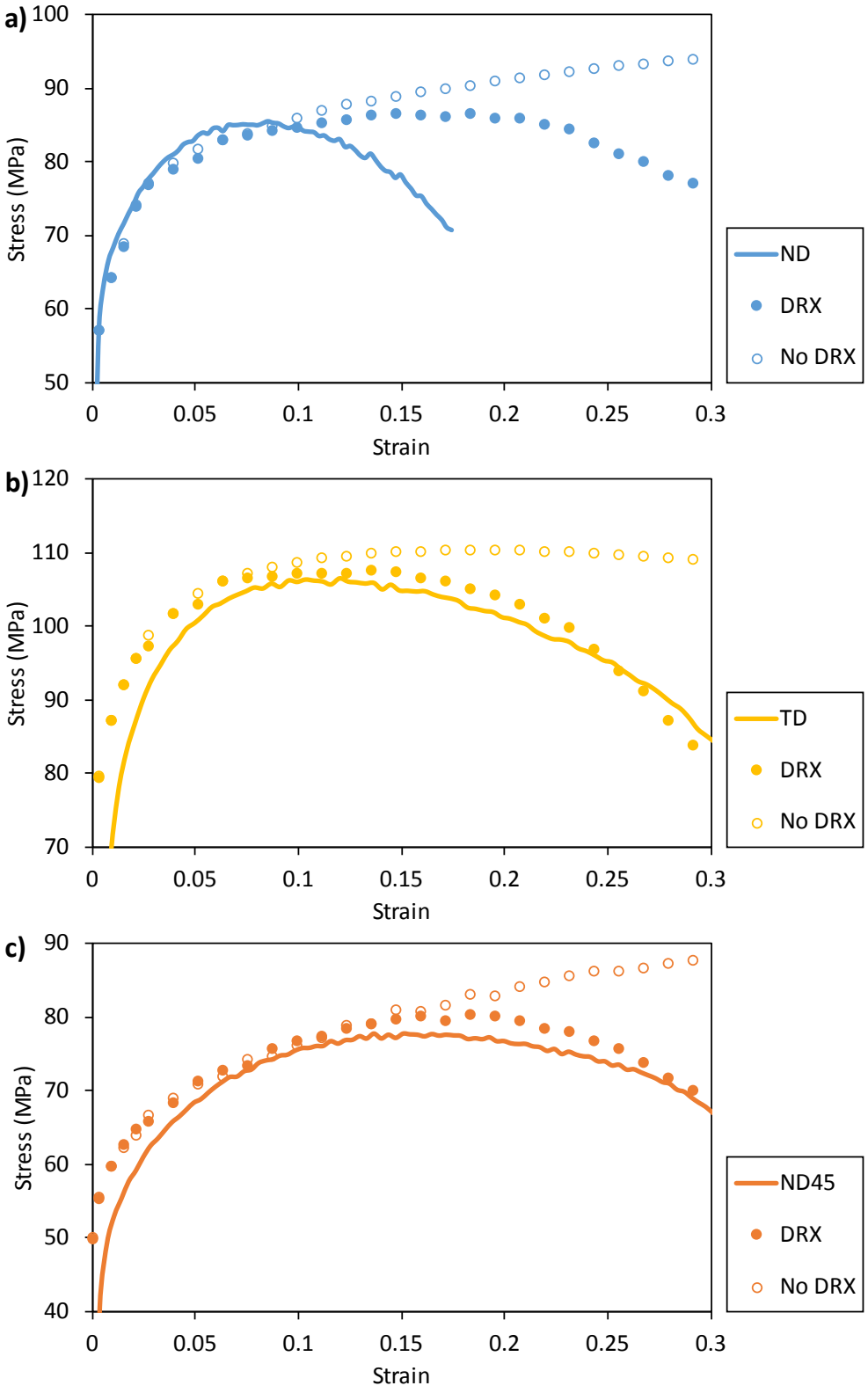

Figure 6.3 Comparison of experimental, VPSC, and VPSC-DRX models for the: (a) normal direction, (b) transverse direction, and (c) 45° from the normal direction. The experimental is shown through a solid line, and the VPSC and VPSC-DRX model in hollow and filled circles, respectively.

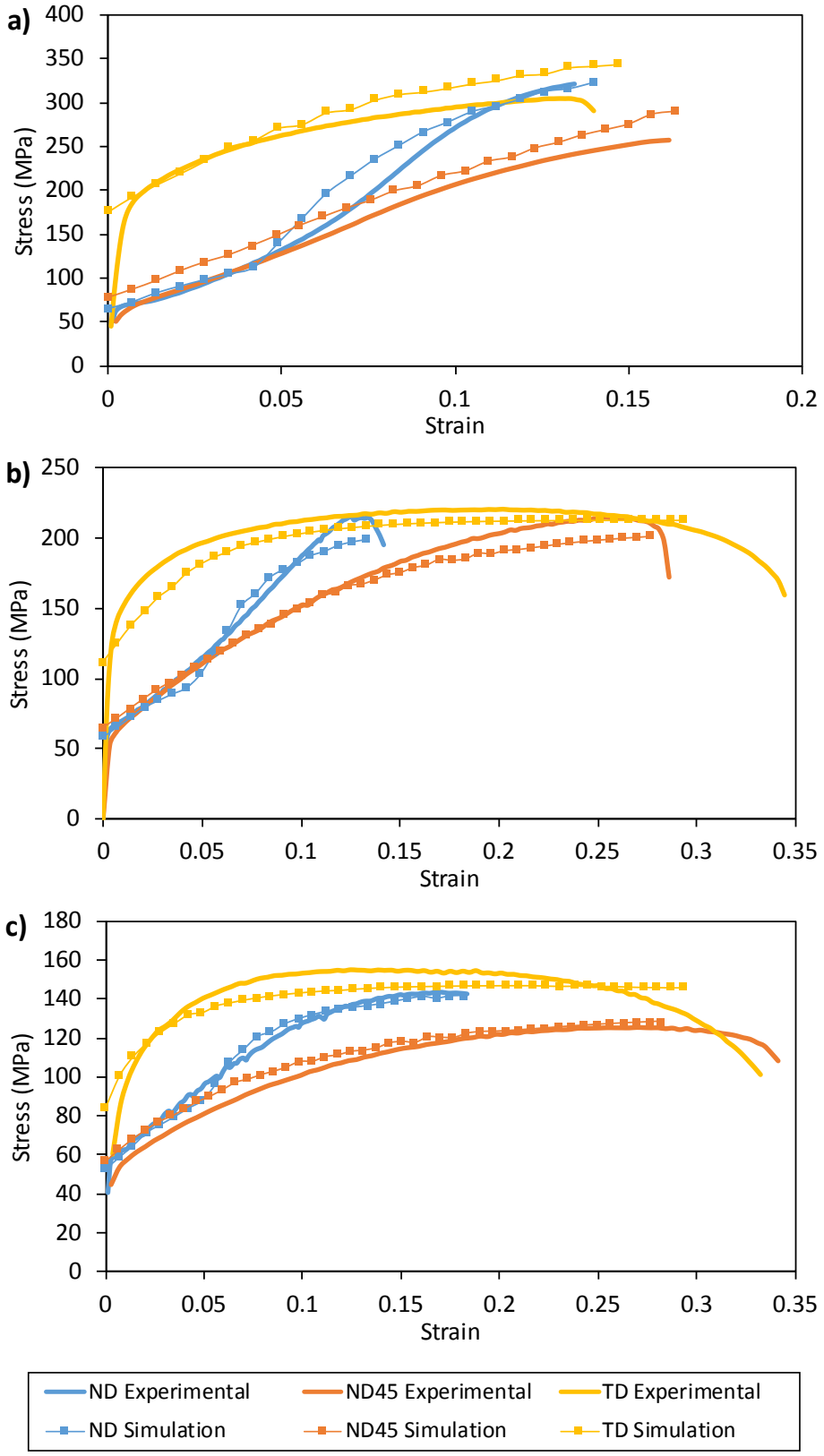

Figure 6.4 Stress-strain curves for the three loading directions at: (a) 25 °C, (b) 100 °C, and (c) 150 °C. The solid lines represent the experimental results while the dotted lines represent the simulation data.

6.2 DEFORMATION MECHANISM ACTIVITIES

All the deformation mechanism activities, predicted by the model, within the parents, twinned, and DRX grains for the three different loading directions at 150 °C and 200 °C can be found in Figure 6.5 and Figure 6.6, respectively. Basal slip, represented by the blue lines, is active and the dominant deformation mode at both temperatures and for all three loading directions, which is expected as the CRSS for basal slip is the lowest of all deformation modes as predicted by literature [1, 16, 31, 41, 52, 56]. The yellow lines illustrate the tensile twinning activity and can be seen in all loading directions at both temperatures, as predicted by literature [19, 28, 31, 39, 43, 52]. Tensile twinning is only active at strains lower than 10%, at which point hardening for twinning has increased the CRSS to a level where other modes will be activated. This is seen by an increase in the overall slip activity with the introduction of pyramidal slip, represented by the grey lines [28, 43, 52].

At 150 °C, the tensile twinning activity decreases from 45% to 15% when the loading direction changes from ND to ND45, and to 5% for the TD case, showing the anisotropic nature of the mechanical behaviour of this material [8, 17, 19, 31, 52]. This decrease in the twinning activity correlates to an increase in the prismatic slip activity to 5%, 10%, and 45%, as indicated by the orange lines, for the ND, ND45, and TD cases, respectively. This has also been observed in other studies [17, 19, 39]. Due to the small number of DRX grains formed at 150 °C (Figure 6.7), there is only a negligible level of deformation activity in these grains in all three loading directions. It should be noted that at 25 °C and 100 °C there is no DRX occurring, and as a result, the activities at these temperatures are omitted, as they will be similar to the ones presented in Chapter 4.

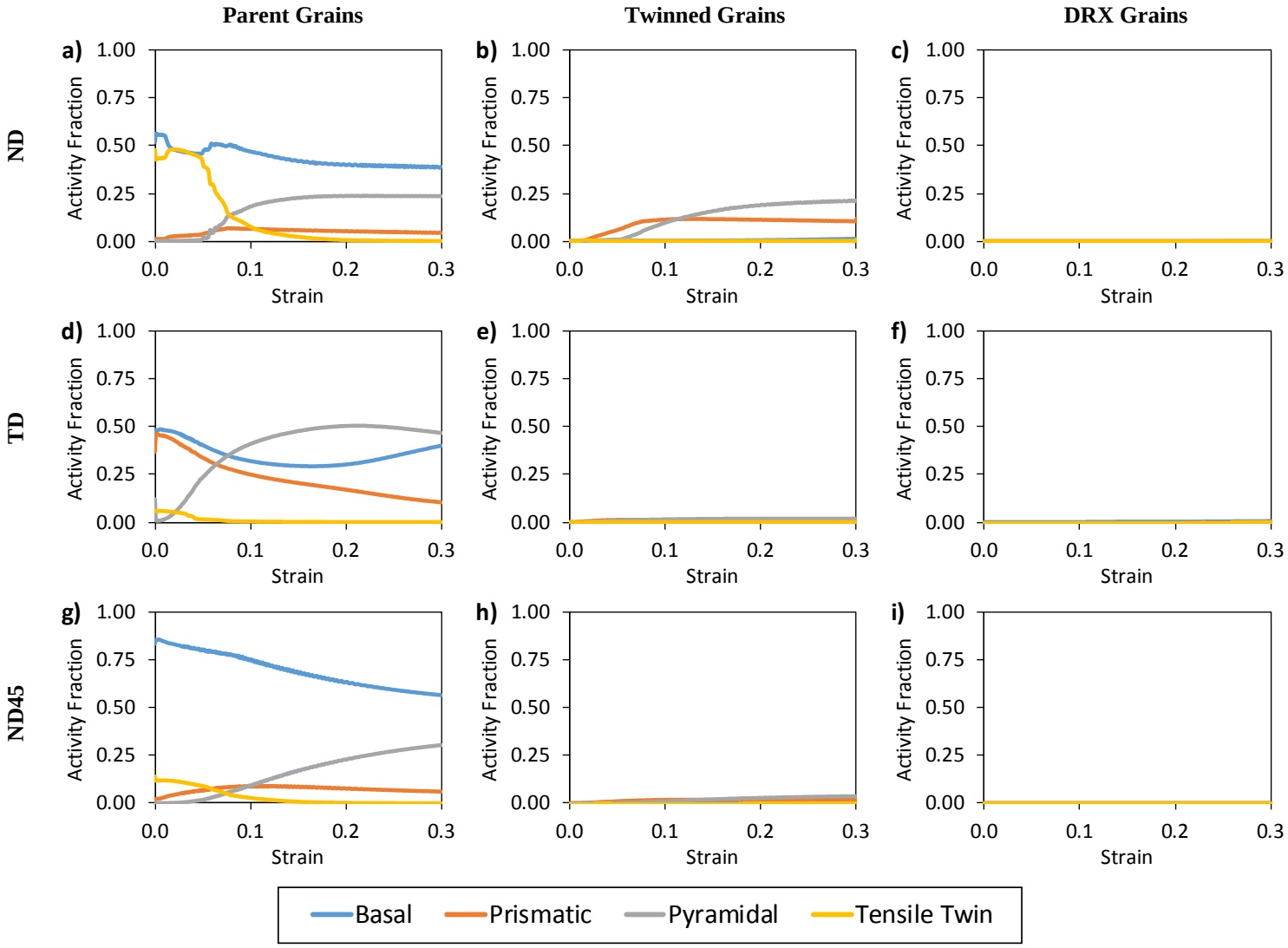

Figure 6.5 Deformation activities in the parent, twinned, and DRX grains at 150 °C in the three loading directions: (a-c) normal direction, (d-f) transverse direction, and (g-i) 45° from the normal direction.

At 200 °C, the active deformation modes are similar to those observed at 150 °C, with lower levels of tensile twinning as deformation slip is temperature sensitive (see Figure 6.6); this is what is expected from literature [8, 9]. In the ND loading direction, this results in an increase in the peak activity for basal slip from 56% at 150 °C to 62% 200 °C. Pyramidal slip starts to be activated at lower strains, $\varepsilon = 0\%$ as it has been shown previously in other studies [28, 43, 52]. These two effects are also seen in the ND45 case, but to a lower extent, with the basal slip activity increasing from 85% at 150 °C to 88%

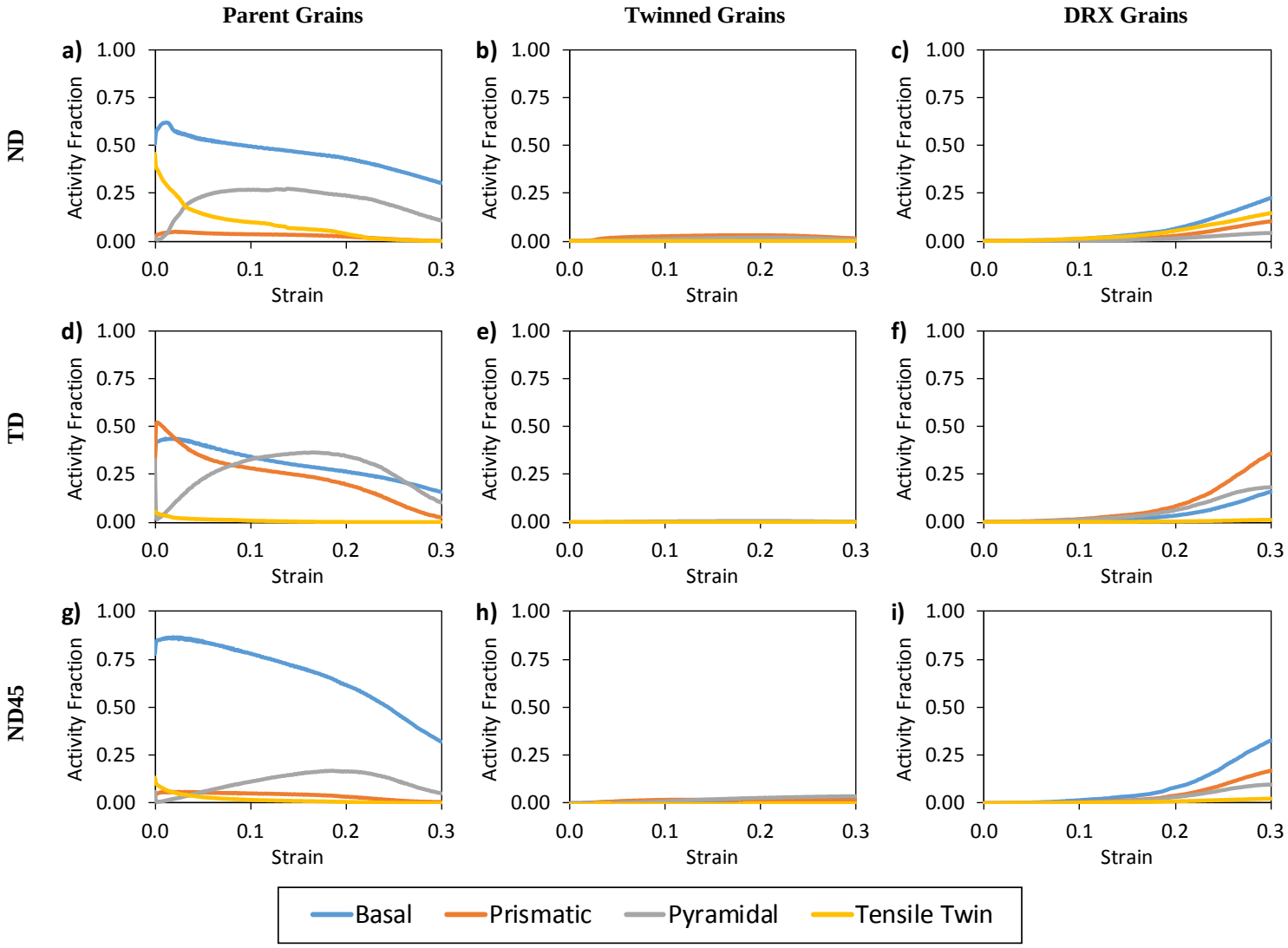

Figure 6.6 Deformation activities in the parent, twinned, and DRX grains at 200 °C in the three loading directions: (a-c) normal direction, (d-f) transverse direction, and (g-i) 45° from the normal direction.

at 200 °C. In the TD case, there is a larger prismatic activity at 200 °C with 52% of the total strain accommodation while it is only 46% at 150 °C. This is agreement with previous studies [17, 19, 39]. At higher levels of strain ($\varepsilon > 15\%$ in Figure 6.6) there is a distinct drop in the activity fractions for all deformation modes in the parent grains, owing to the increasing size of DRX grains that allows deformation to occur in those grains instead.

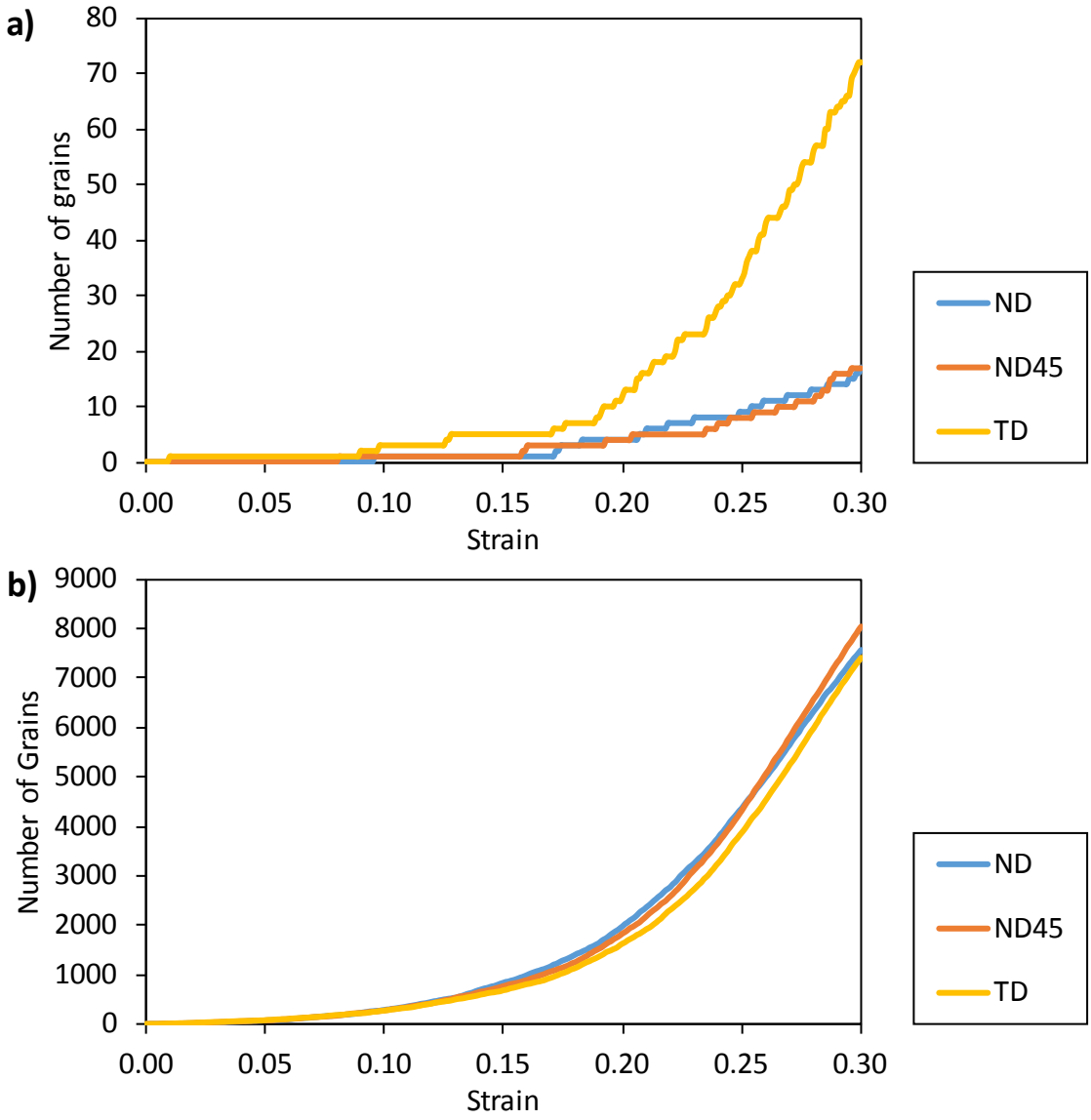

Figure 6.7 Number of DRX grains formed for the three loading directions at: (a) 150 °C and (b) 200 °C. It should be noted that the y-axis is not the same in both graphs.

At higher strain levels ($\varepsilon > 15\%$) there are more DRX grains being formed (Figure 6.7), and there is an increasing level of activity in the DRX grains. The deformation modes in the DRX grains is the same as that observed in the parent grains; the main deformation mechanism is a combination of tensile twinning and slip. Figure 6.6 shows a variation in the deformation behaviour between the parent and DRX grains. This variation can be explained through the DRX grains reorientating to preferentially activate different deformation modes and the newly formed DRX are near-perfect and are comparatively

softer than their parent grains. Basal slip, with its low CRSS, is the main mechanism at a peak deformation activity of 22%, 32%, and 15% for ND, ND45, and TD cases, respectively. In Figure 6.5 and Figure 6.6, twinning activity is shown to be dependent on the loading direction, and this is also reflected in the DRX grains with a peak deformation activity of 14%, 2%, and 1% in the ND, ND45, and TD cases, respectively. Similarly, due to the lack of twinning, there is an increase in the overall slip activity at a peak deformation activity of 10%, 16%, and 36% for prismatic slip, and 4%, 10%, and 18% for pyramidal slip in the ND, ND45, and TD cases, respectively. It has been shown that the DRX mechanism is often found in the presence of basal and pyramidal slip, and twinning, which are all active at this temperature [78, 81, 86, 91, 94, 98, 99, 101, 105].

Figure 6.8 illustrates the trends of the total deformation activities at 150°C and 200°C in the ND, ND45, and TD loading directions without and with DRX (incorporating data from Figure 4.19). Overall, there is an increase in the basal and prismatic slip activities in each loading direction as a result from the inclusion of the DRX model. Here the newly formed near-perfect DRX grains are presumed to deform primarily through the basal slip mode; basal slip has the lowest CRSS values for DRX grains. Similarly, the newly formed DRX grains has the potential to be reorientated favourably to activate the prismatic slip. The combination of the two effects results in a significant decrease in the total pyramidal activity.

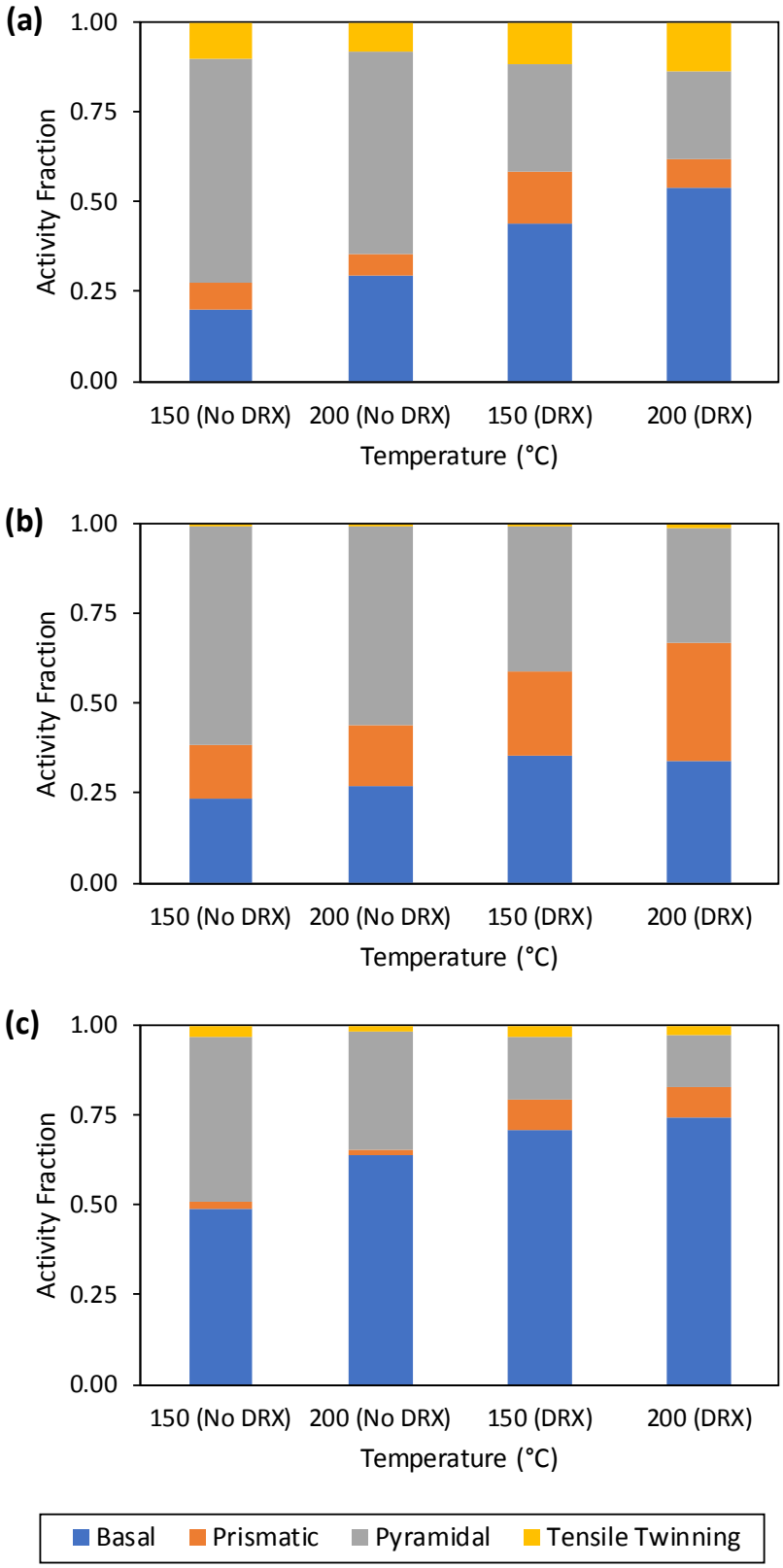

Figure 6.8 Comparison of the total deformation activities without and with DRX at different temperatures in the: (a) normal direction, (b) transverse direction, and (c) 45 from the normal direction

6.3 DYNAMIC RECRYSTALLISATION VOLUME FRACTIONS

The volume fractions of each phase, parent grains, twinned grains, and DRX grains, can be found in Figure 6.9. These figures show the decrease in the tensile twinning activity from 150 °C to 200 °C through the lowered twinned grain volume fraction. It should be noted that there is no significant DRX activity at 150 °C, achieving a total of 0.1% volume fraction at the end of the simulation across all loading directions. Additionally, the DRX activity can be seen at 200 °C in the increase of DRX grain volume fraction as strain increases, as it has been shown experimentally and in simulations [25, 30, 83-87, 89, 91, 107, 159].

The ND direction at 150 °C (Figure 6.9a) shows the larger level of tensile twinning activity among the three loading directions with a total of 37% volume fraction of twinned grains at the fracture strain ($\varepsilon = 30\%$). The overall decrease in tensile twinning activity at 200 °C (Figure 6.9b) can be seen in a lower twinned grain volume fraction of 15% at the strain $\varepsilon = 10\%$, leading to a total of 28% volume fraction at the fracture strain.

As the loading direction changes to the ND45 direction, there is also a decrease in the tensile twinning activity between 150 °C (Figure 6.9c) and 200 °C (Figure 6.9d) as the loading direction is no longer favourable for tensile twinning activation. This is shown through a total twinned grain volume fraction of 11% at the fracture strain at 150 °C. The same effect is seen in the TD direction with a total twinned grain volume fraction of 3%. Furthermore, at 200 °C this effect is increased, resulting in a twinned grain fraction for

ND45 of 3%, and 1% for the TD case, which reflects the reduced level of tensile twinning activity shown in Figure 6.6.

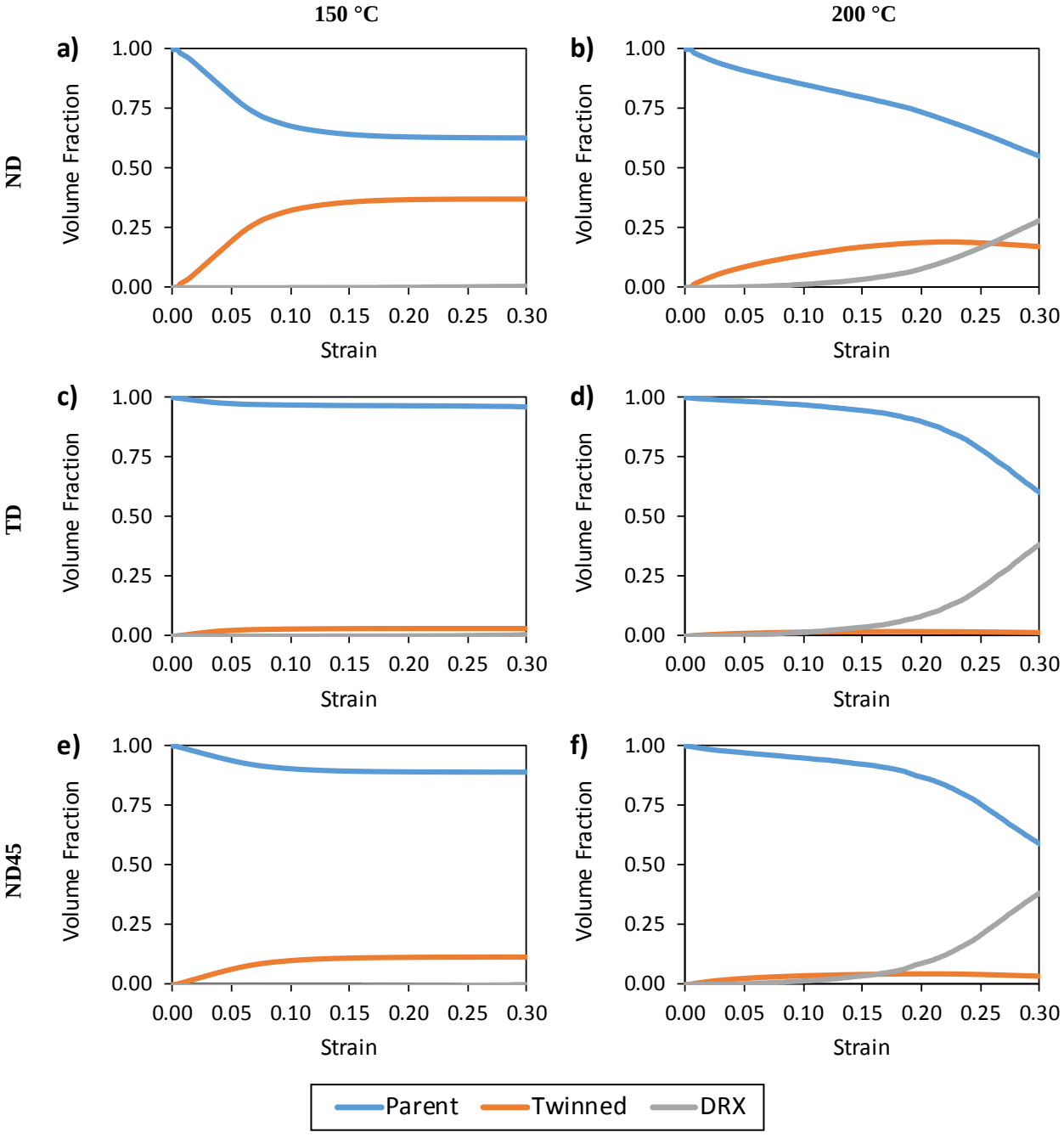

Figure 6.9 Volume fractions of the parent, twinned, and DRX grains at 150 °C and 200 °C in the three loading directions: (a, b) normal direction, (c, d) transverse direction, and (e, f) 45° from the normal direction.

Figure 6.7 shows the number of DRX grains with increasing strain for all loading directions. At 150 °C there are only a few DRX grains created, 18 grains for the ND and ND45 cases and 80 grains for the TD case, which correlates to the extremely low DRX volume fraction in Figure 6.9. At 200 °C, the increased level of DRX activity results in a large number of DRX grains formed; there are 7576, 8027, and 7429 DRX grains formed in the ND, ND45, and TD loading directions, respectively. At a strain of 10%, there is an average of 275 DRX grains formed across the loading directions, and at $\varepsilon = 20\%$ there is an average of 1800 DRX grains. The corresponding volume fractions of the DRX grains at strain $\varepsilon = 10\%$ and $\varepsilon = 20\%$ are 1.5% and 8.4%, respectively. This shows that the majority of the DRX grains are only formed at higher levels of strains where there is sufficient slip activity and, subsequently, dislocation accumulation.

6.4 DEFORMED POLE FIGURES

The experimental and predicted (0001) PF for each loading direction are shown in Figure 6.10. The initial (0001) PF (Figure 4.1) presented a strong basal texture with most grains having their c-axis parallel to the ND direction. Tensile twinning causes significant textural changes as we can see in the experimental PFs with a fraction of grains with their c-axis oriented normal to ND after deformation; tensile twinning rotates grains by 86° [31, 78, 81, 94, 101]. This is observed in the ND and ND45 cases where there is a large intensity region in the centre of their respective PF in Figure 6.10, as these orientations deformed through both twinning and slip [8]. In the TD case, the main deformation mechanism is slip deformation [15], which does not cause large grain rotations. This is

reflected through the deformed textures (Figure 6.10) being quite similar to the initial texture (Figure 4.1).

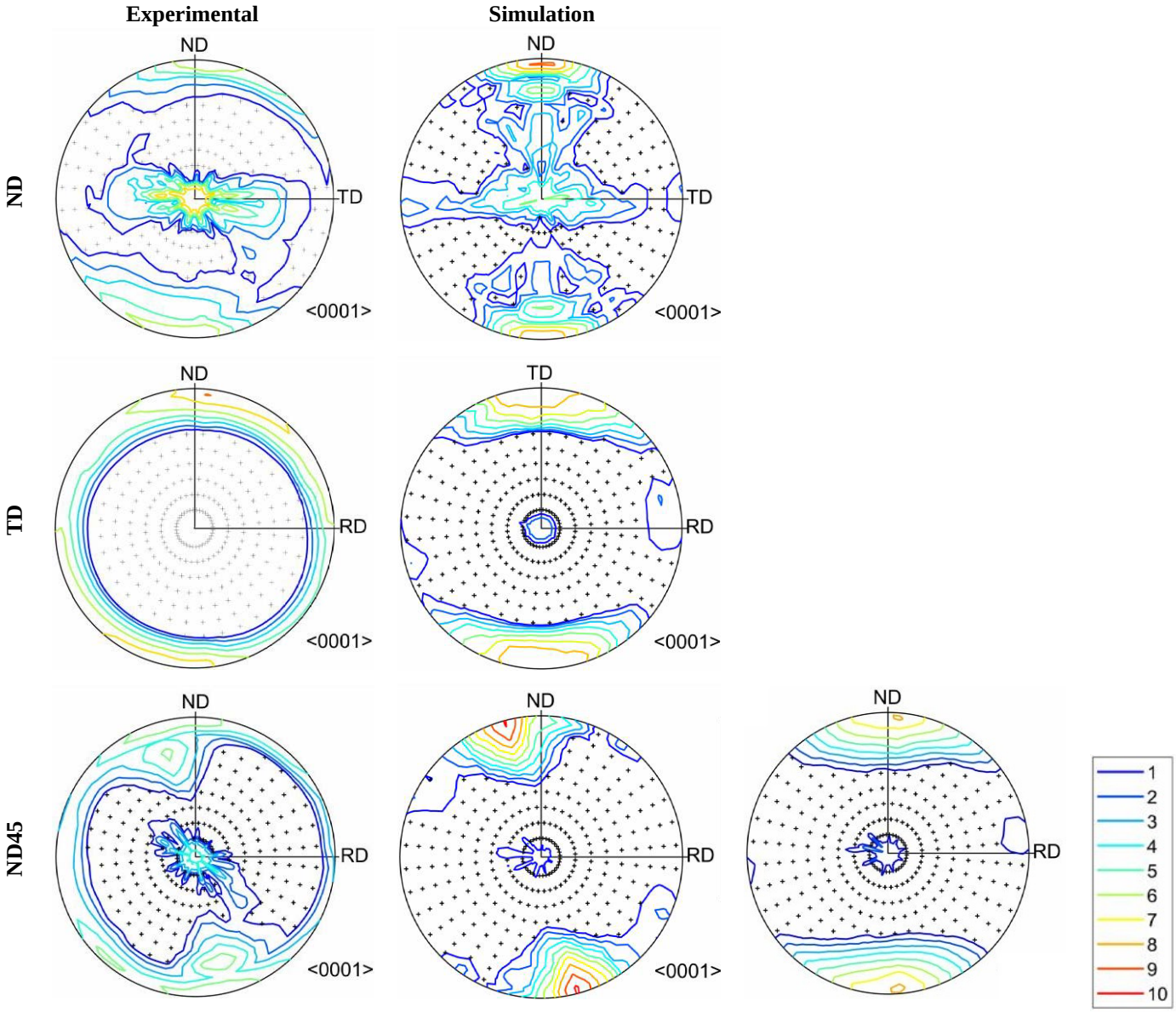

Figure 6.10 Simulation and experimental (0001) pole figures for loading at 200 °C at 18% strain for ND, and 30% strain for TD and ND45. The initial pole figure is included for comparison.

Both experimental and simulated PF are similar. The TD case shows a similar basal texture, the main difference between the experimental and simulated PFs is the lack of the orthotropic symmetry in the simulated PF. While in the ND case, the predicted PF shows the strong basal texture with a high intensity in its centre due to twinning. The texture evolution as a result of the DRX process is expected to be minimal as the DRX

grains have similar crystallographic orientations with the parents grains, which is shown through the high intensity regions along the ND direction of the PFs in Figure 6.10 [7, 11, 12, 75-78, 102].

A similar effect is found in the ND45 case, with a very strong basal texture still present after deformation and small high intensity region in the centre of the PF due to the presence of the twinned grains. The experimental PF shows a significant twinned grain volume fraction that was not predicted by the model. One possibility for this discrepancy is the fact that the experimental texture measurements were conducted close to the fracture surface where large twinning activity is expected than in the rest of the coupon.

A secondary study, similar to Section 4.4.6, was conducted where the tensile twinning activity was increased to further understand the discrepancies between the experimental and predicted PFs. The resulting deformed PFs can be found in Figure 6.11, showing higher amounts of twinned grains, as shown by the higher intensity region in the centre of the predicted PFs. In the ND and ND45 cases, these additional twins change the predicted textures such that they are now comparable to the experimental PFs in Figure 6.10. This confirms the possibility of the experimental PFs being conducted closer to the fracture surface. Furthermore, the TD case remains relatively unchanged as there are very small amount of twins, as for this loading direction, the material deforms preferentially through slip [83].

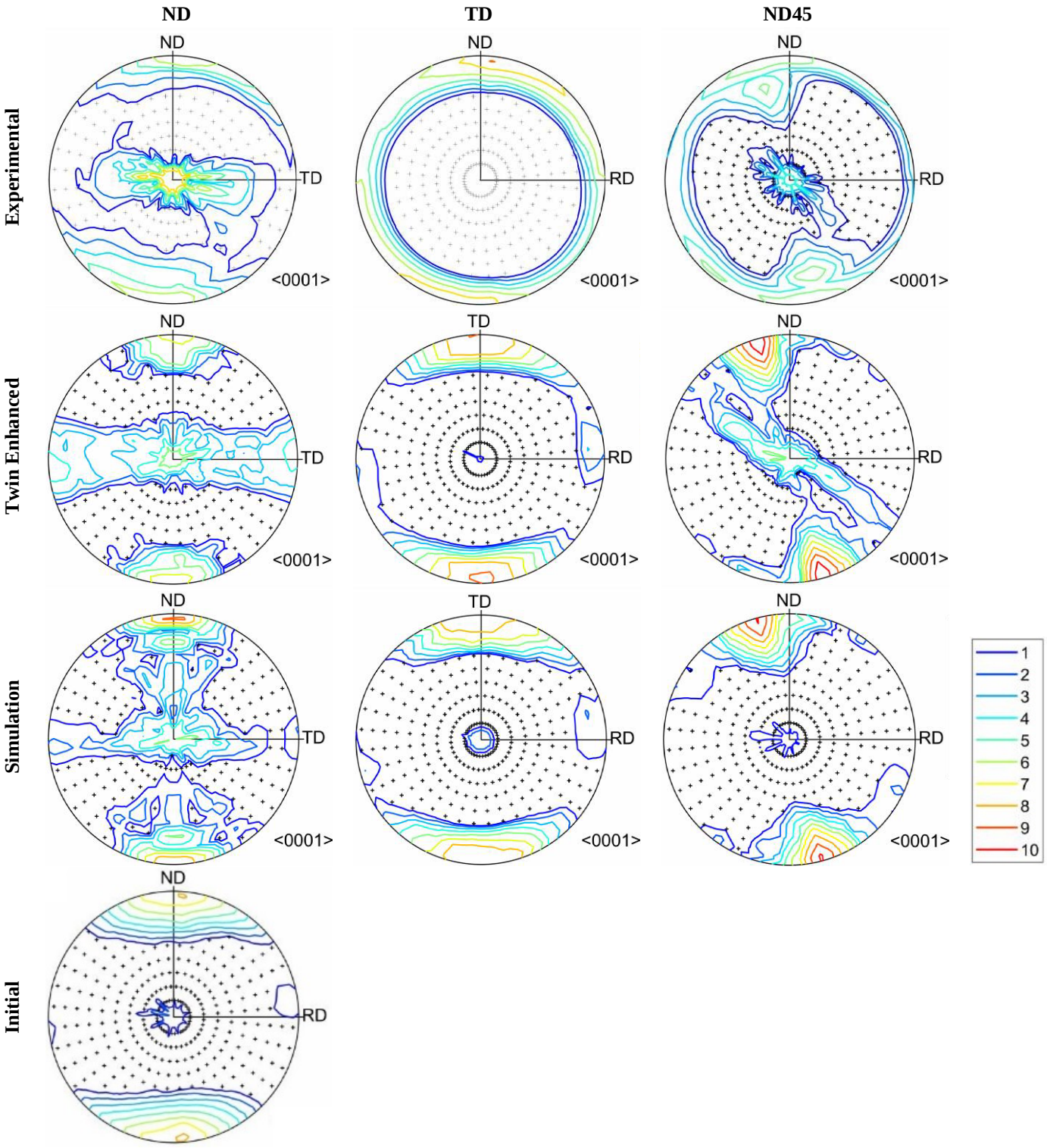

Figure 6.11 Experimental, tensile twin enhanced, and simulation (0001) pole figures at 200 °C at 18% strain in the ND, and 30% strain for TD and ND45. The initial pole figure is included for comparison.

6.5 DYNAMIC RECRYSTALLISATION BEHAVIOUR AND PARAMETRIC STUDIES

The DRX process is quite complex and different mechanisms can be activated, as such the model needs to take into consideration all these different aspects. A number of parametric studies were conducted to investigate the effects of the parameters used in the VPSC-DRX model, as well as to justify the values of the parameters that were used to run the simulations discussed in the previous sections.

6.5.1 Influence of the Dynamic Recrystallisation Thresholds

The main feature of this VPSC-DRX model is the introduction of thresholds to initiate and terminate the DRX behaviour during plastic deformation. This is accomplished via two terms called “initial threshold” and “final threshold”, which both uses a percentage of the parent grain’s volume fraction. A parametric study, shown in Figure 6.12, was conducted to investigate the effects of the threshold values on the DRX and the hardening behaviour. In Figure 6.12, the black lines show the original stress-strain curves that were presented and discussed in the previous sections. It should be noted that the final threshold was set to 100% of the parent grain’s volume fraction to accommodate the simulations runs with the larger initial thresholds. For the final threshold study, the initial threshold value was kept constant at 1% of the parent grain’s volume fraction.

When the initial threshold value decreases to 0.1% from 1% of the initial parent grain’s size (see the lighter colour curves in Figure 6.12), there is a small increase in the softening behaviour observed in the ND and ND45 cases. On the other hand, when the initial threshold increases to 15% and then 20% (see the darker colour curves in Figure 6.12), there is a reduction in the softening behaviour with the increase in the flow stress. These

effects are likely due to a delay in the activation of the DRX process; a smaller initial threshold value would allow an earlier activation of the DRX process, while a larger initial threshold value delays the activation of the DRX process.

Meanwhile in the TD case, there is only a minute difference in the softening behaviour whether the initial threshold increases or decreases. This difference is attributed to the higher amount of slip activity, as result of the anisotropic nature of Mg alloys (see Figure 6.6), which allows for a greater DRX growth rate (see Equation (5-7)). While the initial threshold is designed to delay the DRX process, however, due to the greater growth rate in the TD case, this delay is not seen.

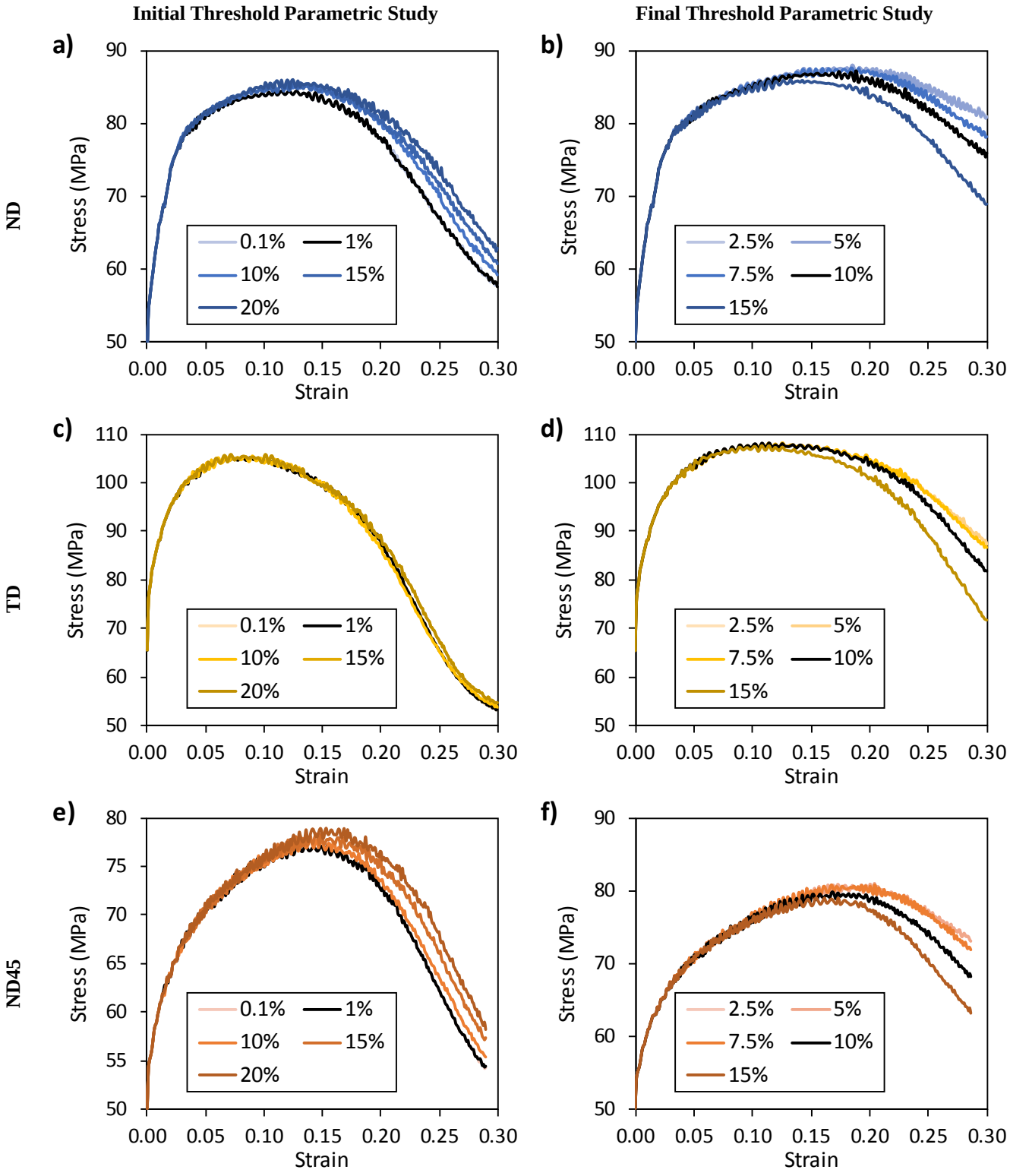

Figure 6.12 Stress-strain curves showing the influence of the initial and final threshold of parent grain's volume fraction for the three loading directions: (a, b) normal direction, (c, d) transverse direction, and (e, f) 45° from the normal direction. (a, c, and e) shows the effects of the initial threshold value, and (b, d, and f) show the effects of the final threshold value.

Another means to control the DRX mechanism is through the final threshold limit, which stops the DRX process of a grain, which was first implemented as a means to prevent material creation in the model. When this value is decreased to 2.5% (see the lighter colour curves in Figure 6.12), there is a reduction in the softening mechanism, due to the final threshold limiting the growth of the DRX grains, suppressing the DRX process. An increase of the final threshold to 15% of the parent grain (see the darker colour curves in Figure 6.12), results in a greater softening effect, which is a result of the continuation of the DRX mechanism to larger strains. Additionally, there are no distinct or notable differences between the results obtained for the different loading directions when changing the final thresholds.

6.5.2 Initial Dynamic Recrystallisation Grain Size

During the DRX process, the DRX grain size is initially in the nanoscale before the grains grow into larger grains. Through changing the initial nucleating grain size, it is possible to increase or decrease the effects DRX has on the flow stress as discussed in Section 6.5.1. Here a parametric study was done to elucidate the effects of the nucleating grain size on the DRX behaviour and mechanism (see Figure 6.13).

The original nucleating DRX grain size used in this study is 1 μm, and the effects of varying this initial size was tested over the range of 0.25 μm to 5 μm. When the nucleating DRX grain size is reduced to below 1 μm (see the lighter colour curves in Figure 6.13) the softening behaviour of the DRX is reduced, as seen by the decrease in the softening behaviour. Conversely, with a larger nucleating DRX grain size (see the darker colour curves in Figure 6.13), there is a larger softening behaviour due to DRX. Since the softening mechanism of Mg alloys is controlled by the volume fraction of the DRX grains,

any changes to the nucleating grain size will equate to a change in the DRX behaviour. Furthermore, the changes in the nucleating grain size results in a similar hardening behaviour in the different loading directions.

6.5.3 Influence of the Dynamic Recrystallisation Orientation

There are various types of DRX mechanisms that are active in Mg alloys, which affect the deformed texture in different manners. DDRX and CDRX both create new grains such that at the end of the deformation the grains will achieve a HAGB with respect to the parent grains, however the initial stages are very different. There are a variety of methods that have been used to predict the evolution of texture within DRX modelling. There are a few studies that utilise a randomised table of grains which are assigned to the newly formed DRX grains [15, 23-25, 83, 85], while other studies give the crystallographic orientation of the parent grain to the DRX grains [79, 107].

This VPSC-DRX model assigns new DRX grains a random crystallographic orientation with a misorientation angle of 15° relative to the parent grains. A parametric study was conducted to investigate the effect of the DRX grain crystallographic orientation on the mechanical behaviour and deformed texture. Here four different orientation assignment schemes were tested:

- DRX-Parent: DRX grains inherit the crystallographic orientation of the parent grains,
- DRX-RAND: DRX grains are rotated 15° around a random axis away from the parent grain crystallographic orientation,
- DRX-RAND15: same as DRX-RAND with a randomised rotation angle between 0 and 15°,
- DRX-RAND90: same as DRX-RAND with a randomised rotation angle between 0 and 90°.

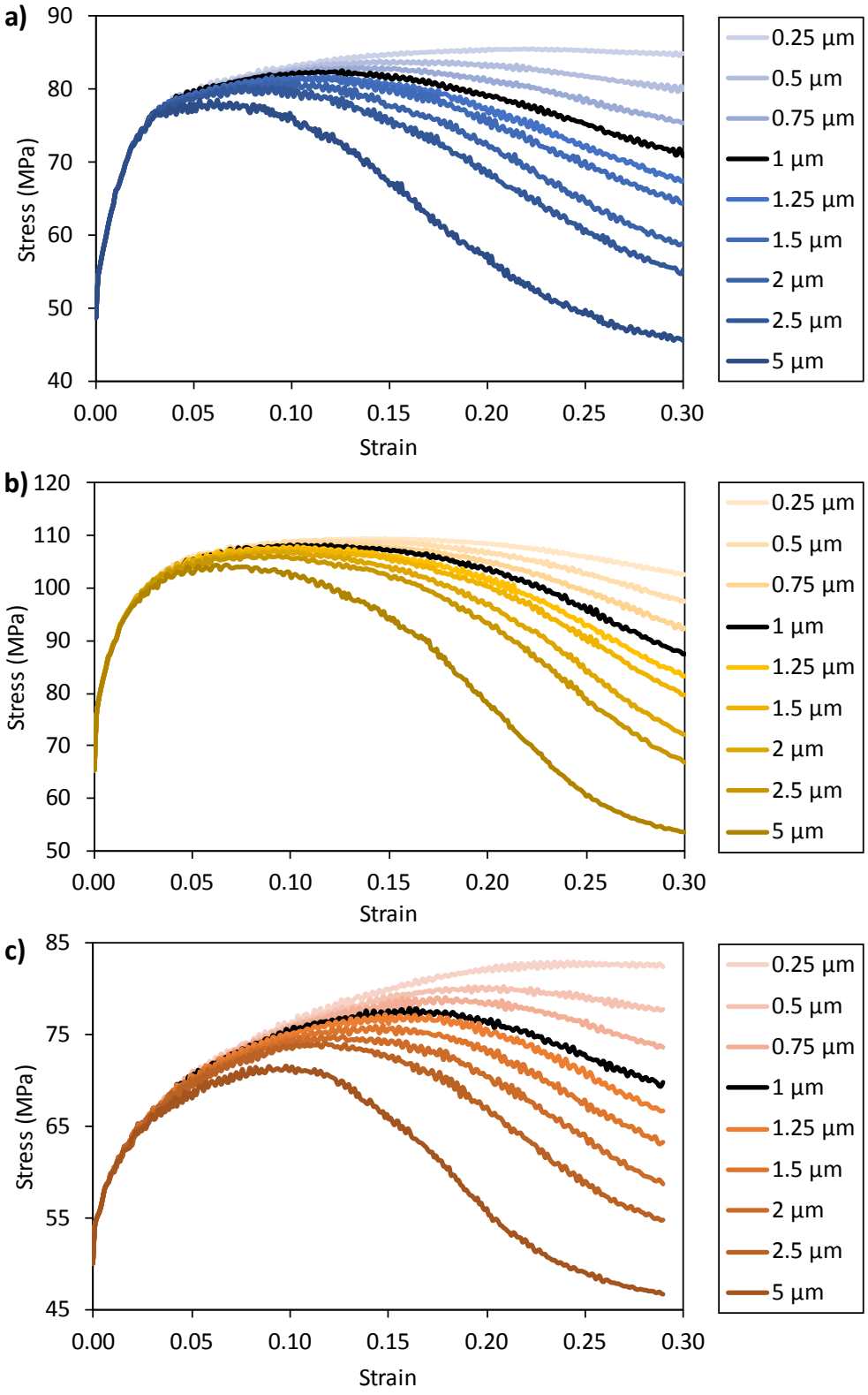

Figure 6.13 Stress-strain curves showing the influence of initial grain size on the stress-strain response when loaded in the: (a) normal direction, (b) tranverse direction, and (c) 45° from the normal direction.

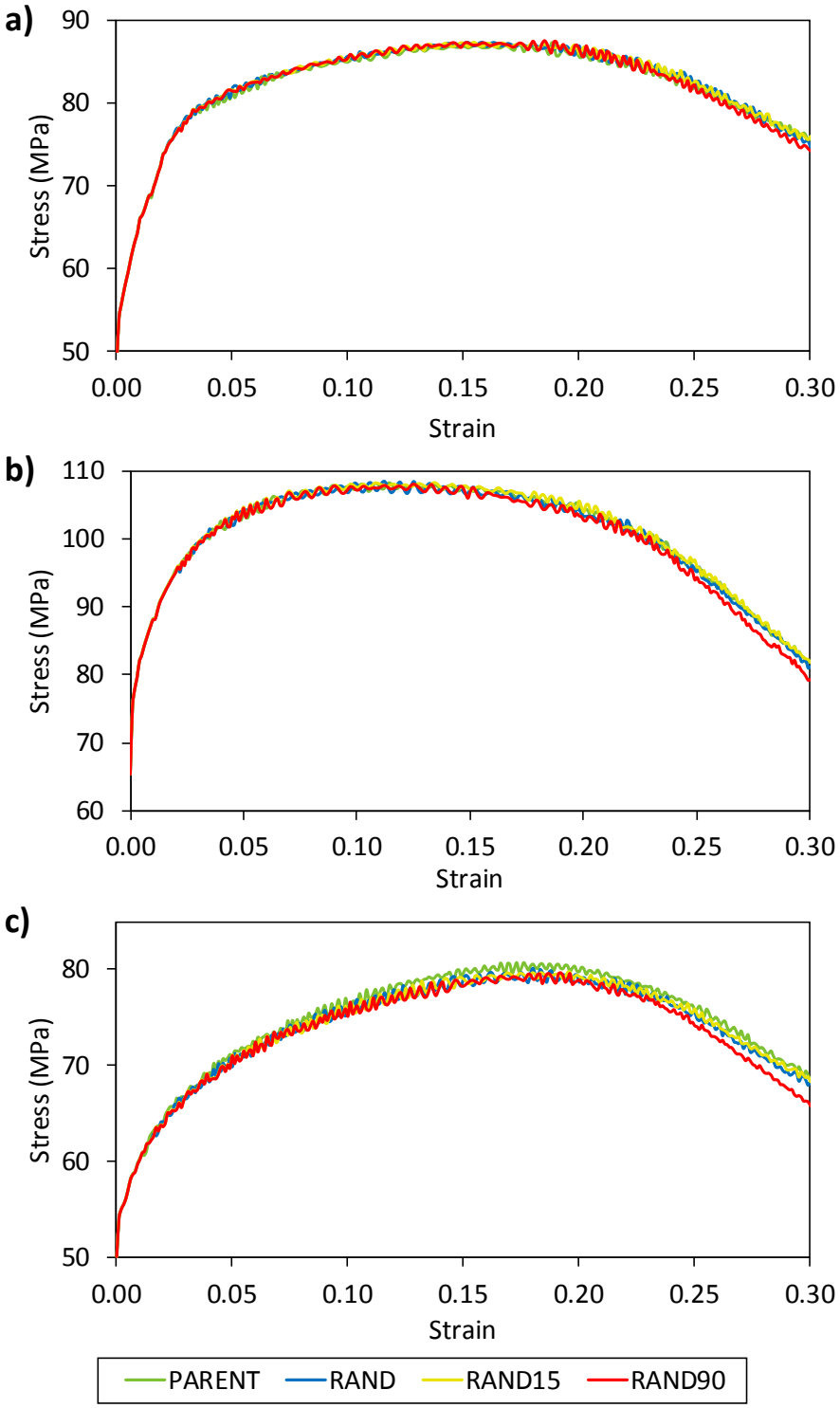

Figure 6.14 Stress-strain curves with different DRX orientation assignment schemes for the three loading directions: (a) normal direction, (b) transverse direction, and (c) 45° from the normal direction. The DRX-Parent orientation assignment scheme is in green, DRX-RAND in blue, DRX-RAND15 in yellow, and DRX-RAND90 in red.

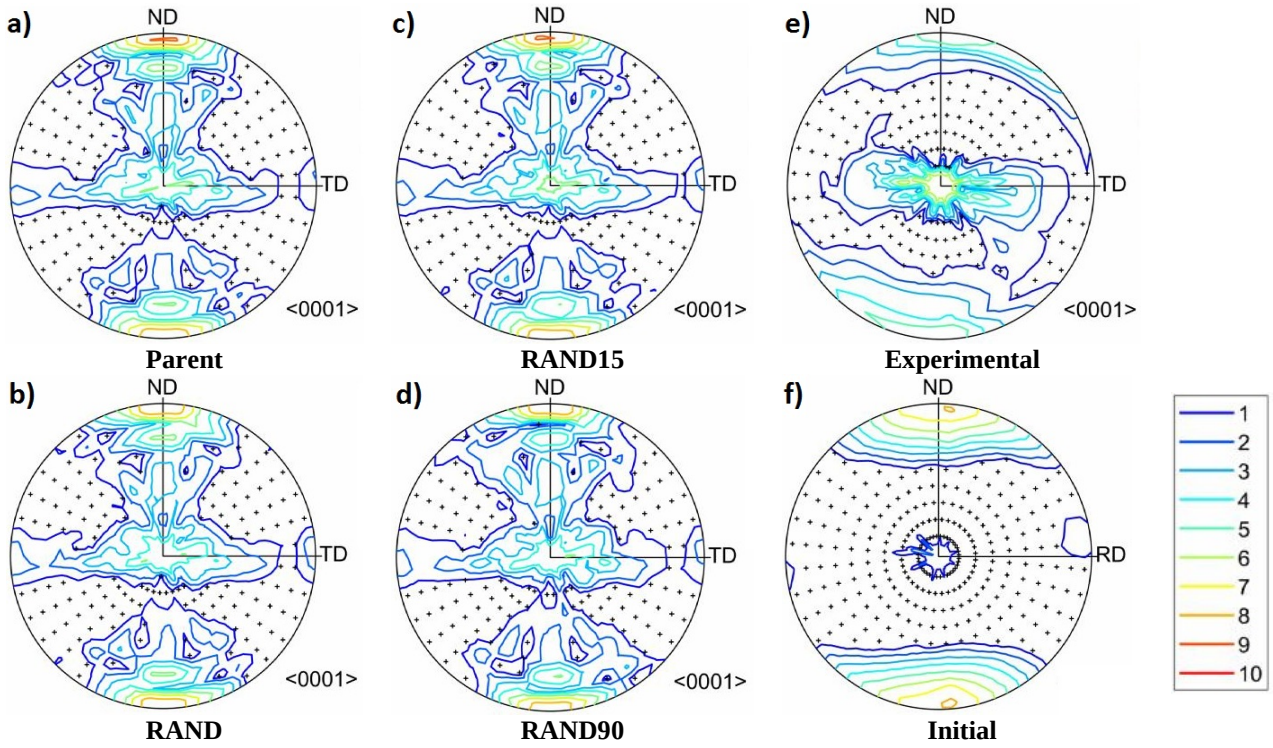

Figure 6.15 (0001) Pole figures for the ND loading direction for the different DRX orientation assignment schemes: (a) Parent, (b) RAND, (c) RAND15, (d) RAND90. The experimental (e) and initial (f) pole figures are included for comparison.

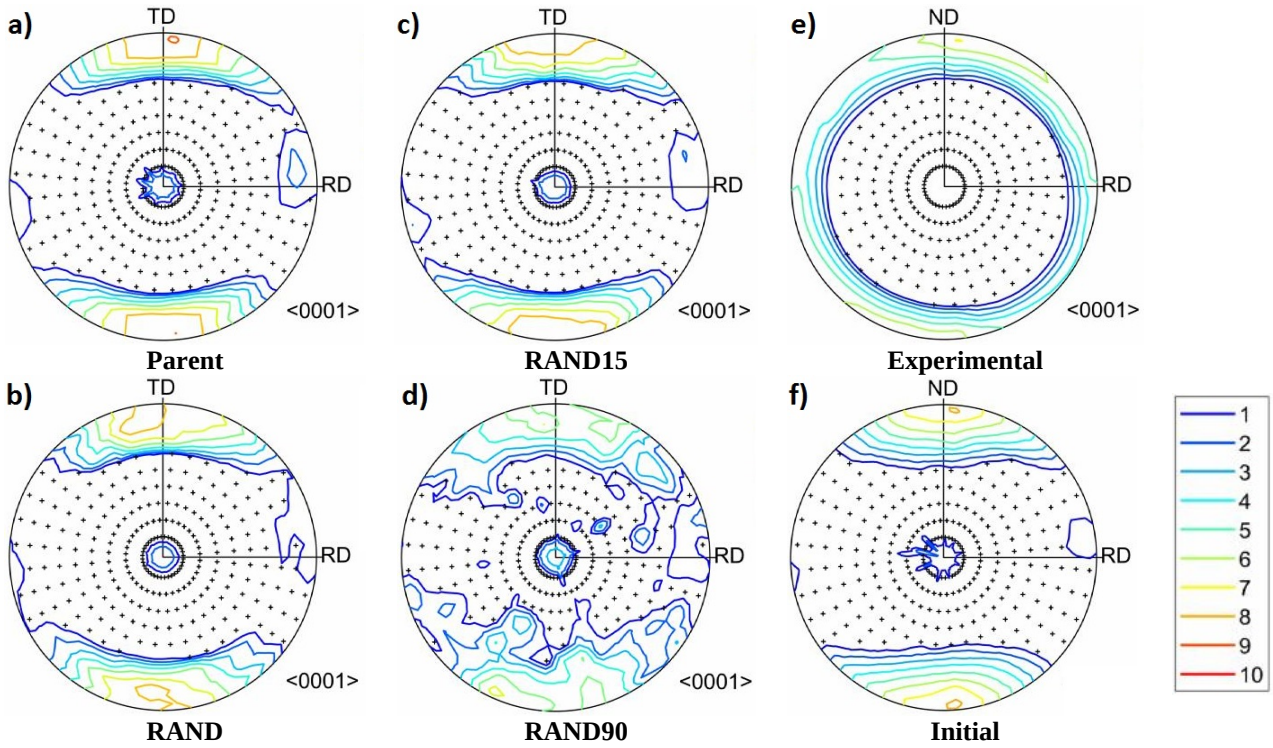

Figure 6.16 (0001) Pole figures for the TD loading direction for the different DRX orientation assignment schemes: (a) Parent, (b) RAND, (c) RAND15, (d) RAND90. The experimental (e) and initial (f) pole figures are included for comparison.

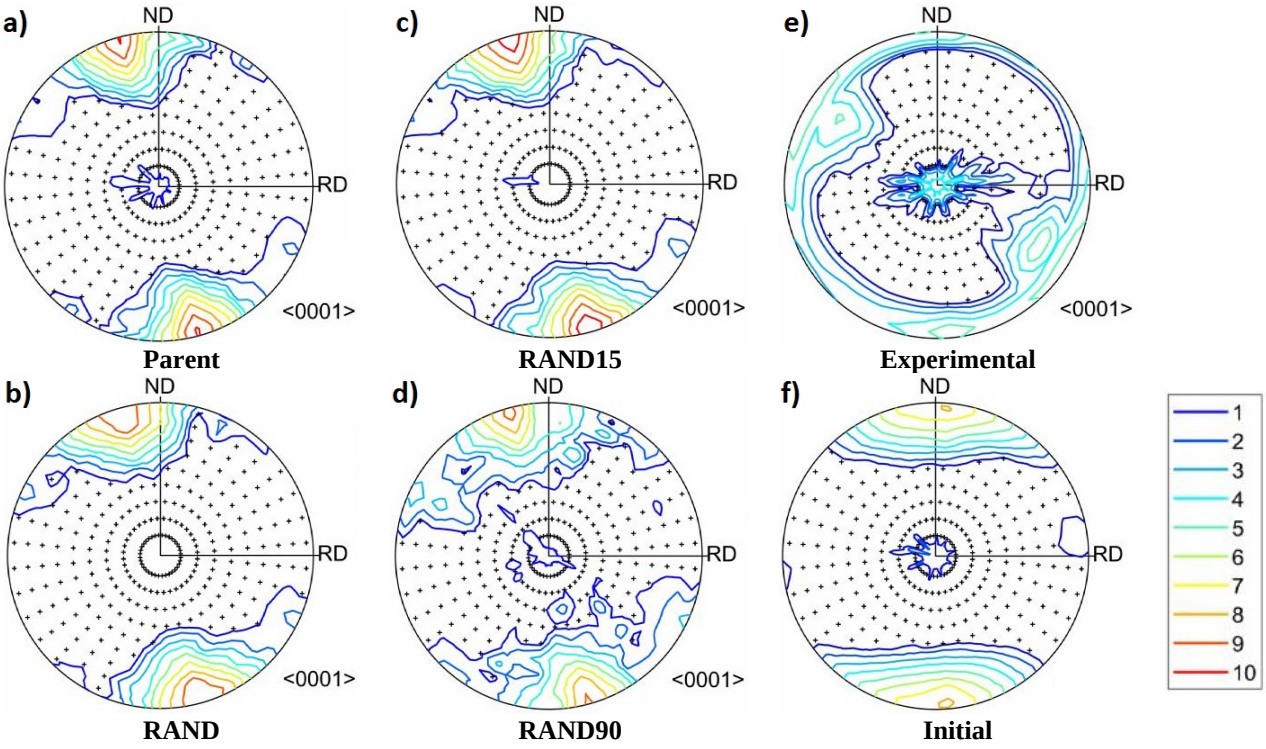

Figure 6.17 (0001) Pole figures for the ND45 loading direction for the different DRX orientation assignment schemes: (a) Parent, (b) RAND, (c) RAND15, (d) RAND90. The experimental (e) and initial (f) pole figures are included for comparison.

The resultant stress-strain curves for the different DRX orientation assignments schemes in Figure 6.14 show there are minute differences in the hardening behaviour between each of the orientation scheme. Ultimately, there are no significant differences to ascertain any importance of the orientation assignment scheme on the mechanical response [83, 89, 107].

Overall, the main difference between each orientation assignment scheme is the reduction in the main intensity regions in the PFs for the three loading directions, but in all cases the deformed (0001) PFs are similar (see Figure 6.15, Figure 6.16, and Figure 6.17 for the ND, ND45, and TD, respectively). For the ND45 and TD cases, the only scheme to produce a different texture is the DRX-RAND90 where a larger dispersion of the crystallographic orientation of grains can be seen in the larger intensity regions of Figure

6.16d and Figure 6.17d. This dispersion effect is prominent within the DDRX process, seen at higher temperature deformation (>300 °C) in Mg alloys, as the DRX grains are formed with HAGBs with respect to the parent grains [77]. Additionally, in the TD-RAND90 case, there is a stronger orthotropic effect that was also seen in the experimental PF (Figure 6.10). This suggests the deformed texture of the experimental is comprised of various DRX grains presenting various crystallographic orientations due to the CDRX mechanism of LAGBs rotating to HAGBs [74].

6.5.4 Influence of the Initial Dislocation Density of the Dynamic Recrystallisation Grains

A parametric study was done to see the effects of assigning a higher dislocation density to the newly formed DRX grains. The stress-strain curves obtained for different initial dislocation density values for the three loading directions are shown in Figure 6.18 with a range of initial DRX grain dislocation densities between $\rho = 1 \times 10^{10}\ m^{-2}$ and $1 \times 10^{14}\ m^{-2}$, where the darker lines indicate a larger dislocation density. The results presented in the previous section were obtained by using an initial dislocation density of $\rho = 1 \times 10^{4}\ m^{-2}$ assigned to newly formed DRX grains, and it is found that there are no drastic changes in the mechanical response until the initial DRX dislocation density reaches $\rho = 1 \times 10^{11}\ m^{-2}$. Increasing the initial dislocation density above $10^{11}\ m^{-2}$, noticeably increases the hardening after the peak stress; the same behaviour has been observed for the three loading directions tested in this study.

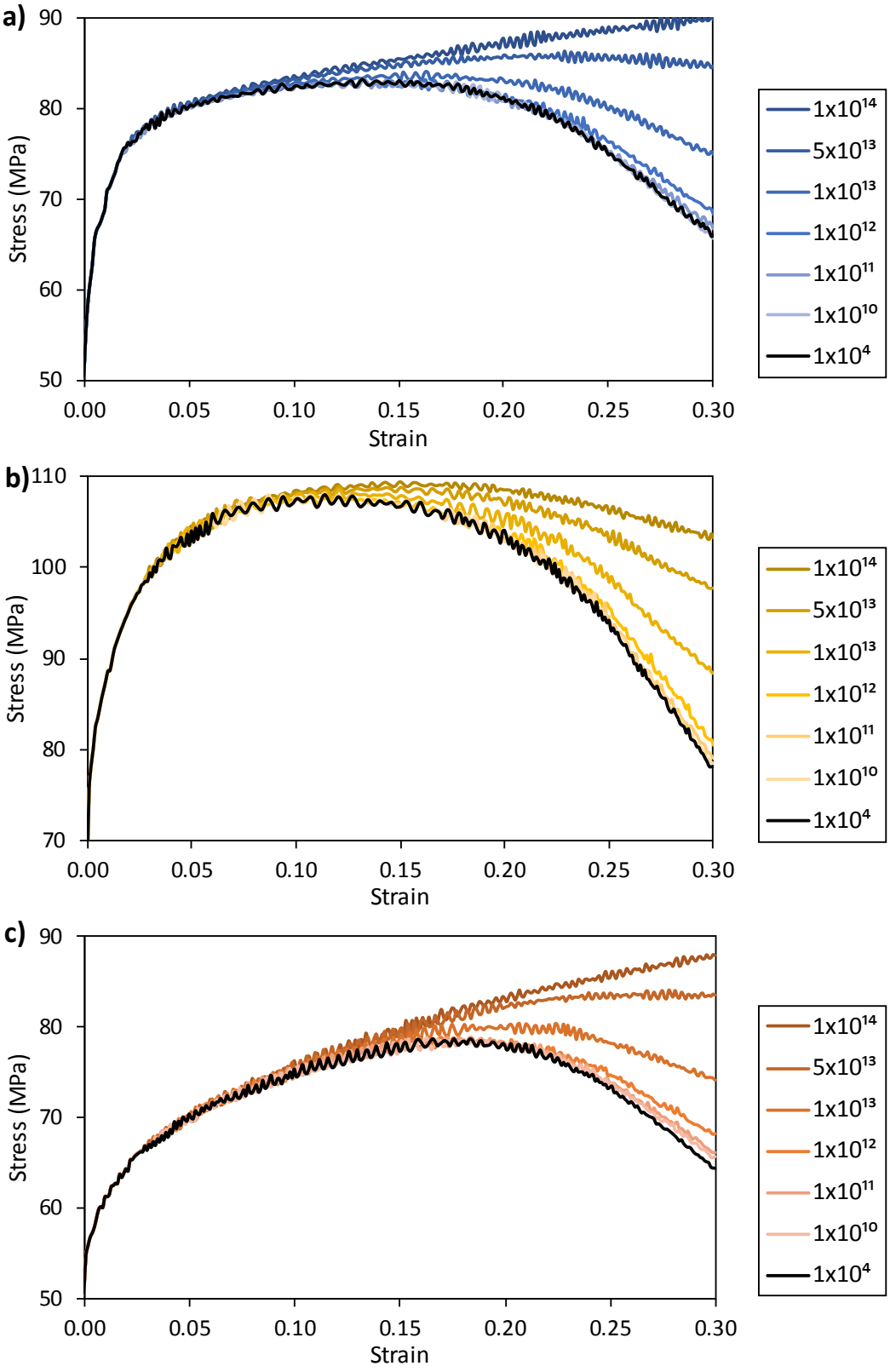

Figure 6.18 Stress-strain curves showing the influence of the initial dislocation density in the DRX grains on the three loading directions: (a) normal direction, (b) tranverse direction, and (c) 45° from the normal direction.

The DRX grain's dislocation density is used to calculate the growth of DRX grains, see Equation (5-7). When changing the initial dislocation density of the DRX grains, it correlates to a change in the DRX growth behaviour. As the dislocation density increases the driving force for the growth of DRX grains is expected to decrease altering the DRX behaviour, and consequently, the resulting steady state grain size of the DRX grains. With a nucleating DRX grain size of 1 μm and an initial dislocation density of $\rho = 1 \times 10^{10}\, m^{-2}$ and $1 \times 10^{14}\, m^{-2}$, results in a steady state DRX grain size of 1.285 μm and 1.475 μm, respectively. Therefore, while the nucleating DRX dislocation density plays a role in the mechanical behaviour and in the microstructural evolution of the DRX process, this can be avoided by selecting an appropriately small value.

6.5.5 Influence of the Number of Possible Dynamic Recrystallisation Grains formed in each Parent Grain

The DRX process has the ability to create an incredible number of grains and will do so until material failure. The current VPSC-DRX process puts a limit of seven DRX grains to be created per parent grain, as a means to reduce the computational load and time. A parametric study was conducted by differing the number of DRX grains per parent grain to illustrate the influence on the mechanical behaviour. The results of the parametric study are shown in Figure 6.19, where the black lines represent the original stress-strain curves of the results presented in the previous section. When restricting the DRX process to be able to only create one DRX grain, there is a great reduction of the softening effect when compared to the original curve. The decreased softening effect in the flow stress is due to the suppression of the DRX mechanism. As the DRX process is able to generate more grains, highlighted by the darker lines in Figure 6.19, the DRX mechanism is no longer suppressed allowing for larger drops in the flow stress for the three loading cases.

However, there are diminishing returns once the parent grain is allowed to create more than seven grains. When a grain is allowed to create 10,000 DRX grains there is no difference in the mechanical response in comparison to the results obtained by allowing the formation of only seven grains. This trend is present across all three loading directions. There was a noticeable increase in processing time when more DRX grains were nucleated. Therefore, the maximum number of DRX grains per parent grain in the simulations was set to seven, as a middle ground of processing speed and accuracy.

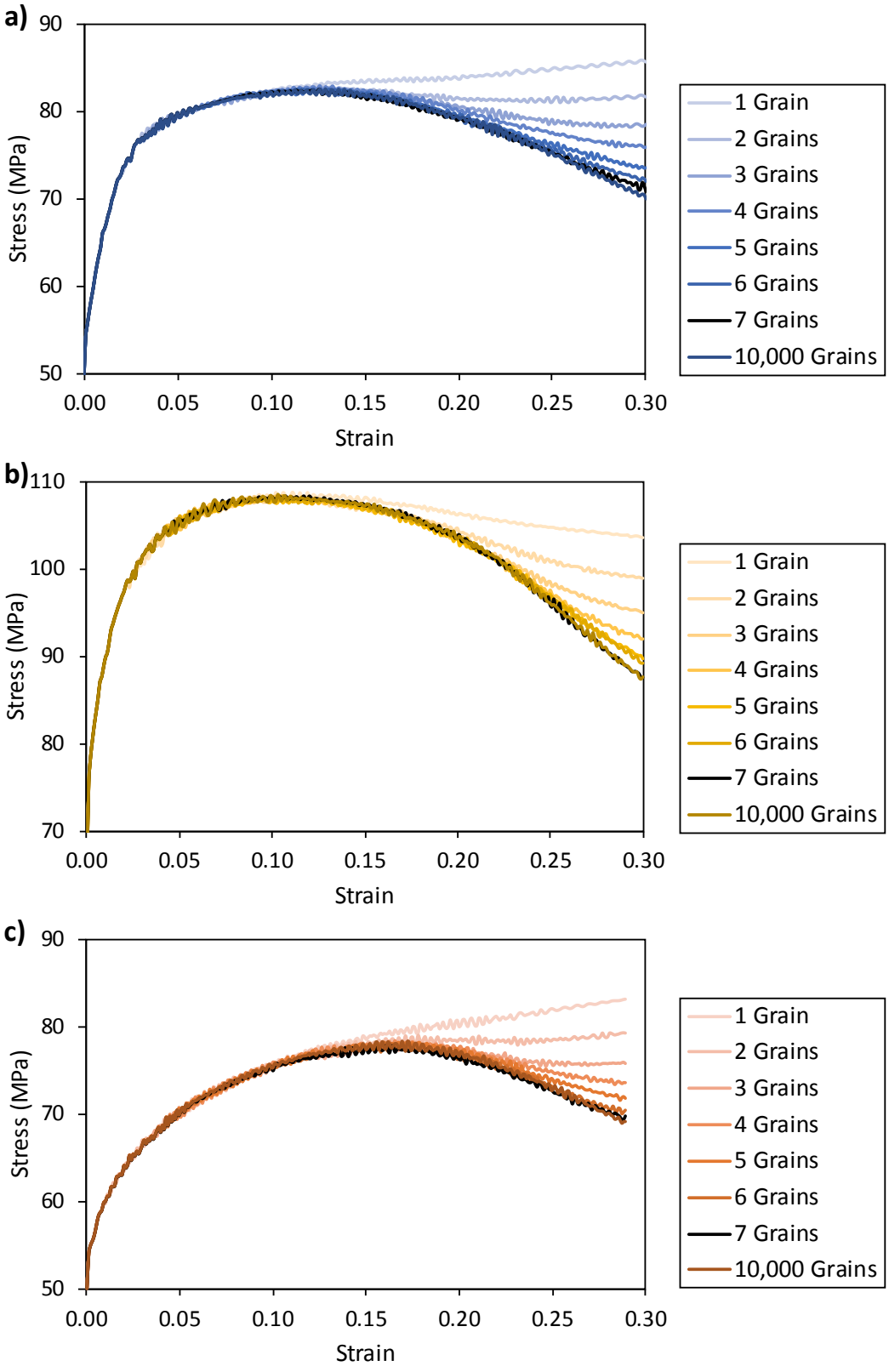

Figure 6.19 Stress-strain curves showing the influence of the number of DRX grains created in each parent grain on the three loading directions: (a) normal direction, (b) tranverse direction, and (c) 45° from the normal direction.

6.6 VPSC-DRX MODEL CONCLUSIONS

The VPSC-DRX model presented here adds a DRX scheme to the VPSC-T model described in Chapter 3. The VPSC-DRX model is able to predict the softening behaviour in the plastic deformation behaviour of the Mg alloy AZ31 at 200 °C under different loading directions. The temperature sensitive nature of the activation of the DRX mechanisms was captured with minimal amount of DRX predicted at 150 °C, and the lack of DRX at lower temperatures. The VPSC-DRX model is able to predict the hardening and softening behaviour and the textural evolution for each temperature and loading direction; the results are in close agreement with the experimental data reported in literature.

Chapter 7 | CONCLUSIONS

Magnesium and its alloys are a strong candidate to replace existing lightweight materials, such as aluminium and titanium with a lower energy and monetary cost, respectively. The main limitations of the widespread use of Mg alloys are the hot deformation necessary for processing Mg alloys (as a result of its low temperature formability), low operating temperatures, and its anisotropic behaviour. Through a simulation study realised by using previously published experimental data, the interplay between the various deformation mechanisms was analysed. This analysis can be used to understand the deformation behaviour of Mg alloys at low to warm temperatures during the manufacturing process and service life of that material.

The elevation of the deformation temperature from 25 °C to 200 °C in Mg and its alloys enables the material to be easily manufactured. Doing so, activates a variety of different deformation mechanisms: $\{10\bar{1}2\}$ tensile twinning, $\langle a\rangle$ basal slip, $\langle a\rangle$ prismatic slip, $\langle c+a\rangle$ pyramidal slip, and DRX. The VPSC model utilises a composite twin grain model as well as dislocation density hardening laws to determine the physical phenomena at play during plastic deformation. This simulation study resulted in the creation of two different VPSC models, which have been shown to accurately predict the activation of the deformation mechanisms under different loading conditions: a temperature sensitive model, and a second model incorporating the DRX scheme. These VPSC models use the same hardening law parameters to produce results in close agreement with experimental data, with regards to the hardening behaviour and microstructural evolution.

The temperature sensitive VPSC model, VPSC-T, was developed to incorporate the drag stresses and the dislocation-dislocation interaction matrix as temperature dependent

parameters. A comparative study was conducted in parallel to validate the proposed changes to the VPSC model, through the comparison of stress-strain responses and the resultant textures after plastic deformation. This study showed that the dislocation-dislocation interaction matrix is a material parameter, which plays a significant role in the strain hardening evolution. Utilising a temperature sensitive dislocation-dislocation interaction matrix instead of a constant one, resulted in predictions in a closer agreement with the experimental data, while the constant interaction matrix consistently overestimated the stress-strain response of the material to deformation. In addition, the drag stresses were shown to be crucial temperature sensitive parameters, necessary to accurately predict the mechanical behaviour. The drag stress for $\langle a \rangle$ prismatic slip is highly sensitive to temperature, while the drag stresses $\langle a \rangle$ basal slip and $\langle c + a \rangle$ pyramidal slip are almost temperature independent.

With increasing temperature, non-basal slip deformation mechanisms become increasingly active, causing a shift in the predominant deformation mode from $\{10\bar{1}2\}$ tensile twinning to $\langle c + a \rangle$ pyramidal slip at a temperature of 150 °C and above. If the loading direction is 45° offset from the c-axis, there are force components parallel and perpendicular to the c-axis and as such the deformation mechanisms will be a combination of the deformation modes observed when the loading direction is parallel or perpendicular to the c-axis. While the 45° offset from the c-axis loading direction maximises the Schmid factor for basal slip, additional deformations modes are necessary to accommodate plastic strain, and therefore, tensile twinning is activated at lower strains and prismatic slip at higher strains.

Deformation of AZ31 Mg at temperatures below 200 °C is possible under specific conditions; the loading direction needs to be favourable to preferentially activate non-basal slip and suppress the activation of twinning. The temperature during deformation needs to be high enough to allow for a switch from a twinning dominated deformation to a slip dominated deformation, which was observed to occur between 150 °C and 200 °C. Furthermore, DRX becomes active at 200 °C and plays a minor role in the strain accommodation.

The VPSC-T model reveals the inability to predict the softening behaviour as a result of DRX occurring at 200 °C and above. This lack of DRX softening spurred the development of the VPSC-DRX model. The VPSC-DRX model, developed upon the VPSC-T model, enables the prediction of the combination of twinning, slip, and DRX deformation mechanisms. The plastic behaviour predicted by the VPSC-DRX model is in agreement with the experimental data between 25 °C and 200 °C using a single set of hardening parameters. Additionally, a series of parametric studies were conducted to ascertain the effects of the various parameters used in this model.

The VPSC-DRX model uses a novel approach to simulate the DRX deformation mechanism by using an initial and final threshold values, representing a percentage of the parent initial grain size, to control the DRX behaviour. Increasing or decreasing the initial and final threshold values can accelerate, delay, or suppress DRX, respectively. The initial threshold value has minimal effects on the DRX induced mechanical response in the range of 0.1% to 10% of the parent initial grain size, however, when this value is increased to 15% or 20% DRX is delayed. The final threshold value has a great effect on the DRX induced softening response. The softening can be suppressed if the final

threshold value is low (2.5% to 7.5%) or accelerated when the final threshold value is increased to 15%.

In this new DRX scheme, the newly formed DRX grains are given a grain size, crystallographic orientation, and initial dislocation density, each having an influence on the DRX induced deformation behaviour. The nucleating grain size is able to suppress or accelerate DRX via decreasing or increasing the grain size, respectively. The initial dislocation density, used as the driving force for the growth of the DRX grains, plays a role in the softening mechanism induced by DRX in Mg alloys. The crystallographic orientation of the nucleated DRX grains has no effect on the mechanical behaviour and minor influences on the texture evolution. Furthermore, the number of grains that can be created during DRX process can affect the mechanical behaviour, however, there were diminishing returns when more than seven grains are created from each parent grain.

The implementation of the VPSC-DRX model into the VPSC-T model, enables the accurate prediction of the plastic deformation behaviour for the Mg alloy AZ31 at temperatures between 25 °C and 200 °C. The simulations are able to determine the switches in the predominant deformation mode as the temperature increases: twinning at room temperature, slip at elevated temperatures, and DRX begins to occur at 150 °C due to the increase in slip activity.

Chapter 8 | FUTURE STUDIES AND CONCEPTS

As it currently stands, the VPSC model developed in this study can be further improved through a deeper analysis of the deformation behaviour. In recent years, new complex processing techniques have been explored and developed for the manufacturing of Mg alloys, the robustness of the VPSC model should be tested for these new techniques. Furthermore, this study focuses the on the DRX behaviour at lower temperatures (≤200 °C), the robustness of the VPSC model can also be tested through simulations at higher temperatures (>250 °C).

8.1 ANISOTROPIC BEHAVIOUR

The attraction for the use of CP modelling is the ability to simulate any loading condition, which can account for the activation of multiple deformation mechanisms and predict the resulting material macroscopic response and microstructural evolution. It is also an important tool to help understand results of experimental work. Through modelling, studies can obtain a variety of data: hardening behaviour, microstructural evolution, and deformation activity, which can be used to describe the plastic behaviour. The temperature sensitive and DRX VPSC model was able to successfully predict the complex plastic behaviour over the temperature range of 25 °C to 200 °C, with the loading axis parallel, 45° offset, or perpendicular to the crystal's c-axis. This model could be tested to predict the deformation behaviour of the Mg alloy AZ31 under different conditions one would a detailed understanding of the deformation evolution from twin-dominated to slip-dominated plastic behaviour. Additional loading directions could be simulated to understand the transition between the twinning and slip dominated plastic behaviour.

Testing loading directions that are 15°, 30°, 60°, and 75°, could reveal a more complete picture of the anisotropic plastic behaviour evolution of that alloy.

8.2 SEVERE PLASTIC DEFORMATION FORMATION TECHNIQUES

A class of manufacturing processes known as severe plastic deformation (SPD) is commonly used to manufacture ultra-fine grained metals, and this has also been done on some Mg alloys [165, 166]. There are many different loading types and conditions, due to the large number of available SPD techniques, such as high-pressure torsion, repetitive corrugation and straightening, accumulative roll bonding, and equal channel angular extrusion [165-167]. These forming techniques, and resulting materials, have increased in popularity in the past decades, as these techniques have been able to improve the mechanical properties of coarse grained alloys. Additional testing with SPD techniques will be able to fully test the robustness of the models developed, evaluating the texture evolution and mechanical behaviour. In the case of ultra-fine grained material, new schemes might need to be incorporated in the VPSC model to describe other deformation mechanisms such as grain boundary sliding.

8.3 TEXTURE INFLUENCE

Currently the model is realised on a Mg alloy containing a strong basal texture in order to analyse the anisotropic deformation behaviour. Aside from hot rolling there are different forming techniques used to manufacture Mg alloys, such as extrusion/drawing, and SPD techniques as listed in Section 8.2. Each forming technique produces a different final texture. The model that was developed in this study could be used to predict the behaviour of theses alloys with different initial texture to gain an understanding of the effect of the initial on the plastic response of the alloy. This is important for warm

temperature deformation as there are a variety of different active deformations seen in Mg alloys.

8.4 Hot Deformation Behaviour and the Influence on the Dynamic Recrystallisation Mechanism

In industry, the manufacturing of Mg alloys occurs at elevated temperatures (>300 °C) to overcome the low temperature formability issues. It would be beneficial to test the robustness of the temperature sensitive and DRX VPSC models at higher temperatures, i.e. 250 °C, 300 °C, and 350 °C. It would be interesting to see how the DRX model developed in this study handle the deformation behaviour with larger amounts of recrystallisation.

8.5 General Model Improvements

The current model uses a minimum and maximum threshold as a percentage of the parent grains' size to control the DRX grain nucleation and growth behaviour. The initial version of the DRX model was to be made for this particular case and does not simulate the DRX behaviour in larger and smaller initial grain sizes. For larger initial grain sizes there will be a smaller number of DRX grains than expected and for smaller initial grain sizes using the percentages will produce very fine DRX grains. Both of these scenarios do not reflect the physical nature of the DRX behaviour, as such an adaptive method of defining the thresholds is needed. Additionally, further experimental studies into the DRX volume fractions at various strains could be conducted to ascertain the validity of the DRX model.

REFERENCES

1. Mordike, B.L. and T. Ebert, *Magnesium - Properties - applications - potential.* Materials Science and Engineering a-Structural Materials Properties Microstructure and Processing, 2001. **302**(1): p. 37-45.

2. Ward-Close, C. and F. Froes, *Developments in the synthesis of lightweight metals.* JOM, 1994. **46**(1): p. 28-31.

3. Hirsch, J. and T. Al-Samman, *Superior light metals by texture engineering: Optimized aluminum and magnesium alloys for automotive applications.* Acta Materialia, 2013. **61**(3): p. 818-843.

4. Kring, D.A. *Composition of Earth's continental crust as inferred from the compositions of impact melt sheets*. in *Lunar and Planetary Science Conference*. 1997.

5. Gunn, G., *Critical metals handbook.* 2014: John Wiley & Sons.

6. Agarwal, S., et al., *Biodegradable magnesium alloys for orthopaedic applications: A review on corrosion, biocompatibility and surface modifications.* Materials Science and Engineering: C, 2016. **68**: p. 948-963.

7. Dogan, E., et al., *Role of starting texture and deformation modes on low-temperature shear formability and shear localization of Mg–3Al–1Zn alloy.* Acta Materialia, 2015. **89**: p. 408-422.

8. Vaughan, M., et al., *Interplay between the effects of deformation mechanisms and dynamic recrystallization on the failure of Mg-3Al-1Zn.* Acta Materialia, 2019. **168**: p. 448-472.

9. Tam, K.J., et al., *Modelling the temperature and texture effects on the deformation mechanisms of magnesium alloy AZ31*. International Journal of Mechanical Sciences, 2020. **182**: p. 105727.

10. Al-Samman, T., *Comparative study of the deformation behavior of hexagonal magnesium–lithium alloys and a conventional magnesium AZ31 alloy.* Acta Materialia, 2009. **57**(7): p. 2229-2242.

11. Li, X., et al., *Texture and microstructure development during hot deformation of ME20 magnesium alloy: Experiments and simulations.* Materials Science and Engineering: A, 2011. **528**(27): p. 7915-7925.

12. Wang, M., et al., *Effect of initial texture on dynamic recrystallization of AZ31 Mg alloy during hot rolling.* Materials Science and Engineering: A, 2011. **528**(6): p. 2941-2951.

13. Proust, G., C. Tomé, and G. Kaschner, *Modeling texture, twinning and hardening evolution during deformation of hexagonal materials.* Acta Materialia, 2007. **55**(6): p. 2137-2148.

14. Beyerlein, I. and C. Tomé, *A dislocation-based constitutive law for pure Zr including temperature effects.* International Journal of Plasticity, 2008. **24**(5): p. 867-895.

15. Zhou, G., et al., *Misorientation Development in Continuous Dynamic Recrystallization of AZ31B Alloy Sheet and Polycrystal Plasticity Simulation.* Materials Science and Engineering: A, 2018.

16. Proust, G., et al., *Modeling the effect of twinning and detwinning during strain-path changes of magnesium alloy AZ31.* International Journal of Plasticity, 2009. **25**(5): p. 861-880.

17. Chandola, N., R.K. Mishra, and O. Cazacu, *Application of the VPSC Model to the Description of the Stress–Strain Response and Texture Evolution in AZ31 Mg for Various Strain Paths.* Journal of Engineering Materials and Technology, 2015. **137**(4): p. 041007.

18. Li, L., et al., *Effects of strain rate on the microstructure evolution and mechanical response of magnesium alloy AZ31.* Materials Science and Engineering: A, 2017. **684**: p. 37-46.

19. Agnew, S.R. and Ö. Duygulu, *Plastic anisotropy and the role of non-basal slip in magnesium alloy AZ31B.* International Journal of plasticity, 2005. **21**(6): p. 1161-1193.

20. Barnett, M.R., C.H.J. Davies, and X. Ma, *An analytical constitutive law for twinning dominated flow in magnesium.* Scripta materialia, 2005. **52**(7): p. 627-632.

21. Oppedal, A., et al., *Effect of dislocation transmutation on modeling hardening mechanisms by twinning in magnesium.* International Journal of Plasticity, 2012. **30**: p. 41-61.

22. Oppedal, A., et al., *Anisotropy in hexagonal close-packed structures: improvements to crystal plasticity approaches applied to magnesium alloy.* Philosophical Magazine, 2013. **93**(35): p. 4311-4330.

23. Ding, R. and Z.X. Guo, *Coupled quantitative simulation of microstructural evolution and plastic flow during dynamic recrystallization.* Acta materialia, 2001. **49**(16): p. 3163-3175.

24. Tang, T., et al., *A polycrystal plasticity based thermo-mechanical-dynamic recrystallization coupled modeling method and its application to light weight alloys.* International Journal of Plasticity, 2019. **116**: p. 159-191.

25. Zecevic, M., et al., *Modelling recrystallization textures driven by intragranular fluctuations implemented in the viscoplastic self-consistent formulation.* Acta Materialia, 2019. **164**: p. 530-546.

26. Proust, G., *Processing magnesium at room temperature.* Science, 2019. **365**(6448): p. 30-31.

27. Xu, W., et al., *A high-specific-strength and corrosion-resistant magnesium alloy.* Nature Materials, 2015. **14**(12): p. 1229-1235.

28. Chakkedath, A., et al., *Contraction Twinning Dominated Tensile Deformation and Subsequent Fracture in Extruded Mg-1Mn (Wt Pct) at Ambient Temperature.* Metallurgical and Materials Transactions A, 2018: p. 1-14.

29. Risse, M., et al., *Elevated temperature effects on the plastic anisotropy of an extruded Mg-4 Wt Pct Li alloy: experiments and polycrystal modeling.* Metallurgical and Materials Transactions A, 2017. **48**(1): p. 446-458.

30. Beer, A.G. and M.R. Barnett, *Microstructural Development during Hot Working of Mg-3Al-1Zn.* Metallurgical and Materials Transactions A, 2007. **38**(8): p. 1856-1867.

31. Khosravani, A., et al., *Twinning in magnesium alloy AZ31B under different strain paths at moderately elevated temperatures.* International Journal of Plasticity, 2013. **45**: p. 160-173.

32. Ziaei, S. and M. Zikry, *Modeling the effects of dislocation–density interaction, generation, and recovery on the behavior of HCP materials.* Metallurgical and Materials Transactions A, 2015. **46**(10): p. 4478-4490.

33. Gu, X., et al., *In vitro corrosion and biocompatibility of binary magnesium alloys.* Biomaterials, 2009. **30**(4): p. 484-498.

34. Staiger, M.P., et al., *Magnesium and its alloys as orthopedic biomaterials: a review.* Biomaterials, 2006. **27**(9): p. 1728-1734.

35. Ding, Y., et al., *Effects of alloying elements on the corrosion behavior and biocompatibility of biodegradable magnesium alloys: a review.* Journal of materials chemistry B, 2014. **2**(14): p. 1912-1933.

36. Henderson, S.E., et al., *Magnesium alloys as a biomaterial for degradable craniofacial screws.* Acta biomaterialia, 2014. **10**(5): p. 2323-2332.

37. Gu, X.-N. and Y.-F. Zheng, *A review on magnesium alloys as biodegradable materials.* Frontiers of Materials Science in China, 2010. **4**(2): p. 111-115.

38. Luthringer, B.J., F. Feyerabend, and R. Willumeit-Römer, *Magnesium-based implants: a mini-review*. Magnesium research, 2014. **27**(4): p. 142-154.

39. Khan, A.S., et al., *Mechanical response and texture evolution of AZ31 alloy at large strains for different strain rates and temperatures.* International Journal of Plasticity, 2011. **27**(5): p. 688-706.

40. Staroselsky, A. and L. Anand, *A constitutive model for hcp materials deforming by slip and twinning: application to magnesium alloy AZ31B.* International journal of Plasticity, 2003. **19**(10): p. 1843-1864.

41. Balík, J., et al., *Modeling of the work hardening in magnesium alloy sheets.* International Journal of Plasticity, 2016. **76**: p. 166-185.

42. Li, Z., et al. *A crystal plasticity study on the deformation of an AZ31 alloy sheet under elevated temperature*. in *Journal of Physics: Conference Series*. 2018. IOP Publishing.

43. Al-Samman, T., X. Li, and S.G. Chowdhury, *Orientation dependent slip and twinning during compression and tension of strongly textured magnesium AZ31 alloy.* Materials Science and Engineering: A, 2010. **527**(15): p. 3450-3463.

44. Xie, Q., et al., *Crystal plasticity-based impact dynamic constitutive model of magnesium alloy.* International Journal of Mechanical Sciences, 2016. **119**: p. 107-113.

45. Abedini, A., et al., *Constitutive characterization of a rare-earth magnesium alloy sheet (ZEK100-O) in shear loading: Studies of anisotropy and rate sensitivity.* International Journal of Mechanical Sciences, 2017. **128-129**: p. 54-69.

46. Qi, H.G., et al., *Atomistic simulation of the structural evolution in magnesium single crystal under c-axis tension.* Acta Metallurgica Sinica-English Letters, 2011. **24**(6): p. 487-494.

47. Ardeljan, M., et al., *Strain rate and temperature sensitive multi-level crystal plasticity model for large plastic deformation behavior: Application to AZ31 magnesium alloy.* International Journal of Plasticity, 2016. **83**: p. 90-109.

48. Koh, Y., et al., *Characterization of mechanical property of magnesium AZ31 alloy sheets for warm temperature forming.* International Journal of Mechanical Sciences, 2015. **93**: p. 204-217.

49. Callister, W.D. and D.G. Rethwisch, *Materials science and engineering: an introduction*. 2018: Wiley New York.

50. Bertin, N., et al., *On the strength of dislocation interactions and their effect on latent hardening in pure magnesium.* International Journal of Plasticity, 2014. **62**: p. 72-92.

51. Nave, M.D. and M.R. Barnett, *Microstructures and textures of pure magnesium deformed in plane-strain compression.* Scripta Materialia, 2004. **51**(9): p. 881-885.

52. Wang, H., et al., *In-situ analysis of the tensile deformation modes and anisotropy of extruded Mg-10Gd-3Y-0.5 Zr (wt.%) at elevated temperatures.* International Journal of Plasticity, 2016. **84**: p. 255-276.

53. Taylor, G.I., *Plastic strain in metals.* Journal of the Institute of Metals, 1938. **62**: p. 307-324.

54. Abedini, A., et al., *Constitutive characterization of a rare-earth magnesium alloy sheet (ZEK100-O) in shear loading: Studies of anisotropy and rate sensitivity.* International Journal of Mechanical Sciences, 2017. **128**: p. 54-69.

55. Koike, J., *Enhanced deformation mechanisms by anisotropic plasticity in polycrystalline Mg alloys at room temperature.* Metallurgical and Materials Transactions a-Physical Metallurgy and Materials Science, 2005. **36a**(7): p. 1689-1696.

56. Knezevic, M., et al., *Strain rate and temperature effects on the selection of primary and secondary slip and twinning systems in HCP Zr.* Acta Materialia, 2015. **88**: p. 55-73.

57. Lavrentev, F.F. and Y.A. Pokhil, *Relation of Dislocation Density in Different Slip Systems to Work-Hardening Parameters for Magnesium Crystals.* Materials Science and Engineering, 1975. **18**(2): p. 261-270.

58. Popova, E., et al., *Coupled crystal plasticity–Probabilistic cellular automata approach to model dynamic recrystallization in magnesium alloys.* International Journal of Plasticity, 2015. **66**: p. 85-102.

59. Tadano, Y., *Formability of magnesium sheet with rolling texture.* International Journal of Mechanical Sciences, 2016. **108-109**: p. 72-82.

60. Zecevic, M., I.J. Beyerlein, and M. Knezevic, *Activity of pyramidal I and II< c+ a> slip in Mg alloys as revealed by texture development.* Journal of the Mechanics and Physics of Solids, 2018. **111**: p. 290-307.

61. Wang, Q., et al., *Anisotropic fracture behavior of AZ31 magnesium alloy sheets as a function of the stress state and temperature.* International Journal of Mechanical Sciences, 2019. **163**: p. 105146.

62. Koh, Y., et al., *Characterization of mechanical property of magnesium AZ31 alloy sheets for warm temperature forming.* International Journal of Mechanical Sciences, 2015. **93**: p. 204-217.

63. Wang, Q.L., et al., *Anisotropic fracture behavior of AZ31 magnesium alloy sheets as a function of the stress state and temperature.* International Journal of Mechanical Sciences, 2019. **163**: p. 105146.

64. *Chapter 8 - Dislocation Climb*, in *Pergamon Materials Series*, D. Caillard and J.L. Martin, Editors. 2003, Pergamon. p. 281-319.

65. *22 - Creep of aerospace materials*, in *Introduction to Aerospace Materials*, A.P. Mouritz, Editor. 2012, Woodhead Publishing. p. 521-533.

66. *3 - Dislocation Motion at Elevated Temperatures*, in *High Temperature Deformation and Fracture of Materials*, J.-S. Zhang, Editor. 2010, Woodhead Publishing. p. 28-39.

67. Viguier, B., et al., *Modelling the flow stress anomaly in γ-TiAl I. Experimental observations of dislocation mechanisms.* Philosophical Magazine A, 1995. **71**(6): p. 1295-1312.

68. Dorn, J.E. and J.B. Mitchell, *Slip mechanisms in single crystals of hexagonal close-packed phases.* 1964.

69. Galiyev, A., R. Kaibyshev, and G. Gottstein, *Correlation of plastic deformation and dynamic recrystallization in magnesium alloy ZK60.* Acta Materialia, 2001. **49**(7): p. 1199-1207.

70. Mirzadeh, H., et al., *Rate controlling mechanisms during hot deformation of Mg–3Gd–1Zn magnesium alloy: dislocation glide and climb, dynamic recrystallization, and mechanical twinning.* Materials & Design, 2015. **68**: p. 228-231.

71. Oren, E., E. Yahel, and G. Makov, *Kinetics of dislocation cross-slip: A molecular dynamics study.* Computational Materials Science, 2017. **138**: p. 246-254.

72. Milička, K., J. Čadek, and P. Ryš, *High temperature creep mechanisms in magnesium.* Acta Metallurgica, 1970. **18**(10): p. 1071-1082.

73. Wu, Z. and W.A. Curtin, *Mechanism and energetics of ⟨c + a⟩ dislocation cross-slip in hcp metals.* Proceedings of the National Academy of Sciences, 2016. **113**(40): p. 11137.

74. Huang, K. and R. Logé, *A review of dynamic recrystallization phenomena in metallic materials.* Materials & Design, 2016. **111**: p. 548-574.

75. Popova, E., et al., *Effect of extension 101-2 twins on texture evolution at elevated temperature deformation accompanied by dynamic recrystallization.* Materials & Design, 2016. **96**: p. 446-457.

76. Farzadfar, S., et al., *Role of yttrium in the microstructure and texture evolution of Mg.* Materials Science and Engineering: A, 2011. **528**(22-23): p. 6742-6753.

77. Li, L., *Deformation band and texture of a cast Mg–RE alloy under uniaxial hot compression.* Materials Science and Engineering: A, 2011. **528**(24): p. 7178-7185.

78. Al-Samman, T. and G. Gottstein, *Dynamic recrystallization during high temperature deformation of magnesium.* Materials Science and Engineering: A, 2008. **490**(1-2): p. 411-420.

79. Griffiths, D., *Explaining texture weakening and improved formability in magnesium rare earth alloys.* Materials Science and Technology, 2015. **31**(1): p. 10-24.

80. Liu, J., Z. Cui, and L. Ruan, *A new kinetics model of dynamic recrystallization for magnesium alloy AZ31B.* Materials Science and Engineering: A, 2011. **529**: p. 300-310.

81. Zhang, H., et al., *Improved mechanical properties of AZ31 magnesium alloy plates by pre-rolling followed by warm compression.* Materials Science and Engineering: A, 2014. **618**: p. 540-545.

82. Galiyev, A., R. Kaibyshev, and T. Sakai, *Continuous Dynamic Recrystallization in Magnesium Alloy.* 2003.

83. Zhou, G., et al., *A polycrystal plasticity based discontinuous dynamic recrystallization simulation method and its application to copper.* International Journal of Plasticity, 2017. **91**: p. 48-76.

84. Liu, J., Z.-s. Cui, and L.-q. Ruan, *A new kinetics model of dynamic recrystallization for magnesium alloy AZ31B.* Materials Science and Engineering: A, 2011. **529**: p. 300-310.

85. Chen, M.-S., et al., *Modeling and simulation of dynamic recrystallization behaviors of magnesium alloy AZ31B using cellular automaton method.* Computational Materials Science, 2017. **136**: p. 163-172.

86. Changizian, P., A. Zarei-Hanzaki, and H. Abedi, *On the recrystallization behavior of homogenized AZ81 magnesium alloy: The effect of mechanical twins and γ precipitates.* Materials Science and Engineering: A, 2012. **558**: p. 44-51.

87. Fatemi-Varzaneh, S., A. Zarei-Hanzaki, and H. Beladi, *Dynamic recrystallization in AZ31 magnesium alloy.* Materials Science and Engineering: A, 2007. **456**(1-2): p. 52-57.

88. Spigarelli, S., et al., *Analysis of high-temperature deformation and microstructure of an AZ31 magnesium alloy.* Materials Science and Engineering: A, 2007. **462**(1-2): p. 197-201.

89. Fan, X.G., et al., *Quantitative analysis of dynamic recrystallization behavior using a grain boundary evolution based kinetic model.* Materials Science and Engineering: A, 2010. **527**(21-22): p. 5368-5377.

90. Chen, X.-M., et al., *Dynamic recrystallization behavior of a typical nickel-based superalloy during hot deformation.* Materials & Design, 2014. **57**: p. 568-577.

91. Sitdikov, O. and R. Kaibyshev, *Dynamic recrystallization in pure magnesium.* Materials Transactions, 2001. **42**(9): p. 1928-1937.

92. Wang, Y., et al., *Modeling and application of constitutive model considering the compensation of strain during hot deformation.* Journal of Alloys and Compounds, 2016. **681**: p. 455-470.

93. Fatemi-Varzaneh, S.M., et al., *EBSD characterization of repetitive grain refinement in AZ31 magnesium alloy.* Materials Chemistry and Physics, 2015. **149**: p. 339-343.

94. Ma, Q., et al., *Twinning-induced dynamic recrystallization in a magnesium alloy extruded at 450 C.* Scripta Materialia, 2011. **65**(9): p. 823-826.

95. Cizek, P. and B. Wynne, *A mechanism of ferrite softening in a duplex stainless steel deformed in hot torsion.* Materials Science and Engineering: A, 1997. **230**(1-2): p. 88-94.

96. Ueji, R., et al., *Tensile properties and twinning behavior of high manganese austenitic steel with fine-grained structure.* Scripta Materialia, 2008. **59**(9): p. 963-966.

97. Prasad, Y. and N. Ravichandran, *Effect of stacking fault energy on the dynamic recrystallization during hot working of FCC metals: A study using processing maps.* Bulletin of Materials Science, 1991. **14**(5): p. 1241-1248.

98. Chang, C., X.H. Du, and J.C. Huang, *Producing nanograined microstructure in Mg–Al–Zn alloy by two-step friction stir processing.* Scripta materialia, 2008. **59**(3): p. 356-359.

99. Galiyev, A., R. Kaibyshev, and T. Sakai, *Continuous dynamic recrystallization in magnesium alloy.* Magnesium Alloys 2003, Pts 1 and 2, 2003. **419-4**: p. 509-514.

100. Chen, M.-S., et al., *New insights on the relationship between flow stress softening and dynamic recrystallization behavior of magnesium alloy AZ31B.* Materials Characterization, 2019. **147**: p. 173-183.

101. Dudamell, N.V., et al., *Influence of texture on the recrystallization mechanisms in an AZ31 Mg sheet alloy at dynamic rates.* Materials Science and Engineering: A, 2012. **532**: p. 528-535.

102. Xin, Y., et al., *Tailoring the texture of magnesium alloy by twinning deformation to improve the rolling capability.* Scripta Materialia, 2011. **64**(10): p. 986-989.

103. Xu, S., et al., *Recrystallization mechanism of as-cast AZ91 magnesium alloy during hot compressive deformation.* Materials Science and Engineering: A, 2009. **527**(1-2): p. 52-60.

104. Jiang, M., H. Yan, and R. Chen, *Twinning, recrystallization and texture development during multi-directional impact forging in an AZ61 Mg alloy.* Journal of Alloys and Compounds, 2015. **650**: p. 399-409.

105. Srinivasarao, B., N. Dudamell, and M. Pérez-Prado, *Texture analysis of the effect of non-basal slip systems on the dynamic recrystallization of the Mg alloy AZ31.* Materials characterization, 2013. **75**: p. 101-107.

106. Li, H., C. Wu, and H. Yang, *Crystal plasticity modeling of the dynamic recrystallization of two-phase titanium alloys during isothermal processing.* International Journal of Plasticity, 2013(51): p. 271-291.

107. Li, H., X. Sun, and H. Yang, *A three-dimensional cellular automata-crystal plasticity finite element model for predicting the multiscale interaction among heterogeneous deformation, DRX microstructural evolution and mechanical responses in titanium alloys.* International Journal of Plasticity, 2016. **87**: p. 154-180.

108. Knezevic, M., et al., *A strain-rate and temperature dependent constitutive model for BCC metals incorporating non-Schmid effects: Application to tantalum–tungsten alloys.* International Journal of Plasticity, 2014. **62**: p. 93-104.

109. Lebensohn, R.A. and C.N. Tome, *A Self-Consistent Anisotropic Approach for the Simulation of Plastic-Deformation and Texture Development of Polycrystals - Application to Zirconium Alloys.* Acta Metallurgica Et Materialia, 1993. **41**(9): p. 2611-2624.

110. Wenk, H.R., et al., *A deformation-based model for recrystallization of anisotropic materials.* Acta Materialia, 1997. **45**(8): p. 3283-3296.

111. Solas, D.E., et al., *Deformation and recrystallization of hexagonal metals: Modeling and experimental results for zinc.* Acta Materialia, 2001. **49**(18): p. 3791-3801.

112. Walde, T. and H. Riedel, *Modeling texture evolution during hot rolling of magnesium alloy AZ31.* Materials Science and Engineering: A, 2007. **443**(1): p. 277-284.

113. Zecevic, M., et al., *Modeling of the thermo-mechanical response and texture evolution of WE43 Mg alloy in the dynamic recrystallization regime using a viscoplastic self-consistent formulation.* International Journal of Plasticity, 2020. **130**: p. 102705.

114. Chadwick, P., *Continuum Mechanics: Concise Theory and Problems*. 2012: Dover Publications.

115. Tomé, C. and R. Lebensohn, *Visco-plastic self-consistent (vpsc).* Los Alamos National Laboratory (USA) and Universidad Nacional de Rosario (Argentina), 2007. **6**.

116. Mecking, H. and U.F. Kocks, *Kinetics of Flow and Strain-Hardening.* Acta Metallurgica, 1981. **29**(11): p. 1865-1875.

117. Lavrentev, F.F., *The Type of Dislocation Interaction as the Factor Determining Work-Hardening.* Materials Science and Engineering, 1980. **46**(2): p. 191-208.

118. Capolungo, L., *Dislocation junction formation and strength in magnesium.* Acta Materialia, 2011. **59**(8): p. 2909-2917.

119. Khadyko, M., S. Dumoulin, and O. Hopperstad, *Slip System Interaction Matrix and its Influence on the Macroscopic Response of Al Alloys.* Materials Science Forum, 2014. **794-796**: p. 566-571.

120. Zecevic, M., et al., *Texture formation in orthorhombic alpha-uranium under simple compression and rolling to high strains.* Journal of Nuclear Materials, 2016. **473**: p. 143-156.

121. Jain, A. and S.R. Agnew, *Modeling the temperature dependent effect of twinning on the behavior of magnesium alloy AZ31B sheet.* Materials Science and Engineering a-Structural Materials Properties Microstructure and Processing, 2007. **462**(1-2): p. 29-36.

122. Chaboche, J.L., *1 - Unified Cyclic Viscoplastic Constitutive Equations: Development, Capabilities, and Thermodynamic Framework*, in *Unified Constitutive Laws of Plastic Deformation*, A.S. Krausz and K. Krausz, Editors. 1996, Academic Press: San Diego. p. 1-68.

123. Sehitoglu, H., et al., *Stress-strain response of a cast 319-T6 aluminum under thermomechanical loading.* Metallurgical and Materials Transactions a-Physical Metallurgy and Materials Science, 2000. **31**(1): p. 139-151.

124. Chaboche, J.-L., *A review of some plasticity and viscoplasticity constitutive theories.* International journal of plasticity, 2008. **24**(10): p. 1642-1693.

125. Krempl, E., *Models of Viscoplasticity Some Comments on Equilibrium (Back) Stress and Drag Stress.* Acta Mechanica, 1987. **69**(1-4): p. 25-42.

126. Voyiadjis, G.Z. and S.M. Sivakumar. *A finite strain and rate-dependent cyclic plasticity model for metals*. in *Proceedings of the International Seminar MECAMAT*. 1992.

127. Husser, E., E. Lilleodden, and S. Bargmann, *Computational modeling of intrinsically induced strain gradients during compression of c-axis-oriented magnesium single crystal.* Acta Materialia, 2014. **71**: p. 206-219.

128. Renganathan, P., J.M. Winey, and Y.M. Gupta, *Shock compression and release of a-axis magnesium single crystals: Anisotropy and time dependent inelastic response.* Journal of Applied Physics, 2017. **121**(3): p. 035901.

129. Renganathan, P. and Y.M. Gupta, *Shock compression/release of magnesium single crystals along a low-symmetry orientation: Role of basal slip.* Journal of Applied Physics, 2019. **126**(11): p. 115902.

130. Feather, W.G., et al., *Mechanical response, twinning, and texture evolution of WE43 magnesium-rare earth alloy as a function of strain rate: Experiments and multi-level crystal plasticity modeling.* International Journal of Plasticity, 2019. **120**: p. 180-204.

131. Chapuis, A., P. Liu, and Q. Liu, *An experimental and numerical study of texture change and twinning-induced hardening during tensile deformation of an AZ31 magnesium alloy rolled plate.* Materials Science and Engineering: A, 2013. **561**: p. 167-173.

132. Nugmanov, D., et al., *Origin of plastic anisotropy in (ultra)-fine-grained Mg–Zn–Zr alloy processed by isothermal multi-step forging and rolling: Experiments and modeling.* Materials Science and Engineering: A, 2018. **713**: p. 81-93.

133. Knezevic, M., et al., *Deformation behavior of the cobalt-based superalloy Haynes 25: experimental characterization and crystal plasticity modeling.* Acta Materialia, 2014. **63**: p. 162-168.

134. Zecevic, M., et al., *Modeling of intragranular misorientation and grain fragmentation in polycrystalline materials using the viscoplastic self-consistent formulation.* International Journal of Plasticity, 2018. **109**: p. 193-211.

135. Cáceres, C. and P. Lukáč, *Strain hardening behaviour and the Taylor factor of pure magnesium.* Philosophical magazine, 2008. **88**(7): p. 977-989.

136. Steglich, D. and Y. Jeong, *Texture-based forming limit prediction for Mg sheet alloys ZE10 and AZ31.* International Journal of Mechanical Sciences, 2016. **117**: p. 102-114.

137. Styczynski, A., et al., *Cold rolling textures in AZ31 wrought magnesium alloy.* Scripta Materialia, 2004. **50**(7): p. 943-947.

138. Jia, W.P., et al., *Texture evolution of AZ31 magnesium alloy sheets during warm rolling.* Journal of Alloys and Compounds, 2015. **645**: p. 70-77.

139. Guo, X., et al., *Experimental and numerical investigation of anisotropic and twinning behavior in Mg alloy under uniaxial tension.* Materials & Design, 2016. **98**: p. 333-343.

140. Prasad, N.S., et al., *Fracture behavior of magnesium alloys – Role of tensile twinning.* Acta Materialia, 2015. **94**: p. 281-293.

141. Jordon, J.B., et al., *Effect of twinning, slip, and inclusions on the fatigue anisotropy of extrusion-textured AZ61 magnesium alloy.* Materials Science and Engineering: A, 2011. **528**(22): p. 6860-6871.

142. Kim, S.-I. and Y.-C. Yoo, *Dynamic recrystallization behavior of AISI 304 stainless steel.* Materials Science and Engineering: A, 2001. **311**(1): p. 108-113.

143. Zhao, P., Y. Wang, and S.R. Niezgoda, *Microstructural and micromechanical evolution during dynamic recrystallization.* International Journal of Plasticity, 2018. **100**: p. 52-68.

144. Graetz, K., C. Miessen, and G. Gottstein, *Analysis of steady-state dynamic recrystallization.* Acta Materialia, 2014. **67**: p. 58-66.

145. Zhang, H., et al., *The dynamic recrystallization evolution and kinetics of Ni–18.3Cr–6.4Co–5.9W–4Mo–2.19Al–1.16Ti superalloy during hot deformation.* Journal of Materials Research, 2015. **30**(7): p. 1029-1041.

146. Quan, G.-Z., et al., *Constitutive modeling for the dynamic recrystallization evolution of AZ80 magnesium alloy based on stress–strain data.* Materials Science and Engineering: A, 2011. **528**(28): p. 8051-8059.

147. Gottstein, G., et al., *Prediction of the critical conditions for dynamic recrystallization in the austenitic steel 800H.* Materials Science and Engineering: A, 2004. **387-389**: p. 604-608.

148. Poliak, E.I. and J.J. Jonas, *A one-parameter approach to determining the critical conditions for the initiation of dynamic recrystallization.* Acta Materialia, 1996. **44**(1): p. 127-136.

149. Poliak, E.I. and J.J. Jonas, *Initiation of Dynamic Recrystallization in Constant Strain Rate Hot Deformation.* ISIJ International, 2003. **43**(5): p. 684-691.

150. Sommitsch, C. and W. Mitter, *On modelling of dynamic recrystallisation of fcc materials with low stacking fault energy.* Acta Materialia, 2006. **54**(2): p. 357-375.

151. Najafizadeh, A. and J.J. Jonas, *Predicting the Critical Stress for Initiation of Dynamic Recrystallization.* ISIJ International, 2006. **46**(11): p. 1679-1684.

152. Ning, Y., et al., *The same strain-rate sensitivity coefficient of 1/6 demonstrated from DRX critical and steady state during hot deformation for metallic materials.* Materials Letters, 2017. **196**: p. 83-86.

153. Roberts, W. and B. Ahlblom, *A nucleation criterion for dynamic recrystallization during hot working.* Acta Metallurgica, 1978. **26**(5): p. 801-813.

154. Shao, Y.-c., et al., *Polycrystal modeling of hot extrusion texture of AZ80 magnesium alloy.* Transactions of Nonferrous Metals Society of China, 2016. **26**(4): p. 1063-1072.

155. Wu, C., H. Yang, and H. Li, *Simulated and experimental investigation on discontinuous dynamic recrystallization of a near-α TA15 titanium alloy during isothermal hot compression in β single-phase field.* Trans. Nonferrous Met. Soc. China, 2014. **24**(6): p. 1819-1829.

156. Takaki, T., et al., *Multi-phase-field model to simulate microstructure evolutions during dynamic recrystallization.* Materials transactions, 2008. **49**(11): p. 2559-2565.

157. Cram, D.G., et al., *Modelling discontinuous dynamic recrystallization using a physically based model for nucleation.* Acta Materialia, 2009. **57**(17): p. 5218-5228.

158. Li, N., et al., *Deformation mechanisms and dynamic recrystallization of AZ31 Mg alloy with different initial textures during hot tension.* Materials & Design, 2013. **50**: p. 382-391.

159. Bernard, P., et al., *A two-site mean field model of discontinuous dynamic recrystallization.* Materials Science and Engineering: A, 2011. **528**(24): p. 7357-7367.

160. Ostapovets, A., P. Molnár, and P. Lejček, *Boundary plane distribution for Σ13 grain boundaries in magnesium.* Materials Letters, 2014. **137**: p. 102-105.

161. Prasad, Y. and K. Rao, *Processing maps for hot deformation of rolled AZ31 magnesium alloy plate: Anisotropy of hot workability.* Materials Science and Engineering: A, 2008. **487**(1-2): p. 316-327.

162. Shewmon, P. and F. Rhines, *Rate of self-diffusion in polycrystalline magnesium.* JOM, 1954. **6**(9): p. 1021-1025.

163. Balogh, L., et al., *The contributions of grain size, dislocation density and twinning to the strength of a magnesium alloy processed by ECAP.* Materials Science and Engineering: A, 2010. **528**(1): p. 533-538.

164. May, J., et al., *Mechanical properties, dislocation density and grain structure of ultrafine-grained aluminum and aluminum-magnesium alloys.* Metallurgical and Materials Transactions A, 2007. **38**(9): p. 1941-1945.

165. Wang, C., et al., *Severe plastic deformation techniques for bulk ultrafine-grained materials.* Rare Metal Materials and Engineering, 2012. **41**(6): p. 941-946.

166. Valiev, R.Z., et al., *Producing bulk ultrafine-grained materials by severe plastic deformation.* Jom, 2006. **58**(4): p. 33-39.

167. Frydrych, K. and K. Kowalczyk-Gajewska, *A three-scale crystal plasticity model accounting for grain refinement in fcc metals subjected to severe plastic deformations.* Materials Science and Engineering: A, 2016. **658**: p. 490-502.